Friedrich-Alexander-Universität
Naturwissenschaftliche Fakultät

Master's Thesis
in Physics

Analysis of two extended γ-ray structures around pulsars

Darius Grüber

Supervisor: Dr. Alison Mitchell

Erlangen Centre for Astroparticle Physics

Submission date: 24.02.2025

Contents

Abstract

Studying astrophysical sources has shown to reveal fascinating processes that lead to the emission of γ-rays stemming from cosmic-ray interactions. While many sources show an evenly and spatially confined emission of γ-rays around their source of origin, some tend to be of extended and diffuse nature. Analysing these sources requires a non standard approach to be applied upon the data since no spatially confined structures can be obtained from such regions. Two such structures of extended emission that are hereby discussed in this work are the regions around the pulsars B1046-58 and B0656+14. The former of them is located within the vicinities of Eta Carinae and Westerlund 2, whereas the latter is associated to the Monogem TeV halo. Thereby, this work deals with the analysis of TeV emission that is present around these sources using data from the H.E.S.S. telescope array. The data analysis of the observations included "traditional" background estimations as well as the newly derived method of ON-OFF matching by Wach et al. (2024). Using the data gained from these methods as well as additional observations across the radio to sub-TeV energy band, it is estimated that the emission surrounding the pulsar B1046-58 is most probably due to a pulsar wind nebula (PWN). However, due to lack of data across the TeV domain, a final categorisation could not be made so far. The analysis of B0656+14 on the other hand has shown the advantages that the ON-OFF matching can provide for very extended γ-ray sources. Yet, the application of own produced data for B0656+14 has then shown a systematic bias, which unfortunately made it impossible to carry out further analysis steps.

1 Introduction

Since the advent of particle physics in the late 19$^{\text{th}}$ century ever more progress has been made regarding the most elementary parts of our universe. Kickstarted by the discovery of X-rays by Röntgen (1898), further experiments were carried out to examine the nature of radiative sources. Geitel (1900) & Elster (1901) as well as Wilson (1900) independently observed ionizing effects from experiments with electrical charged bodies that are exposed to air. Since no mechanism causing this ionisation was known yet, a couple of suggestions were made, alongside which a possible solution to the origin of the free ions involved cosmic sources (Cirkel-Bartelt, 2008).
However, initial suggestions by Victor Hess involved that possible effects of rays penetrating the atmosphere would be diminished by some kind of ground based radiation. Although initially wanting to prove that the ionisation effect decreases in higher altitudes, he found the opposite to happen above a certain distance from ground. This then led to the conclusion that there are some kind of rays that interact with the atmosphere, causing then the outcomes of his experiment (Hess, 1912).
Yet, due to the unfortunate event of World War I, it took until the 1920's until an adequate explanation of these "cosmic rays" was found by Milikan (1926), marking the beginning of modern astroparticle physics. Compton (1933) then came to the conclusion that cosmic rays are mainly consisting of protons, electrons, and helium nuclei.
According to these findings, this chapter deals with the current knowledge of how the spectrum of cosmic rays that is measured on Earth arises as well as its core features. Furthermore an overview of the production of γ-rays from cosmic ray interactions is given. Then the formation and properties of one such γ-ray source - the pulsar - are discussed and its first $\sim$ 100 kyr of existence is presented. At last the interactions of cosmic particles within our atmosphere are described and a method to measure them is presented.

1.1 Cosmic ray spectrum

The composition of cosmic rays has been the subject of numerous experiments over the years, and no final answer explaining the entire spectrum has been found yet. Current estimates of the cosmic ray composition suggest that $\sim$90 % of the measured ones are protons, together with heavier nuclei as well as electrons (few per mill). Alongside these charged particles, photons and neutrinos are also part of the cosmic ray spectrum, albeit being sometimes treated separately from the charged domain (De Angelis et al., 2018).
Additionally antimatter makes up a tiny fraction of the total cosmic ray population, where mostly anti-protons and positrons have been measured so far. It is suggested that larger antimatter structures (e.g. $^3\bar{\text{He}}$) are present in the cosmic ray flux, which however are not confirmed until now (Blum et al., 2017).
In order to investigate the origins of the spectrum of cosmic rays observed on Earth, an overview of the spectrum is first presented, before going more into detail about the structure it shows. Using data from several decades of observations, the spectrum of cosmic rays present within the Earth's atmosphere can be seen in Fig. 1. The plot shows the intensity of measured cosmic rays (scaled by E^2) over energy. Thereby, the observed intensities of the different constituents to the cosmic ray composition can be seen together with a grey colour

scale, indicating the rate of their occurrence. In total, the showed spectra include those for protons, electrons, positrons, galactic γ-ray background, anti-protons, neutrinos, as well as the isotropic (extragalactic) γ-ray background (IGRB).

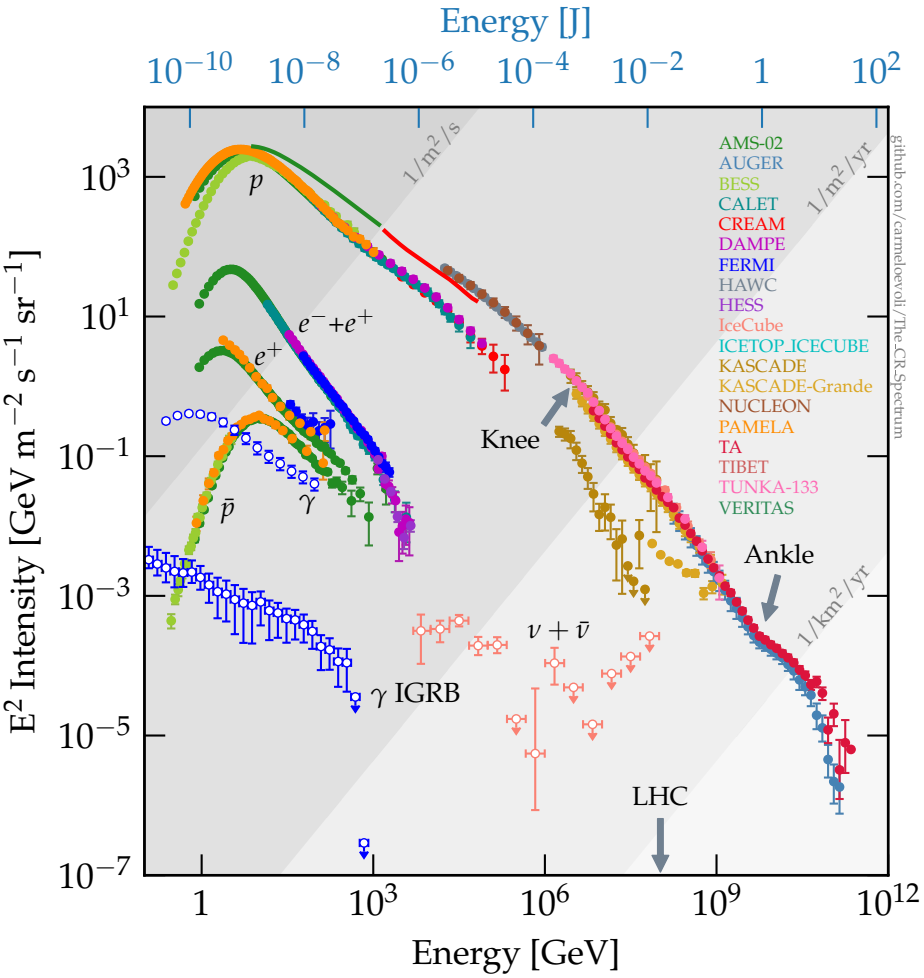

Figure 1: Cosmic ray spectrum using multi-wavelength data from various observation sites. Figure taken from (Evoli, 2020).

The spectrum follows a power law $E^{-\gamma}$ and has two visible quantities called the "knee" at $\sim 10^6$ GeV and "ankle" at $\sim 10^9$ GeV. Besides these two indicated quantities, two additional observable characteristics exist within the cosmic ray spectrum. Thereby, one identifies the bulk at $\sim 10^7$ GeV as the "second knee" of the spectrum. Furthermore, it can be seen that a cutoff occurs at $\sim 4 \cdot 10^{10}$ GeV, which is due to the Greisen-Zatsepin-Kuz'min (GZK) effect, which is explained further below (Navas et al., 2024; Watson, 2014).

1.1.1 Spectrum up to the "knee"

The spectrum in this range is dominated by energy losses as well as solar influences for energies below ~ 10 GeV. The solar influences change for increasing energies, leading to a

power law shape with index ∼2.7 and a shift of the origin to be of galactic nature. Thereby, the origins of cosmic rays within our galaxy are estimated to be mainly from supernova remnant (SNR) regions, composed typically of a centre star remnant (e.g. neutron star) and the blasting shock wave of the supernova explosion (Navas et al., 2024; Slane, 2017).
The mechanisms causing SNRs and cosmic rays and furthermore the γ-rays from these remnants are discussed later in sections 1.3 & 1.4. Additionally, massive stars ($> 20 M_{\odot}$) are assumed to contribute to the spectrum by interactions of their stellar wind with surrounding molecular clouds (Cesarsky et al., 1983). Additionally, microquasars, which are binary systems of a star remnant (black hole or neutron star) and a regular star, are assumed to be a source of cosmic rays. Thereby, they accelerate protons through their termination jets, causing also potential γ-radiation when the cosmic rays interact with the interstellar medium (ISM) (Mirabel, 2007; Bosch-Ramon et al., 2005). At last, the galactic centre could also be an accountable source for cosmic radiation, as it is estimated to accelerate particles during periods of activity ($\sim 10^7 - 10^8$ yr) (Ptuskin et al., 1981).
Around the "knee", the spectrum has a changed slope, i.e., the spectral index changes from ∼2.7 to ∼3, which is estimated to be due to several reasons. Thereby, the change of the spectrum with increasing energy could be due to a change in particle acceleration efficiency, but also due to possible photodisintegration around the sources. Furthermore, other estimates include a change in confinement by magnetic fields and also possible influences of single source explosions. However, there is up until now not a final explanation of the "knee", thus requiring further studies of the spectrum (Candia et al., 2003).

1.1.2 From "knee" to "ankle"

A second change in the spectrum can be observed after the initial "knee", leading to a further increase of the spectral index from ∼3 to ∼3.3. This shift is estimated to be due to a change from galactic to extragalactic sources, thus leading to a subsequent cutoff of galactic cosmic rays. Thereby, the "second knee" can be seen as the point at which galactic cosmic rays have reached their maximum acceleration limit. At this point then, the influence of extragalactic sources starts to become more important, and its influence starts to shift the spectrum's slope (Navas et al., 2024).
There are various extragalactic sources that could be shaping the spectrum of ultra-high energy cosmic rays (UHECRs). Thereby, among the most probable sources for cosmic rays are active galactic nuclei (AGN), which can accelerate particles by its jet and strong magnetosphere (Rieger, 2022).
Furthermore, γ-ray bursts (GRBs) are also accounted to be a source for the observed cosmic ray spectrum, although their origin is still an open debate. Thereby, one divides between short- (SGRBs) and long-lived (LGRBs) ones, calling the former as such if it exhibits a duration of ∼2 s. The current knowledge regarding these objects is that SGRBs are formed by the merging of two stellar remnants (two neutron stars, or perhaps a neutron star and black hole), causing the neutron star to be torn apart. The LGRBs are thought to be occurring in case a black hole is formed, leading to a massive release of energy due to the massive gravitational potential. However, up to now only the theory describing LGRBs is commonly accepted, while the SGRB merger theory remains uncertain, thus requiring further experiments to prove it (Gehrels et al., 2012).
Besides that, so-called starburst galaxies, which are galaxies undergoing long period star

formation processes, can emit cosmic rays by an interplay of stellar winds and supernova explosions. Thereby, it possible that particles are accelerated by the winds of these starbursts, allowing them to escape the region before photodisintegration plays a role (Anchordoqui et al., 1999; Romero et al., 2018).
At last, besides galactic pulsars and magnetars, also extragalactic ones play a major role in accelerating cosmic rays within their vicinity, which, as previously mentioned, will be explained in sections 1.3 & 1.4 more thoroughly. Yet, it is important to mention that the "second knee" does not represent an abrupt end of galactic sources. It can rather be seen as the point at which the contribution of these sources starts to decrease while simultaneously having extragalactic contributions starting to occur (Navas et al., 2024).
This shift is supported by the fact that cosmic rays at these energies can have gyroradii the size of the Milky Way's thickness, thus allowing them to exit it. The point at which it is assumed that the cosmic rays are entirely from extragalactic origin is referred to as "ankle", also accompanied by a spectral index shift from $\sim$3.3 to $\sim$2.5. However, these estimated contributions from non-galactic sources are still up to debate, since some models assume that galactic γ-ray bursts or magnetars could also be accountable for the observed spectrum around the ankle (Drury, 2012, Navas et al., 2024; Watson, 2014).

1.1.3 GZK-cutoff

The GZK-cutoff is a theoretically derived effect suggesting that the flux of cosmic rays observable on Earth is experiencing a suppression around $\sim 4 \cdot 10^{10}$ GeV. Thereby, the main constituent of high energy cosmic rays - the protons - can interact with photons of the cosmic microwave background (CMB) leading to the Δ^+ resonance

$$p + \gamma_{\text{CMB}} \longrightarrow \Delta^+ \longrightarrow \begin{cases} p + \pi^0 \\ n + \pi^- \end{cases} .$$

This process has a mean free path[1] of $\sim$4 Mpc, leading to a subsequent reduction of its energy by a factor of $\sim$0.2. Thereby, the effective distance in which Δ^+ resonance can occur is in the order $\sim$20 Mpc, which also makes it the most dominant energy-loss mechanism for cosmic rays. However, it is still up to debate whether or not the cutoff as shown in Fig. 1 is the GZK-cutoff or just the limit to which cosmic rays can be accelerated in general (Watson, 2014).

1.2 γ-ray production from cosmic-rays

Since cosmic rays are essentially charged, relativistic particles, they can be deflected by magnetic fields, thus making it hard to reconstruct their source of origin. Therefore, studying the neutral product of cosmic ray interactions, i.e., γ-rays, can give vital information about cosmic ray acceleration mechanisms. Therefore, it is first discussed how the particle interactions of cosmic rays can lead to various forms of γ-radiation. Conclusions made from these particle interaction considerations allow then to make further suggestions about the

[1]Measure to describe the mean length a cosmic ray can travel before interacting with a CMB photon.

astrophysical sources and therefore can give valuable insights about their originating region. Therefore, this section discusses the most important processes that lead to the emission of γ-rays.

1.2.1 Bremsstrahlung

Bremsstrahlung describes the decelerating effect of a magnetic field (e.g. of an ion or nucleus) upon a charged particle (see Fig. 2). The thereby produced photon has then an energy which is equal to the kinetic energy loss of the charged particle (Jardin-Blicq, 2019).

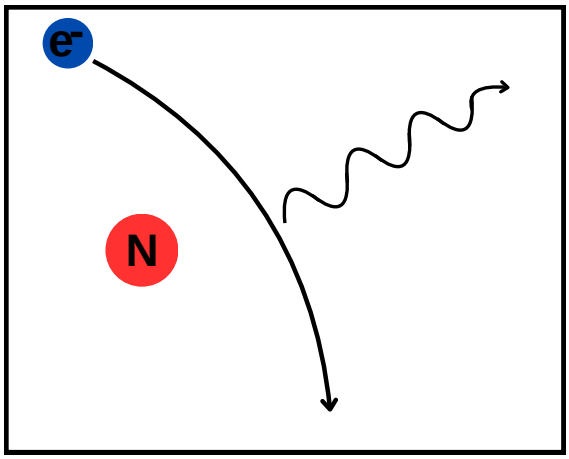

Figure 2: Emission of Bremsstrahlung on the example of an electron (e^-) interacting with a nucleus (N).

1.2.2 Synchrotron radiation

Synchrotron radiation can be seen as a special case of Bremsstrahlung, as it involves also the interaction of a magnetic field upon a charged particle. However, in this case the magnetic field of a given source object is acting as an accelerating instance, since it induces a Lorentz force perpendicular to the field lines. This then provokes a circular motion of the charged particles, leading to a further acceleration that then leads to photon emission in perpendicular direction to the path the charged particles travel along (see Fig. 3). This radiation can be seen between the radio and lower γ-ray bands ($\sim 10^{-15} - 10^{6}$ eV) (Jardin-Blicq, 2019).

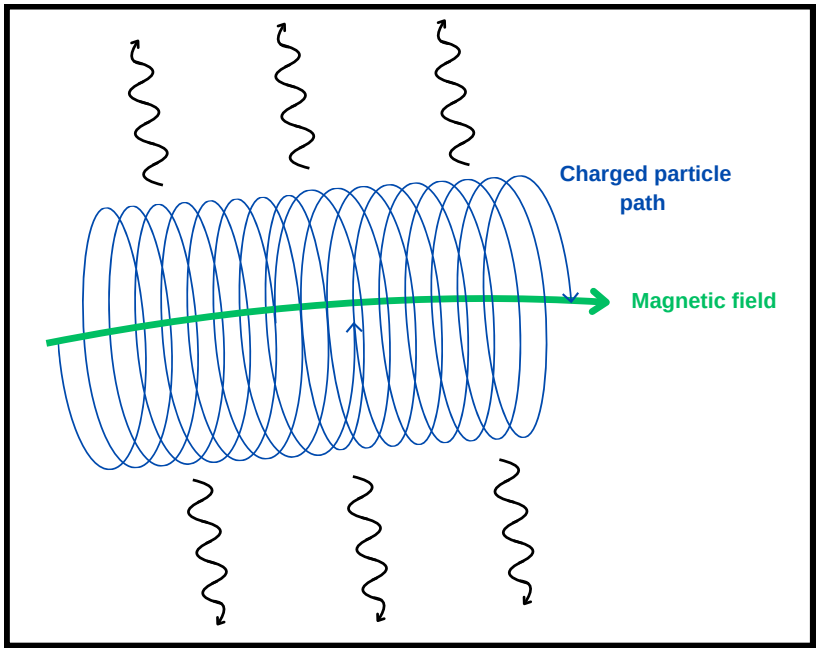

Figure 3: Schematic overview of synchrotron emission arising when a charged particle travels alongside a magnetic field.

1.2.3 Inverse Compton (IC) scattering

As depicted in Fig. 4, photons can gain energy through scattering with relativistic electrons, which is then referred to as inverse Compton scattering. This effect is typically important between X-ray and γ-ray band ($\sim 10^3 - 10^{15}$ eV) and takes place between boosted electrons and photons of lesser energy, typically originating from the CMB, stellar radiation fields, and dust (Jardin-Blicq, 2019).

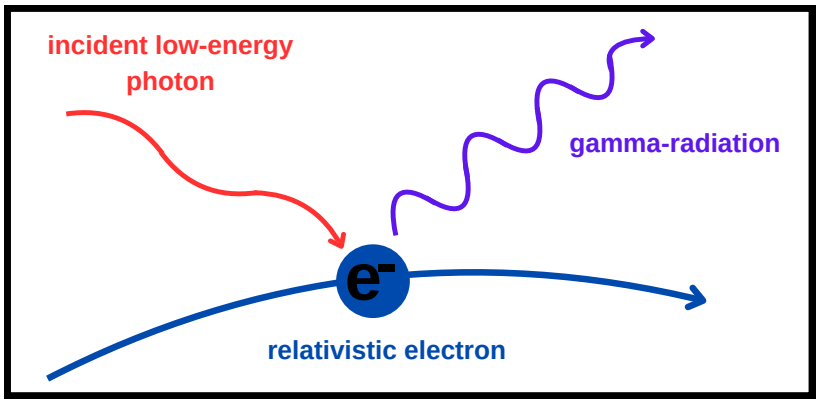

Figure 4: A lower energy photon gains energy through a scattering process with a relativistic electron, also known as inverse Compton scattering.

1.2.4 Proton-Proton (PP) interactions

Photons due to hadronic interactions are also a possible resource for observed γ-radiation with the most frequently occurring process being proton-proton collisions in that case. Colliding protons can cause γ-radiation not directly, but rather through the subsequent decay of the neutral pion (π^0) they have produced (see Fig. 5). This adds a hadronic origin to the observed γ-rays, thus adding the possibility that not only leptonic interactions cause it (Jardin-Blicq, 2019).

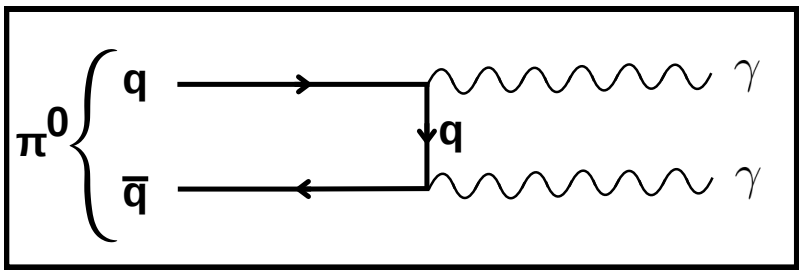

Figure 5: Feynman diagram of the neutral pion decay into two photons.

Furthermore the collision of protons can cause charged pions ($\pi^{\pm}$) to appear, which decay via a weak decay into $\mu^{\pm}$ and ν_{μ}. Therefore, the hadronic branch of cosmic ray interactions is not only responsible for the observable γ-radiation, but also for the neutrino production. Furthermore, as the muon decays into $e^{\pm}\nu_e\nu_{\mu}$, even larger populations of neutrinos are estimated to be originating from cosmic-ray interactions. Thereby, analysing them could add vital information to the cosmic-ray puzzle in the future (De Angelis et al., 2018).

1.3 Supernovae & pulsar formation

Having now discussed how cosmic ray interactions can cause γ-ray production, a further look on one such source - the pulsar - is taken. For this purpose, the mechanisms of core collapse supernovae and supernova with accreted material are first discussed, with the former being of particular importance since it includes the possibility of the formation of neutron stars. Following these introductions, the main properties of the pulsar, a special type of neutron star, and its effects on the immediate environment are discussed.

1.3.1 Type Ia supernovae

The name convention of supernovae is of historical nature, since they were first categorised based on their absence (type I) and presence (type II) of hydrogen spectral lines. Later it was found that there are several different sub-classes within the types based on the presence (Ia) and absence of silicon lines (Ib and Ic). Thereby, supernovae that have no silicon lines can be further divided based on the occurrence of helium in their spectra, which is only the case for type Ib supernovae (Cerda-Duran et al., 2018).
However, the supernova kinds differ not only based on their observed absorption lines, but

also on their formation process. Contrary to the core collapse mechanism, type Ia supernovae typically occur in a binary system consisting of a white dwarf and a main sequence star. Thereby, the white dwarf accretes material from its neighbouring star, leading to increased temperature and pressure, thus making carbon fusion through 3α processes possible. If the Chandrasekhar limit ($M>1.4\ M_\odot$) is reached, a thermonuclear runaway process leads to critical instabilities of the system. This causes the energy density to rise, thus provoking massive expansive forces to act on the white dwarf, which finally lead to its disruption in an enormous explosion (Demtröder, 2017).

1.3.2 Type II, Ib & Ic supernovae

In contrast to the binary system supernova of type Ia, the supernovae of types II, Ib, and Ic form once a regular massive ($M \geq 8M_\odot$) main sequence star approaches the end of its lifetime. Thereby, the stellar evolution is determined by its inner balance between the gravitational forces and the hydrostatic pressure. Typically, in stars like our sun, the main cause for the hydrostatic pressure to be present is the fusion process of hydrogen. For more massive stars, further fusion processes can occur (e.g., burning of ^{12}C, ^{16}O, ^{20}Ne, ^{28}Si) until ^{52}Fe is reached. However, for stars at the lower end of the $8M_\odot$ border, only burning of ^{12}C is reached, as the fusion of more massive elements would require a higher temperature to occur. In case the burning cycles continue to ^{52}Fe, no further fusion processes can occur, as it has the highest binding energy per nucleon. Thereby, an iron-nickel core is slowly formed, which is surrounded by lighter elements ("onion shell") with the outermost shell consisting of cooled hydrogen, unable to undergo any fusion processes (Demtröder, 2017; Cerda-Duran et al., 2018).
The star remains in this more or less stable state until the thermal pressure can not counter the gravity any more. Once this is the case, the star collapses under the gravitational pull from the centre. During this phase, free protons and electrons can interact with each other, such that inverse β-decay

$$e^- + p \longrightarrow n + \nu_e$$

occurs, which reduces the electron degeneracy pressure that counters gravitation up to that point. After the electrons are gone, nothing stops the gravitational collapse until the matter is dense enough that neutron degeneracy pressure sets in (Demtröder, 2017).
The further development of the system depends on the progenitor's mass. If the degeneracy pressure of the neutrons is not sufficient enough to counteract the gravitational pull, a black hole arises. However, if it is sufficient enough, then the gravitational collapse is stopped at a certain distance from the core (typically $r = \sim 10$ km), and a neutron star formation is possible. In this case, the material flow provokes an increasing density up until the matter is so compact that it has $\rho = 10^{16}$ kg m^{-3} (= atomic nucleus density). From this point onwards, no more matter can flow into the centre, creating a shock wave that spreads outwards with a speed of $\sim 5 \cdot 10^4$ km s^{-1}. The shock wave rips the surrounding layers of the star away resulting in an immense explosion ($E \approx 10^{44}$ J), referred to as core collapse supernova (Demtröder, 2017).

1.3.3 Pulsars

The remnant of a core collapse supernova that has not formed a black hole is called a neutron star and is mainly composed of degenerated neutron matter. It is categorised by two main features, a strong magnetic field strength ($\sim 10^{11} - 10^{13}$ G) and a short rotational period ($\sim 0.03 - 3$ s), both being due to angular momentum conservation from the predecessor star (Demtröder, 2017; Slane, 2017; De Angelis et al., 2018).
A special type of neutron stars are the so-called pulsars (short form of **Puls**ating st**ar**) which were first observed[2] by Hewish et al. (1979). Pulsars are characterised by having a magnetic axis that deviates from the axis of rotation (see Fig. 6), which causes them to emit radiation in a pulsed manner similar to a lighthouse (Demtröder, 2017; Slane, 2017; De Angelis et al., 2018).

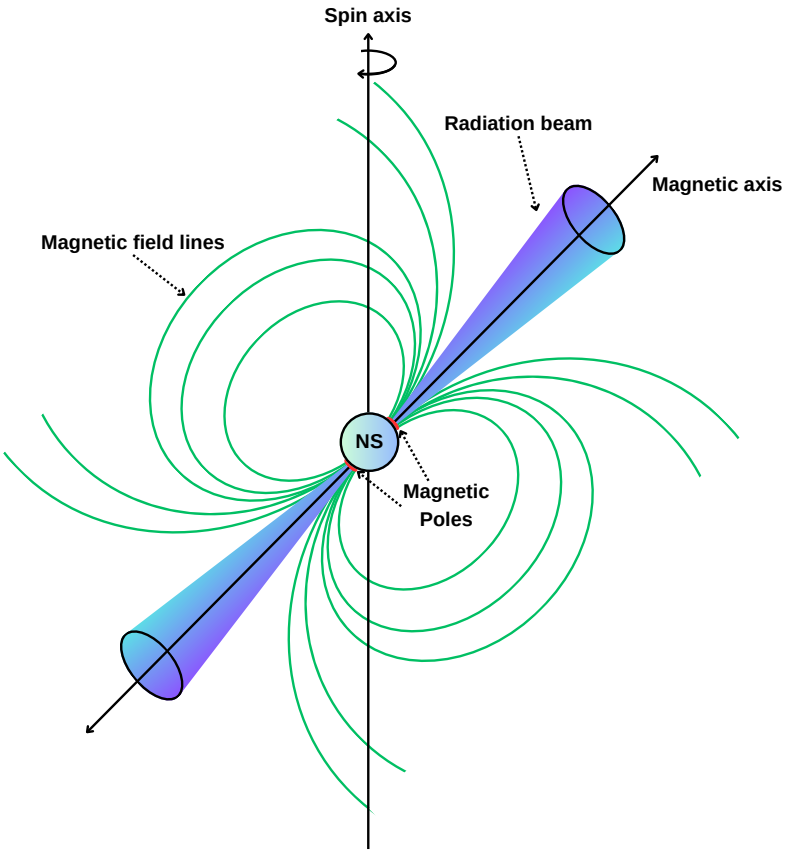

Figure 6: Schematic representation of the pulsar, which is a neutron star (NS) characterized by its magnetic field being misaligned to the axis of rotation.

[2]It was actually Jocelyn Bell Burnell who discovered the first Pulsars under her supervisor Anthony Hewish. However, it was only Hewish which later got a Nobel prize for the discovery together with Martin Ryle (Lee, 2013).

The pulsar itself emits electromagnetic radiation through its powerful magnetic fields, which lead to pair production processes, i.e., generation of electron-positron pairs. Additionally, particles can be ripped out of the pulsar's surface due to its strong magnetic fields, which then add to the particle population. Thereby, the electrons and positrons get accelerated towards relativistic velocities, causing them to emit synchrotron radiation (see section 1.2) within the radio to X-ray band. The jets containing this relativistic outflow cause a particle wind to form, which is then referred to as the pulsar wind. This particle wind travels through the supernova ejecta, which eventually leads to a deceleration process. The region in which this slowdown occurs is called the termination shock, where the outward moving wind is counterbalanced by the pressure of the media in which it expands. Beyond the termination shock, a region of shocked relativistic plasma is formed, which is called the pulsar wind nebula (PWN). Inside the PWN, γ-ray emission in the TeV domain occurs and is mainly due to IC scattering of the electrons and positrons with the CMB, but also due to Bremsstrahlung and pion decay (see section 1.2). Thereby, the pulsar powers the PWN and continuously loses energy primarily due to electromagnetic radiation and the particle wind that sustains the PWN (Wang, 2014; Kirk et al., 2009; Harding et al., 2006; Demtröder, 2017).
The injected energy is thereby directly dependent on the rotational energy E_{rot} of the pulsar. Thereby, an important quantity is the spin-down luminosity (Gaensler et al., 2006)

$$\dot{E} = -\frac{dE_{\text{rot}}}{dt} = 4\pi^2 I \frac{\dot{P}}{P^3}, \tag{1}$$

which describes the rate at which the pulsar's rotational energy is put into its PWN. Hereby, I denotes the pulsar's moment of inertia (typically $\sim 10^{45}$ g cm^{-2}), P is the rotational period, and $\dot{P}$ its first time derivative. The crab pulsar for example has been found to have $\dot{E} \approx 5 \cdot 10^{38}$ erg cm^{-2} s^{-1} (Gaensler et al., 2006).
The age a neutron star has can also be described by the rotational period (Gaensler et al., 2006)

$$\tau = \frac{P}{(n-1)\dot{P}} \left[1 - \left(\frac{P_0}{P} \right)^{n-1} \right], \tag{2}$$

where P_0 is the initial period, and n is the so-called braking index (typically $2 < \text{n} < 3$). However, most of the time, n=3 is assumed, as this represents the case of a magnetic dipole, i.e. $P_0 \ll P$, leading to the so-called pulsar's characteristic age (Gaensler et al., 2006)

$$\tau_c = \frac{P}{2\dot{P}}, \tag{3}$$

which is mostly stated as the age of the pulsar.
Additionally, the magnetic field strength is given as (Gaensler et al., 2006)

$$B = 3.2 \cdot 10^{19} \sqrt{P[\text{s}]\dot{P}}\ \text{G}, \tag{4}$$

and ranges between $10^8 - 10^{15}$G. In the latter case one calls such objects magnetars, whereas the former case categorises millisecond pulsars. Typically in order to have a PWN, a pulsar must have $B = 10^{12} - 5 \cdot 10^{13}$ G (Gaensler et al., 2006).

1.4 Post supernova evolution

Next, the evolution of the PWN system is discussed using the current state of knowledge on how the system behaves in its first ∼100 kyr. Thereby, three different time zones are of interest, the first being in $\lesssim$10 kyr, in which the PWN and SNR are existing in almost coincidental positions. This is followed by a subsequent escape of the PWN from the SNR system within ∼10-100 kyr until it is estimated to be fully outside its hosting SNR. After the PWN has escaped its hosting SNR at $\gtrsim$100 kyr, it is estimated to form a TeV pulsar halo, a sphere characterised by diffuse γ-ray emission. However, it is important to mention that not all post supernova system end up showing a TeV halo in general, therefore existing further in a phase where γ-ray emission is due to the PWN (Giacinti et al., 2020).

1.4.1 Formation of PWN+SNR system ($\lesssim$10 kyr)

After the occurrence of a supernova, the pulsar has a direct zone of influence, in which it provokes particle interactions through energy injection according to Eqn. (1). The region, as it can be seen in Fig. 7, is best characterisable by dividing it into two different zones of interest, these being the direct influence zone of the pulsar (i.e. the PWN), and the surrounding supernova remnant (SNR). During the earlier phase of the system ($t \lesssim 10$ kyr), the PWN together with its hosting pulsar shares roughly the same centre position as the SNR (Giacinti et al., 2020).
The SNR itself expands with up to 10^4 km s^{-1}, thereby having a forward shock (FS) that expands further into the surrounding ISM/circumstellar medium. This expansion is accompanied by a subsequent increase of pressure and temperature for the media affected by the shock front. Besides the expansion of the SNR, it can be observed that the pulsar itself moves with a velocity of > 400 km s^{-1} due to the inhomogeneous explosion. Thereby, the PWN remains inside a region that is characterised by a relatively low pressure compared to its own, therefore allowing a vast expansion within the SNR. One usually refers to systems in which the PWN is located within the SNR as being composite systems (Gaensler et al., 2006).
As previously discussed, relativistic particles in form of the pulsar wind stream outwards leading to interactions with its surrounding media, thus causing the formation of the termination shock front. Furthermore, a PWN arises outside the termination shock, which is sustained by the pulsar wind composed of relativistic electrons and positrons, accelerated by the magnetic fields of the pulsar. Overall, it can be observed that the γ-radiation is confined within the PWN, whose size increases due to the constant energy input of the pulsar. This inflation benefits from the previously mentioned pressure gradient in the SNR, thus causing the PWN to inflate at supersonic speeds (Giacinti et al., 2020).

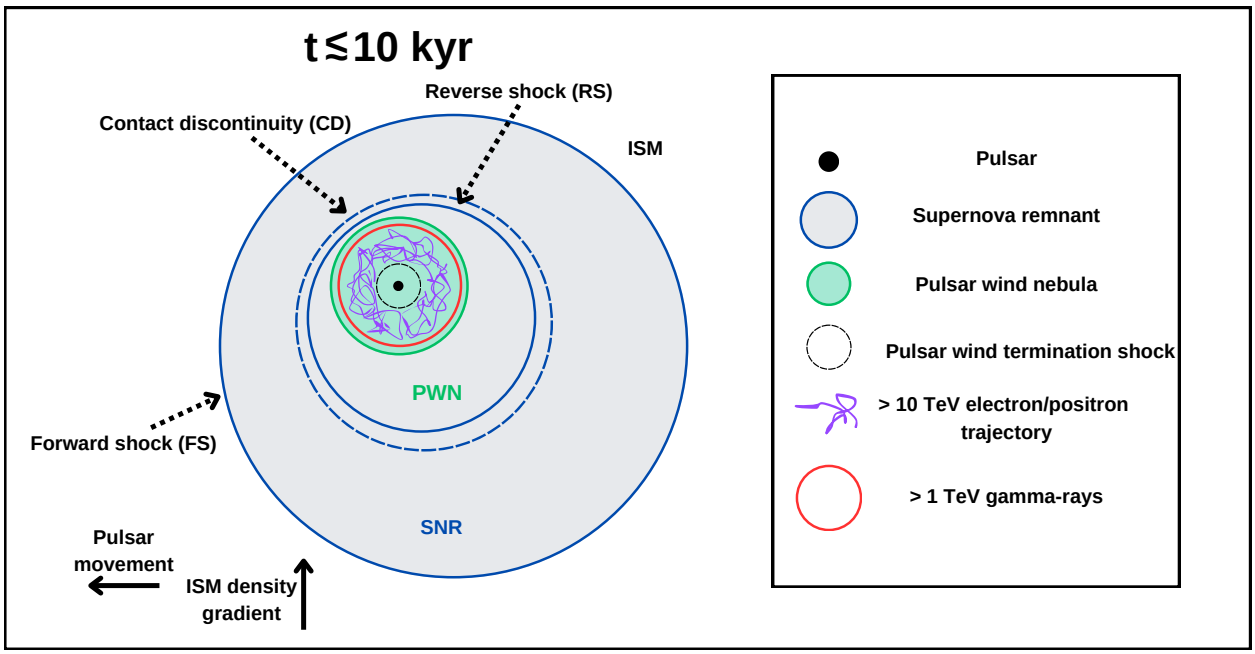

Figure 7: Initial PWN+SNR formation right after the supernova has occurred together with the direction of the pulsar and the ISM density gradient. Note that the direction of motion of the pulsar, as well as the ISM gradient is arbitrary and does not always have to be this way. Although this schematic overview is made by own means, it is important to notice that it is majorly based on Fig. 1 in (Giacinti et al., 2020).

With the growing size of the SNR, a decelerating effect starts to arise as ever more material from the surrounding media is swept up by the FS. This causes a pressure to build-up in the shocked region, eventually leading to the formation of the reverse shock (RS), which propagates inward. As the RS traverses the colder metal enriched gas, X-ray emission can be observed as the RS heats the ejecta up. Thereby, one refers to the region between RS and FS as the contact discontinuity (CD), which separates the zones of shocked ejecta by the RS from the shocked ambient medium by the FS (Slane, 2017; Gaensler et al., 2006).
At $\sim 10^3$ kyr, the SNR enters its so-called "Sedov-Taylor" phase, characterised by an adiabatic expansion into the ISM/circumstellar medium, where the FS shell's radius is given as $R \propto t^{2/5}$. During this evolution phase of the remainder system, radio, X-ray and γ-ray emission occur within coincident regions. Thereby, the radio to X-ray emission can be traced down to observable synchrotron emission due to particle accelerations around the pulsar as well as heat induced emission from the RS. TeV emission is present within the PWN and is mainly due to IC scattering, but also in parts due to Bremsstrahlung or pion production. However, at $\sim 10^4$ kyr the RS is estimated to collide with the PWN, thus marking the beginning of the second evolutionary phase of the PWN (Giacinti et al., 2020; Slane, 2017; Gaensler et al., 2006; Truelove et al., 1999).
Before moving forward to the next phase, it is worth mentioning that the direction in which the SNR expands is in general dependent on where the ISM density gradient points. In Fig. 7, the gradient points upwards, thereby causing the expansion of the SNR (and thereby of everything it contains) to be slowed down in that direction. In addition to that, a spherical

shape of the structure is generally a simplification and does not necessarily reflect real systems, as the most famous Crab Nebula does show a more complex reality (Giacinti et al., 2020).

1.4.2 Intermediate system (∼10-100 kyr)

After a couple of thousand years, the PWN and RS collide with each other, causing the forward moving PWN expansion to be repressed, thus leading to an increased pressure and a subsequent expansion. This reverberative process leads to oscillations (typically lasting a few thousand years), causing TeV γ-ray emission regions to stream outside of the SNR, while some parts of this emission are still within the SNR itself (Gaensler et al., 2006).
Thereby, this process is accompanied by a shift in the observable emission between the low-energy ranged (radio & X-rays) and γ-radiation, leading to spatially non-coincident regions of particle acceleration. Electrons that are accelerated to high energies by the magnetic source fields thereby emit synchrotron radiation and then cool rapidly at short distances. Contrary to that, γ-rays are emitted at larger distances from the pulsar and are dominantly produced via IC scattering of older (less energetic) electrons with the CMB. Furthermore, due to this mechanism and the motion of the pulsar, the location of the γ-ray and the radio to X-ray emission may not coincide with each other (Giacinti et al., 2020).

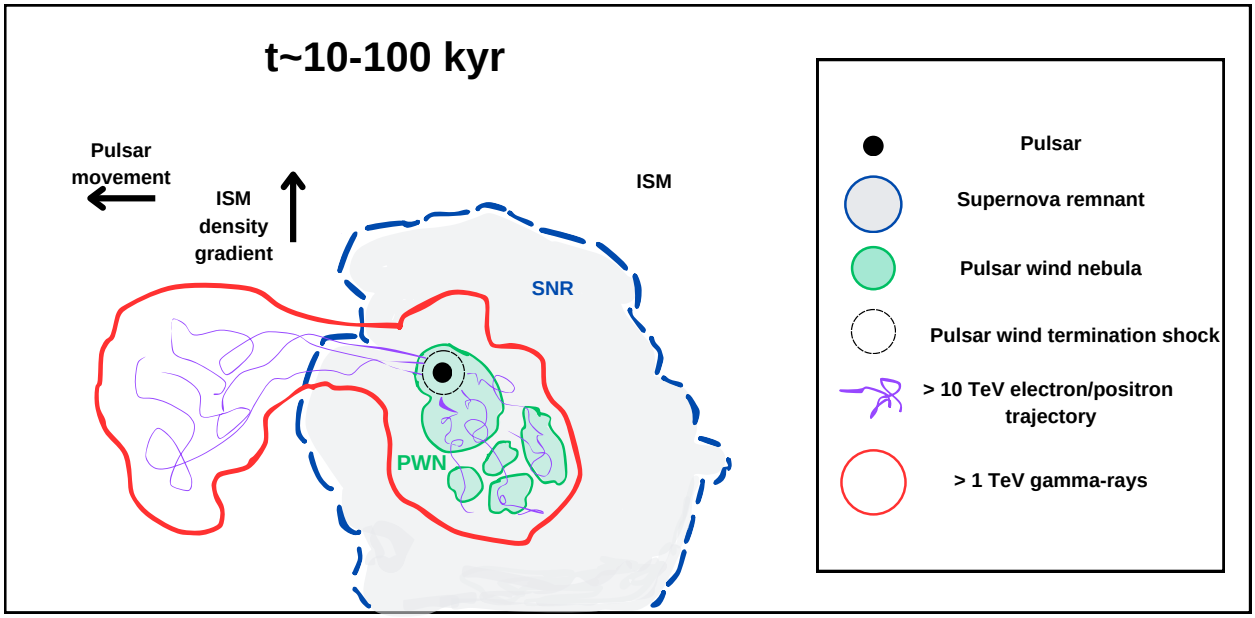

Figure 8: The PWN+SNR systems evolution between ∼10-100 kyr, showing diffuse γ-ray emission. This figure is also majorly based on Fig.1 in (Giacinti et al., 2020).

Furthermore, the PWN's expansion is influenced by several other aspects such as the surrounding composition of the ISM in which the SNR expands. So far, the ISM composition was assumed to be mostly following a homogeneous gradient without greater turbulences or regions of different compositions. These aspects can affect the overall structure of the

remaining system and lead to influences on the general morphology of the system. In conclusion, this stage can be described as the phase in which the pulsar starts to escape from its hosting SNR due to its initial kickback velocity. This process also benefits from given density gradients in the present ISM, thus causing a discrepancy between the observable X-ray and γ-ray emission from the region. This eventually leads to different zones of emission, causing X-rays to be present closer to the pulsar and γ-rays to be locatable at larger distances (Giacinti et al., 2020).

1.4.3 TeV Halos ($\gtrapprox$100 kyr)

Once a time duration of $\sim$ 100 kyr has passed since the supernova has occurred, the pulsar is estimated to leave the SNR, thus escaping into the ISM due to the kickback velocity it got in the supernova explosion (Giacinti et al., 2020). This stage is depicted in Fig. 9, together with a smaller cut-out showing a zoomed version of the immediate pulsar region.

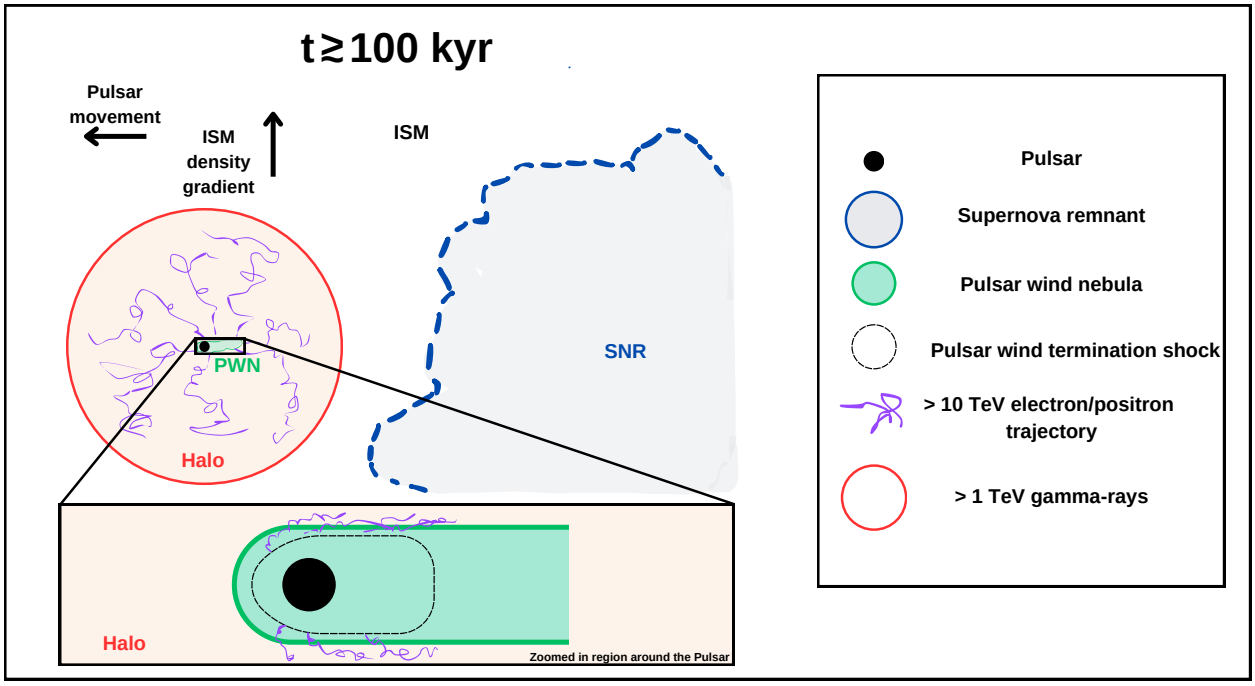

Figure 9: Formation of a TeV halo together with a close up depiction of the PWN system. The figure is again majorly based on Fig.1 in (Giacinti et al., 2020).

In this stage a so-called bow-shock PWN forms around the pulsar, having a much smaller size than the previously seen PWN within the SNR. As this bow-shock system travels in the ISM, it leaves behind a trail with the pulsar's motion dictating the direction of the system. It is then estimated that TeV γ-ray emission can be observed due to interactions of the interstellar magnetic field with escaping electrons and positrons from the pulsar. These interactions can occur within a volume that is much larger than the PWN. They thereby present a reasonable explanation for already observed pulsar structures that exceed the theoretical expectations for PWN sizes. Radio to X-ray emission on the other hand is also still present and is detectable

closely around the pulsar due to the previously mentioned synchrotron emission induced by the rapidly cooling electrons around the pulsar (Giacinti et al., 2020, Sudoh et al., 2019).
However, as the TeV Halo theory is a rather newly derived evolution phase a post supernova system can have, no generalised concept about the formation of such systems exists, mainly due to the fact only so little of them have been observed so far. Thereby, Sudoh et al. (2019) suggest that TeV halos can be formed within the SNR, contrary to the definition by Giacinti et al. (2020). The latter suggests that a TeV halo is only labelled as such in case a process as depicted in Fig. 9 has happened while requiring a non-dominant influence of the relativistic electrons upon the ISM energy density. Furthermore they argue that the TeV halos described by Sudoh et al. (2019) rather represent the second evolutionary stage of the system (i.e., the PWN+SNR diffuse scheme as depicted in Fig. 8). It is therefore decided to use their definition of a TeV halo, as even though their categorisation rejects a more optimistic TeV halo population, it nevertheless implies a more detailed categorisation than Sudoh et al. (2019) does.
At last it is important to mention that the here depicted evolution of the system must not follow a symmetric shape, but can appear diffuse and filamentary. Additionally, the population of electrons and positrons at highest energies is depending on the pulsars themselves, thus making the fraction of accelerated electrons and positrons most possibly uneven (Giacinti et al., 2020).

1.5 Atmospheric particle interactions & a detection method

It is not possible to measure cosmic or γ-rays from Earth's surface directly, as said particles interact with the Earth's atmosphere. However, the need for ground-based measurements lies within the limited area a space operated telescope has, e.g., the Large Area Telescope (LAT) on board of the Fermi satellite. The LAT measures electromagnetic showers produced within its build-in calorimeter. These showers then arise from electrons and positrons that were formed due to pair conversion of incident γ-rays that interacted with a thin tungsten foil. The reason to use this kind of material lies within its high Z number, which increases the probability of a pair conversion while keeping this layer as small as possible to avoid multiple scattering processes. Thereby, the LAT has an effective area at normal incidence of $\sim 1\ \mathrm{m}^2$, which restricts its ability to detect high-energy γ-rays, as their flux decreases with increasing energy (Atwood et al., 2009).
Thereby using ground-based telescopes gives a more realistic access to larger collection areas, thus allowing to search for fainter sources as it could be done for smaller areas (Hinton et al., 2009). Therefore this chapter deals with the interactions within our atmosphere as well as the method of Imaging Atmospheric Cherenkov Telescopes (IACT's), which allow to measure high energy γ-rays via ground stationed facilities.

1.5.1 Extensive air showers

Once a high-energy particle enters the atmosphere, it undergoes interaction processes leading to so-called extensive air showers (EAS). There are two kinds of EAS that can occur:

1. **Electromagnetic (EM) air showers:**

   High-energy photons undergo pair production in the Coulomb field of an atmospheric atom/molecule, producing an electron-positron pair. The electrons and positrons are then undergoing Bremsstrahlung leading to production of secondary photons. These secondary photons are then able to produce secondary electrons and positrons[3] which lead to further photons due to Bremsstrahlung. This cascading effect continues until a critical energy E_c is reached. After this point, the energy losses due to ionisation are more dominant than Bremsstrahlung effects (De Angelis et al., 2018; Jardin-Blicq, 2019).

2. **Hadronic air showers:**

   Contrary to EM shower, hadronic showers are characterised by interactions governed by the strong force at their initial point of interaction. Thereby, charged and neutral pions as well as nucleons and more exotic particles like Kaons are produced once a cosmic ray (e.g. protons, α) interacts with an atmospheric nucleus. Neutral pions make up about $1/3$ of the total pion population and decay into two photons. Photons that are thereby produced are then capable of inducing an EM shower themselves. Charged pions and Kaons typically decay into muons and muon neutrinos (De Angelis et al., 2018; Jardin-Blicq, 2019).

Both processes have in common that they produce more particles the further they travel within the atmosphere[4]. Typically one can distinguish between them due to their shape, as hadronic showers tend to be less well defined as they tend to have a higher possibility of scattering and the fact that strong interactions happen only under a certain angle (De Angelis et al., 2018).

[3]It is worth noticing that secondary photons can undergo Compton scattering processes at lower energies.
[4]In this instance the atmosphere can be seen as a calorimeter.

1.5.2 Imaging Atmospheric Cherenkov Telescopes

Since the particles produced by EAS are travelling with a velocity faster than the speed of light in air, they produce Cherenkov radiation (see Fig. 10).

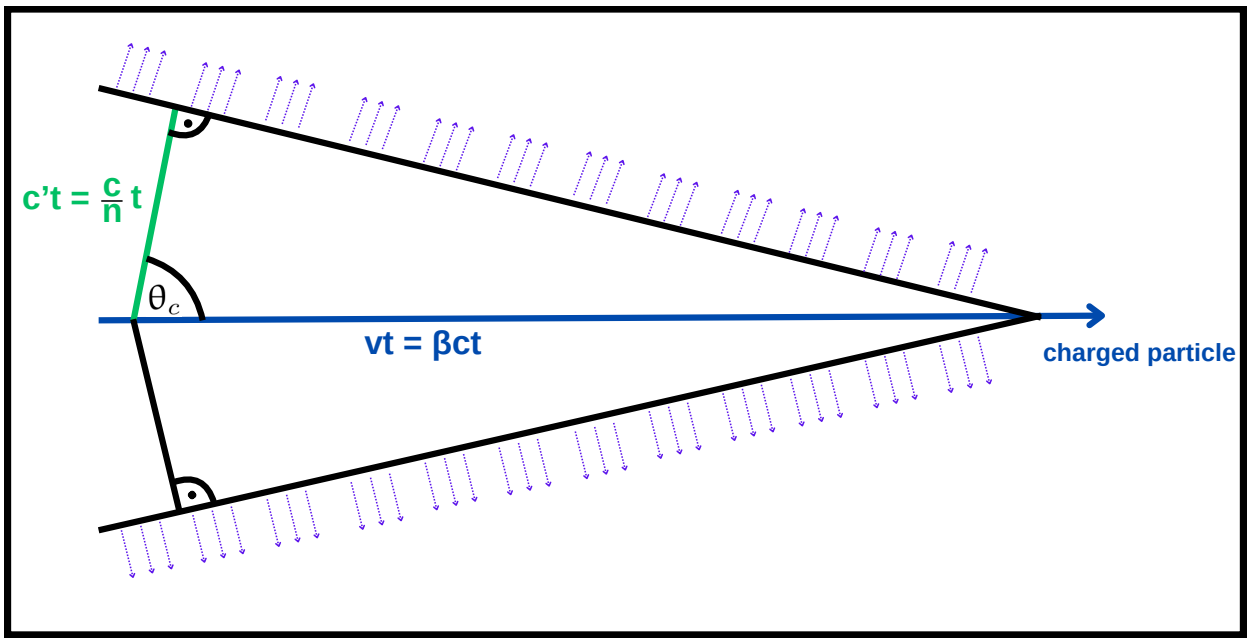

Figure 10: Schematic depiction of the Cherenkov radiation emitted by a charged particle travelling through a given medium.

This radiation is emitted in a cone like shape with an opening angle (De Angelis et al., 2018)

$$\cos(\theta_c) = \frac{c't}{vt} = \frac{1}{n\beta}, \quad \text{with } \beta = \frac{v}{c}, \tag{5}$$

where n is the refractive index of the medium. Thereby, the emitted Cherenkov radiation serves best for the purpose of a detectable radiation caused by incident particle interactions within the Earth's atmosphere. However, due to the main Cherenkov emission happening within the first 20 m of a shower, a cone produced by a shower of 1 TeV has a radius of 120 m (see Fig. 11). Therefore, detectors that want to measure Cherenkov radiation must typically cover these areas and are preferably located in higher latitudes. IACTs collect Cherenkov light by means of a large optical reflector in order to focus the light on a set of photomultipliers (PMTs). The subsequent signal is then send to a set of triggers, which determine whether or not the signal is above a threshold, therefore preventing false signal measurements (De Angelis et al., 2018).

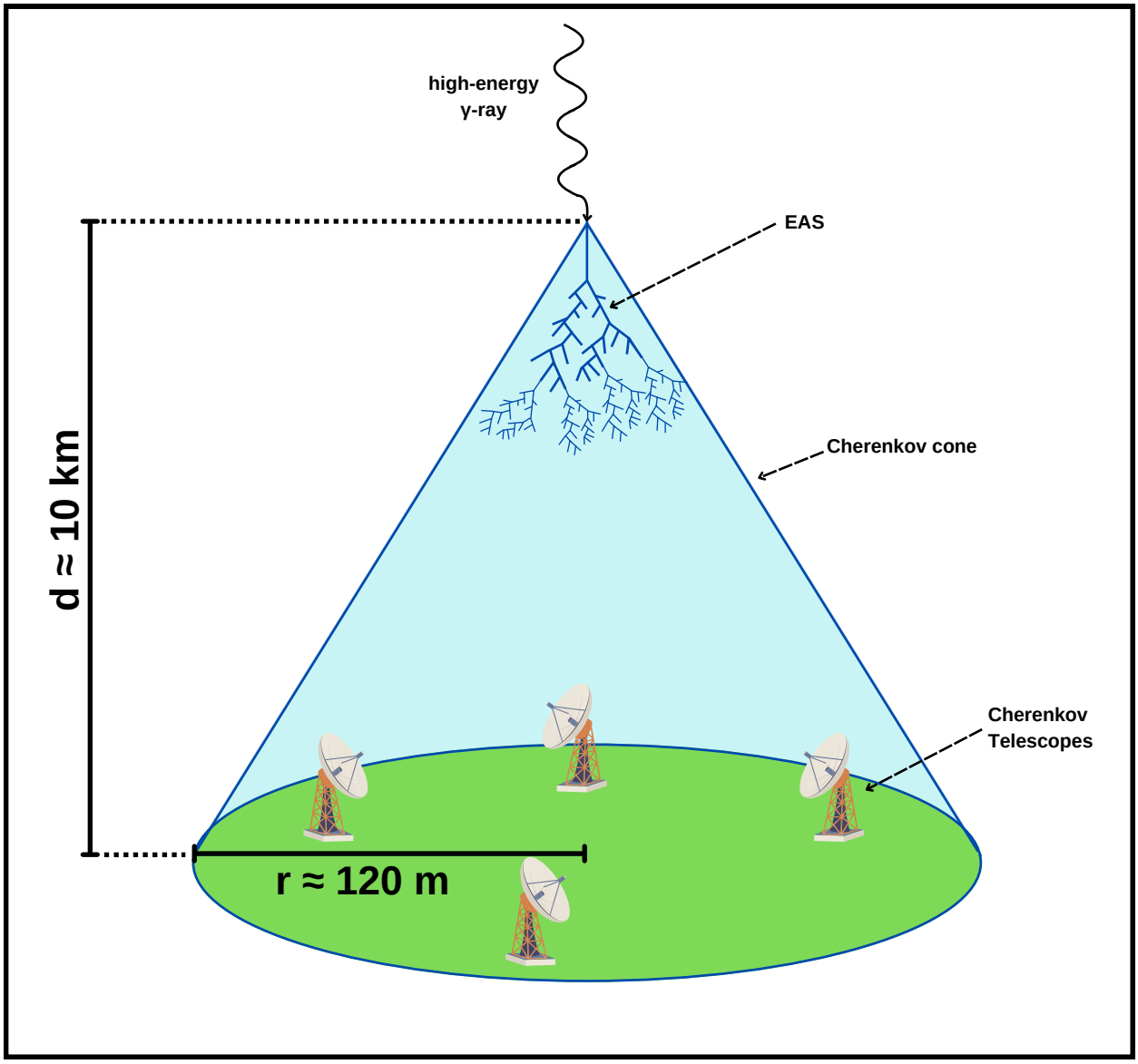

Figure 11: Demonstrative depiction of the shower development caused by an incident γ-ray. The Cherenkov light is distributed in a cone like shape, where the telescopes need to be placed inside.

If a signal is sufficient enough it is further transported to a data acquisition system with a typical time resolution of 1 ns. Typically IACT facilities consist of several individual telescopes, as this improves not only the detection of the shower itself, but also guarantees that events are not recorded falsely. One can separate such events depending on their initial production particle, therefore allowing a separation between photon and hadron like events. Thereby, photon like induced events have a thin elliptic structure, whereas hadronic events tend to be more scattered and isotropic. However, as the Cherenkov light emission begins at $\sim$ 10 km, reaching its maximum at $\sim$ 8 km (initial $E_\gamma = 1$ TeV) and a subsequently decrease in strength in a non linear manner, IACTs need to be build in higher located regions as previously mentioned (De Angelis et al., 2018).

2 The High energy stereoscopic system (H.E.S.S) telescope array

The H.E.S.S. telescope array is stationed in the Khomas Highland Namibia (altitude $\sim$ 1.8 km) and capable of measuring high energy γ-ray induced Cherenkov light. As this light is produced within the atmosphere, stable atmospheric conditions are essential for successful measurements, as well as no light pollution, which is the reason for the choice of this region. Throughout the year, the Khomas Highland shows little to no rain or snow periods and overall mild temperatures (Pühlhofer, Leuschner, et al., 2024).
Therefore, a quick overview of the changes that were made throughout its existence are first given, followed by a description of how the data that has been acquired is further handled.

2.1 H.E.S.S. telescope site throughout the years

The H.E.S.S. telescope array has been in operation for over 20 years in which it has gone through different cycles of hardware changes. This section therefore provides a brief overview of the main features that categorise the different phases that led to the current state of operational capabilities. In addition, an explanation of the central trigger system is given, as it also serves to categorize the different observation modes that the array can perform.

2.1.1 HESS I era

The array itself featured initially four IACTs (CT1-4) (HESSI phase, 2002-2012) with a reflector dish diameter of 13.6 m, consisting of 380 round mirror facets, making up a total collection area of 107 m^2 (Pühlhofer, Leuschner, et al., 2024).
The mirrors are arranged in a Davies-Cotton pattern (see Davies et al., 1957), thus reducing the time spread of the Cherenkov photons (Aharonian, Buckley, et al., 2008).
CT1-4 have the same recording setup, utilising a system of 60 drawers comprised of 16 photomultipliers that are capable to measure the Cherenkov light beam. The signal recorded is further send to a system consisting of low and high gain acquisition channels, connected to samplers, transferring the signal to an Analogue to Digital Converter (ADC) (Aharonian, Akhperjanian, Aye, et al., 2004).

2.1.2 HESS II era

The installation of a fifth telescope (CT5) with a reflector dish diameter of 36 m marks the next phase of the array (HESSII phase 2012-2016). CT5 consists of 876 hexagonal mirror facets making up a total parabolic collection area of $\sim$600 m^2, which is capable of reflecting Cherenkov light towards the camera system (2048 PMTs). Contrary to the already used Davies-Cotton layout, a parabolic setup allows for smaller differences of the photon arrival time in the focal plane (Cornils et al., 2005; Gottschall et al., 2015).

2.1.3 HESS Iu era

In 2016, the cameras of CT1-4 received an upgrade (HESSIu phase) to newer models, in order to reduce the deadtime of the system. Another reason for the upgrade was that a considerable part of the equipment has been worn out or was simply not produced any more. Concerning the electronics, only the PMTs together with their power units were kept, mostly due to the high cost of acquisition and their resilience compared to local weather conditions (Ashton et al., 2020).

2.1.4 CT5 FlashCam installation

The last change of hardware was made in 2019 and involved the usage of a FlashCam camera, which consists of a photon detector plane (PDP), readout electronics, and a data acquisition system. The PDP is kept at a constant temperature of 30° through a water cooling and has build-in pre-amplifiers, allowing direct signal processing. There are a total of 147 PDP modules inside the FlashCam camera, therefore allowing a preciser capture of Cherenkov emission through 1758 active usable pixel channels (Pühlhofer, Barcelo, et al., 2019; Bi et al., 2021).

2.1.5 Trigger system

In order to measure EAS, the H.E.S.S. site uses a central trigger system (CTS) to achieve a coincident measurement of a signal. Any triggering measurement in CT1-5 is directly send to the CTS. Should an event be first recorded by one of the CT1-4 arrays, the CTS only triggers CT5 in case that at least two of CT1-4 measure that event (*stereo* mode). On the other hand, if CT5 triggers an event first (which is typically the case since CT5 records up to 70% of the events itself), the CTS will accept the signal if only one of CT1-4 registers the same event (*hybrid* mode) (Pühlhofer, Leuschner, et al., 2024).

2.2 Data production chain

In the case that an event has been measured in either of the modes introduced in section 2.1.5, a post data handling production chain is now imposed on the data. Thereby, a set of different calibration cuts are applied, each representing a so-called data level (DL), reaching from the initial raw output (DL0) up to the final analysable dataset (DL4). This section covers the basic outline of how an event that is measured by H.E.S.S. goes through this reduction chain. A thorough discussion can be found in (Aharonian, Akhperjanian, Aye, et al., 2004; Aharonian, Akhperjanian, Bazer-Bachi, et al., 2006; and Nigro et al., 2021; as well as Parsons et al., 2014).

2.2.1 Calibration: DL0 - DL1

In this stage the raw measured data (DL0) is converted into units of photoelectrons and corrections due to systematic uncertainties need to be applied. This section therefore covers how an arriving signal in the PMTs is treated further and which assumptions are made to convert a measured current into a usable signal. Furthermore, possible causes for systematics that are arising due to technical limitations, as well as physical sources, are presented.
This section follows the discussion in (Aharonian, Akhperjanian, Aye, et al., 2004).

1. **Signal conversion (Aharonian, Akhperjanian, Aye, et al., 2004):**

   The recorded PMT signal is first transformed into a voltage via a resistor before it is split between a low gain (LG) and high gain (LG) channel (see Fig. 2 by Aharonian, Akhperjanian, Aye, et al. (2004)). The signal then passes analogue ring samplers (ARS) before the signals are rematched using a multiplexor that is connected to an analogue to digital converter (ADC). The LG and HG amplitudes are given by

   $$A^{\mathrm{HG}} = \frac{\mathrm{ADC}^{\mathrm{HG}} - P^{\mathrm{HG}}}{\gamma_e^{\mathrm{ADC}}} \cdot \mathrm{FF} \tag{6}$$

   $$A^{\mathrm{LG}} = \frac{\mathrm{ADC}^{\mathrm{LG}} - P^{\mathrm{LG}}}{\gamma_e^{\mathrm{ADC}}} \cdot \mathrm{FF} \cdot \frac{\mathrm{HG}}{\mathrm{LG}}. \tag{7}$$

   Here, the parameters denote the following:

   - **Pedestal positions** $P^{\mathrm{HG}}, P^{\mathrm{LG}}$:

     The pedestal positions are defined as the ADC's mean value during measurements where no Cherenkov light is recorded, i.e., dark current measurements.

   - **Conversion factor** γ_e^{ADC}:

     In order to convert the ADC signal into units of photoelectrons (p.e.) the conversion factor γ_e^{ADC} is needed. It takes the PMT gain, signal amplification, and also the integration in ARS into account.

   - **Flat field coefficient** FF:

     The FF coefficient is derived during special calibration runs and accounts for inhomogeneities within the camera pixels, as they do not record events evenly.

   - **High gain to low gain amplification ratio** HG/LG.

     This factor is needed to account for the different p.e. rates the LG and HG channel capture. Thereby the HG can be used until 150 p.e., whereas the LG is used for >200 p.e. values. In case that values in between this range occur, the amplitude is calculated via

     $$A = (1 - \epsilon) \cdot A^{\mathrm{HG}} + \epsilon \cdot A^{\mathrm{LG}}, \text{ with } \epsilon \approx \frac{A^{\mathrm{HG}} - 150}{200 - 150}. \tag{8}$$

2. **Systematics affecting pixels (Aharonian, Akhperjanian, Aye, et al., 2004):**

   There are basically two different kinds of pixel systematics that can occur during a measurement. One being that some pixel channels are simply not usable due to an unlocked ARS, an effect randomly appearing when the power is switched on. Additionally, signals with a very high voltage, as well as signals with less than 30 p.e. rate or signals with very unusual high p.e. frequency (compared to surrounding pixels) are excluded. Furthermore, signals can be rejected due to their high night-sky background (NSB) value. As discussed in section 1.5.2, IACTs heavily rely on the calometric nature of the atmosphere, which can become a problem when the light gets attenuated due to atmospheric changes. Thereby, not only weather aspects like the cloudiness or temperature play a role, but also contaminations due to a bright night-sky. Therefore if a NSB value of 250 MHz is measured, all pixels above this level are automatically excluded, contamination however can not fully be excluded.

2.2.2 Event reconstruction & categorisation: DL1 - DL2

In order to process the data further, it is vital to differentiate between hadronic induced EAS and γ-ray ones. The original method by Hillas (1985) uses Monte Carlo simulations to model the shower development and its subsequent pattern visible on the telescope. Therefore, so-called Hillas parameters are used, which are dependent on the light shower's width, length, and orientation on the images. By applying these cuts, around 60-70% of the γ-ray showers could be accepted as such, while only 1-2% of the proton background where accepted (Hillas, 1985).
However, a more modernly developed approach by Parsons et al. (2014) uses an Image Pixel-wise fit for Atmospheric Cherenkov Telescopes (`ImPACT`) to model the different patterns. Thereby, a likelihood fit of DL1 objects upon template air showers derived by Monte-Carlo (MC) simulations is made, while also accounting for the telescope response by using ray-tracing. This method requires enormous computing power, but has the advantage that it distinguishes very precisely between the EAS types mentioned above (Parsons et al., 2014). Generally, a categorisation using `ImPACT` can be done in three different ways[5]: *hard*, *standard*, and *loose* cuts. In general for most sources *standard* cuts suffice and offer a good compromise between the two other alternatives. Using *loose* cuts is mostly relevant only for bright extragalactic sources[6], while the choice of using *hard* cuts depends on the emission type that is expected from the source. Thereby, these cuts have been optimized for sources that show fluxes of around 1% of the Crab nebula (Pühlhofer, Leuschner, et al., 2024; Aharonian, Akhperjanian, Bazer-Bachi, et al., 2006).

[5]These cuts are also applied in the method described by Hillas, and thus not exclusive to `ImPACT`.
[6]Such sources are typically affected by extragalactic background light, which is characterised by higher energies (Pühlhofer, Leuschner, et al., 2024).

2.2.3 Instrument response function and γ-ray event files: DL3

With the choice on cuts set, one can produce DL3 files (usually in standard `FITS` format (Wells et al., 1979)), which are objects consisting of a γ-ray event list together with its Instrument Response Function (IRF). The latter describes the response of the telescope to a γ-ray with a certain energy, whereas the γ-ray event list contains the reconstructed data (Donath et al., 2023). The IRF can be written as (Donath et al., 2023)

$$R(p, E|p_{\text{true}}, E_{\text{true}}) = A_{\text{eff}}(p_{\text{true}}, E_{\text{true}}) \cdot PSF(p|p_{\text{true}}, E_{\text{true}}) \cdot E_{\text{disp}}(E|p_{\text{true}}, E_{\text{true}}), \quad (9)$$

with the effective area $A_{\text{eff}}(p_{\text{true}}, E_{\text{true}})$, describing the effective sky area in which particles are collected depending on their true energy E_{true} and position p_{true}. The Point Spread Function $PSF(p|p_{\text{true}}, E_{\text{true}})$ gives the probability density of measuring the position p while the true position/energy is at p_{true} and E_{true}. The energy dispersion $E_{\text{disp}}(E|p_{\text{true}}, E_{\text{true}})$ characterises the probability of finding a reconstructed photon at energy E when its true position/energy is actually p_{true} and E_{true} (Donath et al., 2023).
The IRF is essential to describe the expected number of detected events (Gammapy, 2024)

$$N(p, E)\, dp\, dE = t_{\text{obs}} \int_{E_{\text{true}}} dE_{\text{true}} \int_{p_{\text{true}}} dp_{\text{true}}\, R(p, E|p_{\text{true}}, E_{\text{true}}) \cdot \Phi(p_{\text{true}}, E_{\text{true}}), \quad (10)$$

with $\Phi(p_{\text{true}}, E_{\text{true}})$ being the sky flux model, and the observation time t_{obs}.
In order to create and perform basic analysis using the DL3 data, this work majorly uses common python packages alongside `Gammapy v1.2` (Donath et al., 2023; Acero et al., 2024), as well as `GAMERA` (Hahn, Romoli, et al., 2022), which is an open source C++/python package.

2.2.4 Background reduction of γ-ray like events

The last step required before starting the actual analysis of H.E.S.S. data lies within the so-called background reduction. This is necessary, as even though cosmic-ray events are filtered out during the `ImPACT` analysis, some γ-ray like events still remain within the DL3 data. Thereby, the aim is it to get the excess counts through (Berge et al., 2007)

$$N_{\text{Excess}} = N_{\text{On}} - \alpha N_{\text{Off}}, \quad (11)$$

where N_{On} are the counts within the region of interest (ROI), N_{Off} the counts in a control region, and α the (telescope's system) acceptance, which is a factor that is defined as the probability of accepting a γ-ray like given a certain position and energy within the FoV. In general, the acceptance depends on several factors, namely the position within the ROI, the zenith and azimuth angle, the reconstructed primary energy, the time of observation and the sky coordinates (due to NSB). Therefore, when regarding the H.E.S.S. telescope's FoV of $\sim 5^\circ$, deviations within the acceptance can occur, but overall remain within 5% (Berge et al., 2007).
This work uses the FoV and ring background reduction methods, as well as the recently developed run-matching approach by Wach et al. (2024). The FOV model uses a template created from archival observations and is then folded with the effective area (Mohrmann et al., 2019).

The ring background, on the other hand, uses sample positions around which a ring with adjustable width is placed, thus calculating the acceptance via (Berge et al., 2007)

$$\alpha \approx \frac{\theta_{\text{solid}}}{A_{\text{region}}}, \tag{12}$$

where θ_{opening} is the solid angle of the ring, and A_{region} being the trial source area. However, since the ring typically covers different sections of the sky region, the acceptance must not be assumed to be constant, as varying offsets arise from the different observation positions. To counteract this problem, a correction factor is required, which must be calculated individually for each region (Berge et al., 2007).
However, the methods described by Berge et al. (2007) are not suitable for analysing highly extended sources where no γ-ray free region might be available. In such cases one can use the previously mentioned ON-OFF run-matching method to account for the background. This method was developed to analyse extended TeV γ-ray emission regions using H.E.S.S. data by matching ON and OFF runs through observational conditions. Thereby, a so-called fractional run deviation coefficient is computed for every observation by using the parameters describing the telescope response and atmospheric conditions (see also Table 2 in Wach et al. (2024)). Therefore, every ON run can be matched to an OFF run under similar observational conditions, provided there is a time period with similar optical efficiency that has Galactic latitude $|b| \geq 10$. Furthermore, it is required that the same telescopes have participated in both ON and OFF runs. The background is then estimated from fitting of the above mentioned FoV background template upon the OFF run. This process is then done for every ON-OFF pair, thus making it a good tool in regions where traditional estimations fail due to a high γ-ray emission throughout the entire FoV (Wach et al., 2024).

3 Analysis of the extended PSR B1046-58 region

First discovered by Johnston et al. (1992), PSR B1046-58 lies above of the Eta Carinae binary system which is known for frequently occurring outbreaks every ∼5.54 years (Iping et al., 2005). The basic parameters of the pulsar are shown in Table 1 and are taken from the **A**ustralia **T**elescope **N**ational **F**acility (ATNF) catalogue (Manchester et al., 2005; ATNF Catalogue, 2025c). The pulsar has a characteristic age qualifying it to be in the intermediate phase of post supernova evolution systems. Furthermore, as the pulsar has a spin-down luminosity $\geq 4 \cdot 10^{36}$ erg s^{-1}, it is likely that it powers and sustains a PWN (Gaensler et al., 2006). This work aims to detect the PWN around the pulsar, following suggestions found by Jardin-Blicq (2019), which reported extended TeV emission to be present around the pulsar. For this purpose the HESS data of the region is analysed. The DL3 data from HESSI phase for PSR B1046-58 are in `FITS` format available and pre-produced by the Erlangen Centre for Astroparticle Physics (ECAP) using the above mentioned (`ImPACT`) algorithm. The total amount of data taken on the region amounts to 73 observation runs.

Table 1: Basic parameters of PSR B1046-58 taken from the ATNF pulsar catalogue (Manchester et al., 2005; ATNF Catalogue, 2025c).

Parameter	Value	Unit
Spin period (P)	124	ms
Period derivative ($\dot{P}$)	$9.61 \cdot 10^{-14}$	s s^{-1}
Distance (D)	2.9	kpc
Characteristic age (τ_c)	20.4	kyr
Surface magnetic field (B)	$3.49 \cdot 10^{12}$	G
Spin-down luminosity ($\dot{E}$)	$2.0 \cdot 10^{36}$	erg s^{-1}
R.A. (J2000)	10:48:13.05	hh:mm:ss.s
Dec (J2000)	-58:32:06.2	dd:mm:ss.s
Distance (d)	2.9	kpc

3.1 Dataset cuts

First, an analysis is performed using all previously discussed background models of section 2.2.4. However, as already mentioned, the ROI is near the Eta Carinae Nebula that undergoes so-called periastron phases which are taken out of the analysis, as X-ray measurements indicate a varying flux during these phases (Corcoran et al., 2017). Although Steinmassl et al. (2023) suggests that there is no major impact upon measured TeV flux during these periods, which is contrary to earlier statements by Abdalla, Adam, et al. (2020), the decision is to exclude these observation runs. Fig. 12 shows that an additional set of observations shows very high NSB values which also need to be excluded from the analysis. As stated earlier, high NSB values influence the measurements by contaminating the Cherenkov light with non divisible light from other non γ-ray sources.

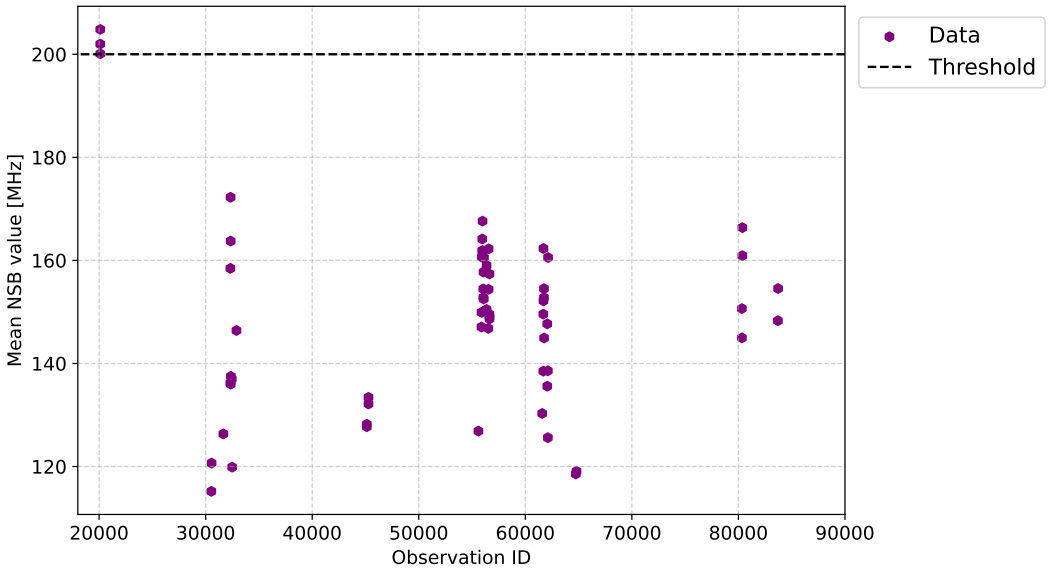

Figure 12: Mean NSB value across all participating telescopes over their observation ID. Note that the NSB values shown here represent the average value across all used telescopes, i.e., the mean value for CT1-4.

Even though no values in Fig. 12 are above 250 MHz, it is decided to cut the observations around run ID 20000, as they are the only runs above a mean NSB value of 200 MHz. Another important parameter that needs to be considered is the so-called *Cherenkov transparency coefficient*, which can be best understood as a value describing the atmospheric conditions is calculated through (Hahn, de los Reyes, et al., 2014)

$$\tau = \frac{1}{N \cdot k_N} \sum_i t_i = \frac{1}{N \cdot k_N} \cdot \sum_i \frac{R_i^{\frac{1}{1.7-\Delta}}}{\mu_i \cdot g_i} \tag{13}$$

where N is the number of telescopes, k_N is a scaling factor depending on the telescope multiplicity, R_i are the trigger rates, μ_i is the muon efficiency, g_i the average pixel gain, and Δ is used to take higher order corrections into account (Hahn, de los Reyes, et al., 2014). The muon efficiency is an important parameter, as muon rings can appear on the detectors in a ring shape. Therefore this efficiency describes the number of measured photo-electrons per incident photon, which can be used to describe the quality of a detection (Gaug et al., 2019; Vacanti et al., 1994). Following further discussions by Hahn, de los Reyes, et al. (2014), a transparency coefficient is indicated as representing good atmospheric conditions in case of a value close to one. This is the case for most data that can be seen in Fig. 13, where a significant amount of observations were taken at values between 0.95-1.07. However, as can also be seen, a considerable amount of observations show τ<0.95, which is still acceptable, as data only needs to be cut in case τ<0.8, which is not the case here (Hahn, de los Reyes, et al., 2014).

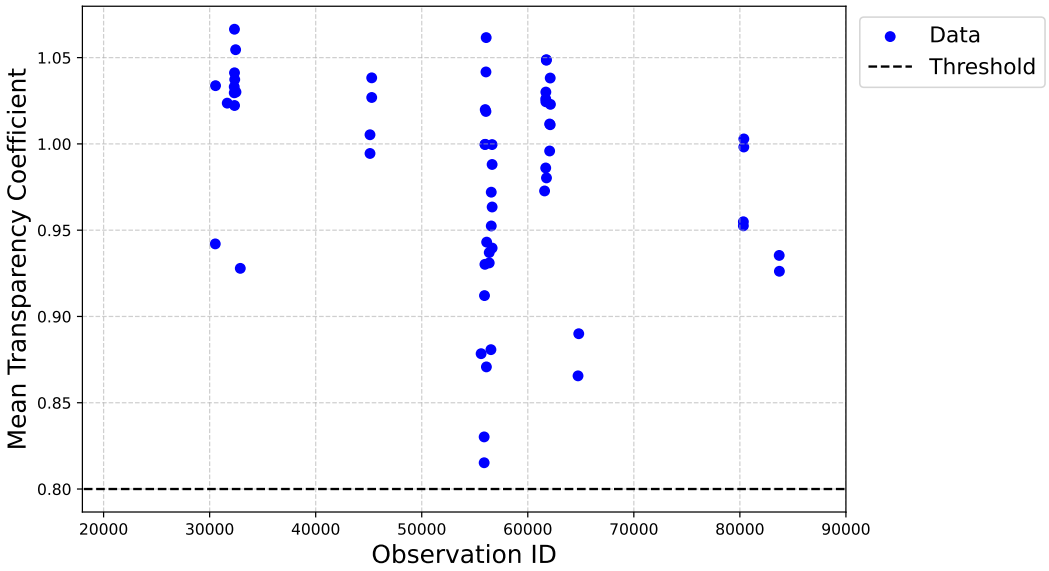

Figure 13: Mean transparency coefficient over observation ID for the 59 runs.

Furthermore, it is decided to use only those runs that have a duration of at least 25min, leading to a further decrease in available runs. Thereby, 59 observations remain when applying all these cuts, leading to an average livetime (i.e., deadtime corrected observation time) of (28.13±0.1) min for each run. Furthermore, it is decided to use only spectral quality produced data (see Aharonian, Akhperjanian, Bazer-Bachi, et al., 2006).
Besides the duration of the runs, it is also important to check the distribution of zenith angles as depicted in Fig. 14. Most runs are located around (39.32±3.76)° with no angles above 60°, which is typically set as a boundary since larger zenith angles can impact the data processing (Benbow et al., 2005; Lu, 2013).

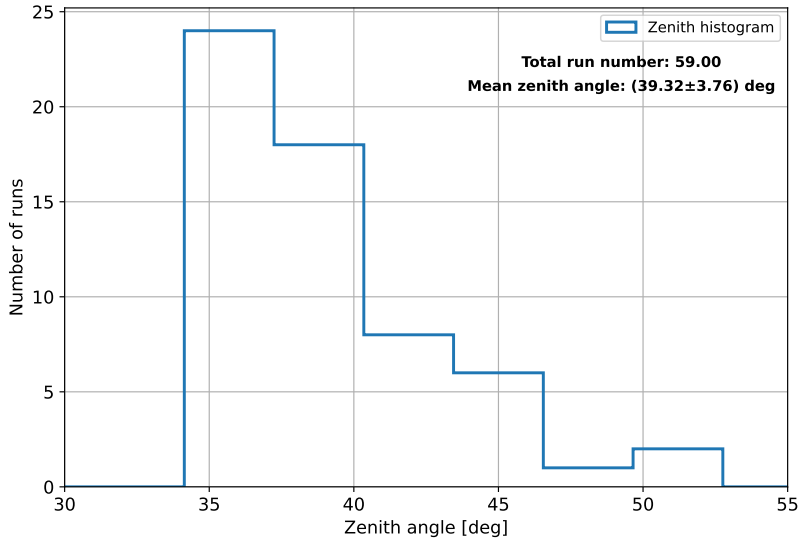

Figure 14: Zenith angle histogram for the remaining 59 observations showing a sharp cut at 38° from which on the counts decrease.

3.2 Background reduction

As the data shows relatively high NSB values, it is decided to set a lower energy threshold based on the DL3 energy dispersion and effective area data. Using the energy dispersion IRF, all events with an energy bias percentage above $^{E_{\mathrm{Reco}}-E_{\mathrm{True}}}/_{E_{\mathrm{True}}} = 5\%$ are discarded, taking then the first energy value above this bias energy as threshold. When using the effective area, the background peak is used as the threshold and only data after the spectrum's turnover point is further used. Finally, both obtained energy threshold lists are compared with each other and the highest energy that occurs in both lists is taken as the lower safe threshold for the actual background reduction. Using this method, the lower energy threshold is calculated to be 0.82 TeV, which is now utilized during the background reduction process.
For the DL4 data production, an empty map of size 8°×8° with pixel size 0.01° is created, and corresponding logarithmically scaled energy axes (in range 0.1-100 TeV) are created. In order avoid source contamination during the background model fitting, a set of exclusion masks are created and applied during the reduction process (see Fig. 15 for an overview). The central mask size is based on the emission as seen in Fig. 4.19 by Jardin-Blicq (2019) and has a radius of 1.8°. Additionally, all known and potential HESS sources within a 5° radius around the map centre are excluded in order to avoid inadvertently including γ-ray sources.

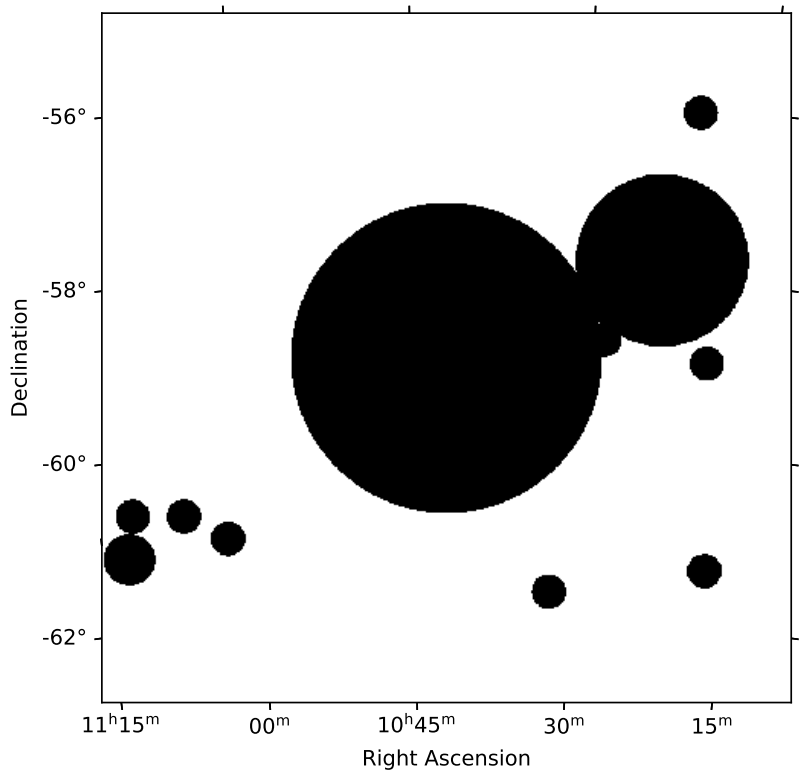

Figure 15: Exclusion masks set upon the dataset during the background reduction processes.

3.2.1 FoV background reduction

As previously discussed, the FoV method uses a normalisation upon the non excluded regions to estimate the background counts. Therefore, `Gammapy` uses a normed spectral model of the form

$$\phi_{\text{norm}} = \frac{dN}{dE} = \phi_0 \cdot \left(\frac{E}{E_0}\right)^{-\Gamma}, \; E_0 = 1 \text{ TeV}, \tag{14}$$

which is fitted upon each DL3 object that are then stacked upon each other. The resulting values for the norm ϕ_0 and tilt Γ can be seen in the histograms depicted in Fig. 16 & 17 . Thereby, a fit using a normal distribution of the form

$$f(x|A, \mu, \sigma) = A \cdot e^{-\frac{1}{2}\left(\frac{x-\mu}{\sigma}\right)^2} \tag{15}$$

is applied. Typically, one expects the tilt to be centred around zero, as a steeper index would imply a source emission, which would then require possible adjustments upon the masked regions.

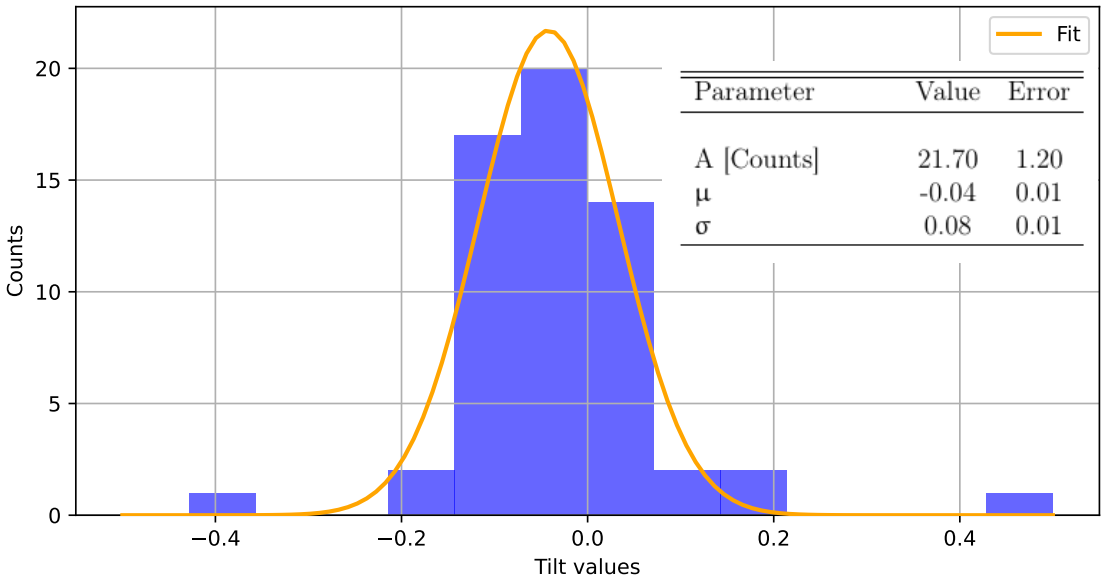

Figure 16: Tilt value histogram together with fit parameters using Eqn. (15).

The norm on the other hand should be centred around one, as this factor represents the uniformity of the spectral model fit, therefore requiring for a theoretical "non-source" region to be equal to one. Therefore, only small corrections are expected to happen in this case, as larger deviations would then indicate source contamination (Mohrmann et al., 2019).
The fit values for the norm and tilt histograms are shown in the individual figures, indicating that the source masks were chosen appropriately, as the tilt is close to zero. The norm value on the other side indicates that there is some cause of non uniformity during the background

reduction occurring. A reason for this could lie within the high NSB values, as a comparison with the transparency coefficient (see Fig. 13) reveals no other observational systematic to be a cause for this. However, as both values are within errors in accordance to the theoretical expectations, further analysis steps can safely be applied.

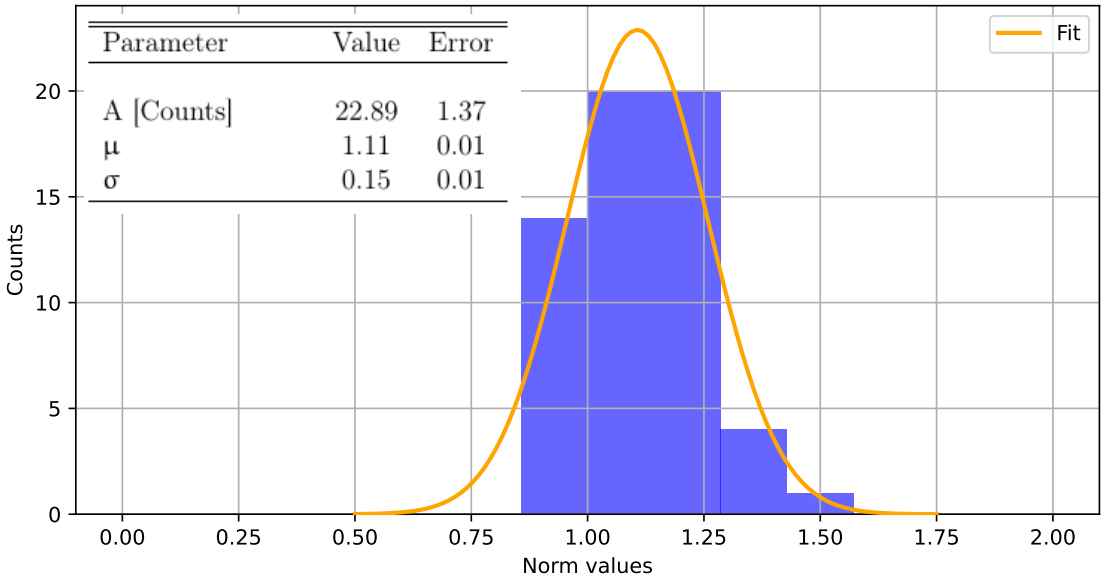

Figure 17: Norm value histogram alongside fit parameters using Eqn. (15).

Finally, a cut on the entire energy dispersion of the stacked dataset is imposed due to the 5% bias requirement, resulting in the lower energy threshold of 0.82 TeV. Fig. 18 shows the energy bias over true energy curve with the grey area representing the excluded data range due to the thresholds set on the individual observation runs.

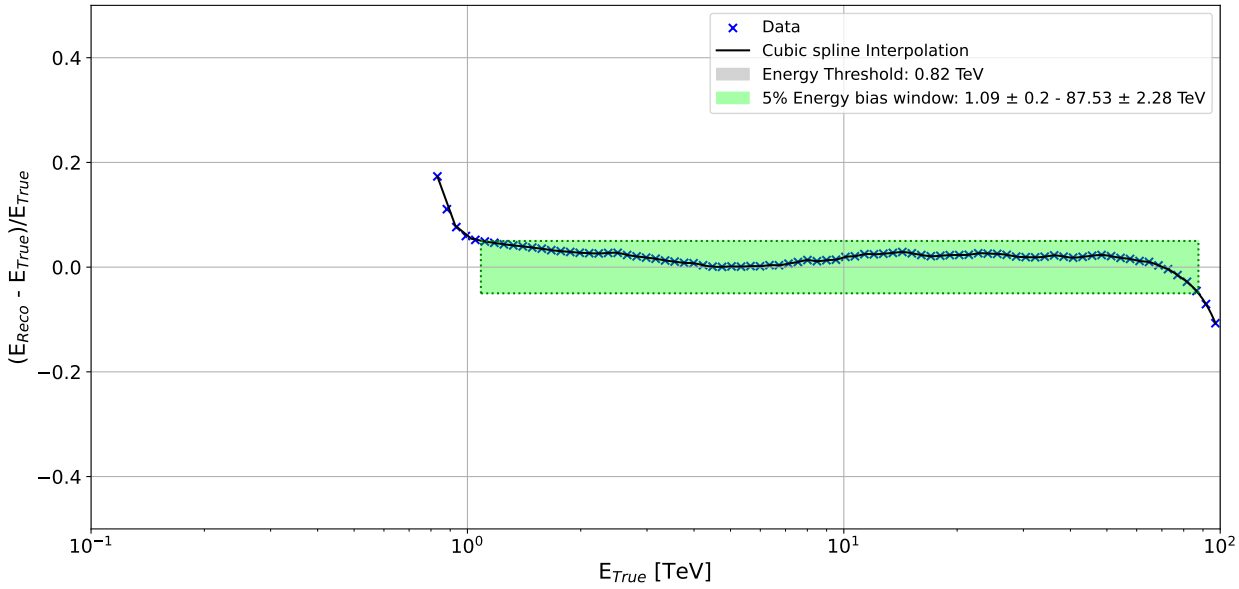

Figure 18: Bias percentage over true energy with indicated energy threshold (grey area) as well as safe bias window (green area). The bias window range is calculated using a cubic spline interpolation upon the data.

Now, in order to restrict the final dataset to be also using only data within the 5% bias range, a cubic spline interpolation using `SciPy` (Virtanen et al., 2020) is made, from which the safe energy window (green box in Fig. 18) is calculated. The reason to do this is that the build in `Gammapy` function uses only the next energy bin it finds, which however, is not ideally in this case. Therefore, using the interpolation guarantees that the bias energy is safely computable, which is necessary, as the choice of including/excluding an energy bin at energies around $\sim$1 TeV can make a difference (logarithmic energy axes). The result of this process is that the safe energy range lies within $E_{\text{low}}^{\text{bias}} = (1.09 \pm 0.20)$ TeV and $E_{\text{high}}^{\text{bias}} = (87.53 \pm 2.28)$ TeV, where a bias percentage error of 1% was assumed. However, due to the bin structure of the energy axes, these values lie exactly within two bins respectively, therefore requiring to choose between one of them. In order to keep the energy range at safe values, it is therefore decided to use the next highest energy bins. Hence, all further analysis is done between 1.16-90 TeV which is uniformly used from now on, except explicitly stated otherwise.
Using the statistics described by Li et al. (1983) then allows one to compute the significance by taking the square root of the test statistic (TS). The resulting $\sqrt{TS}$ map can be seen in Fig. 19, which is computed using a correlation radius of 0.6°. Furthermore, the 5σ contours as well as all known sources (within radius of 2.5° from the centre) reported by the fourth Fermi catalogue 4FGL[7] (Abdollahi et al., 2020) are taken into account.

[7]The catalogue data is extracted using the `gammapy.catalog` sub-package and from this point on if 4FGL is mentioned, the data from this catalogue object is meant (see Donath et al., 2023).

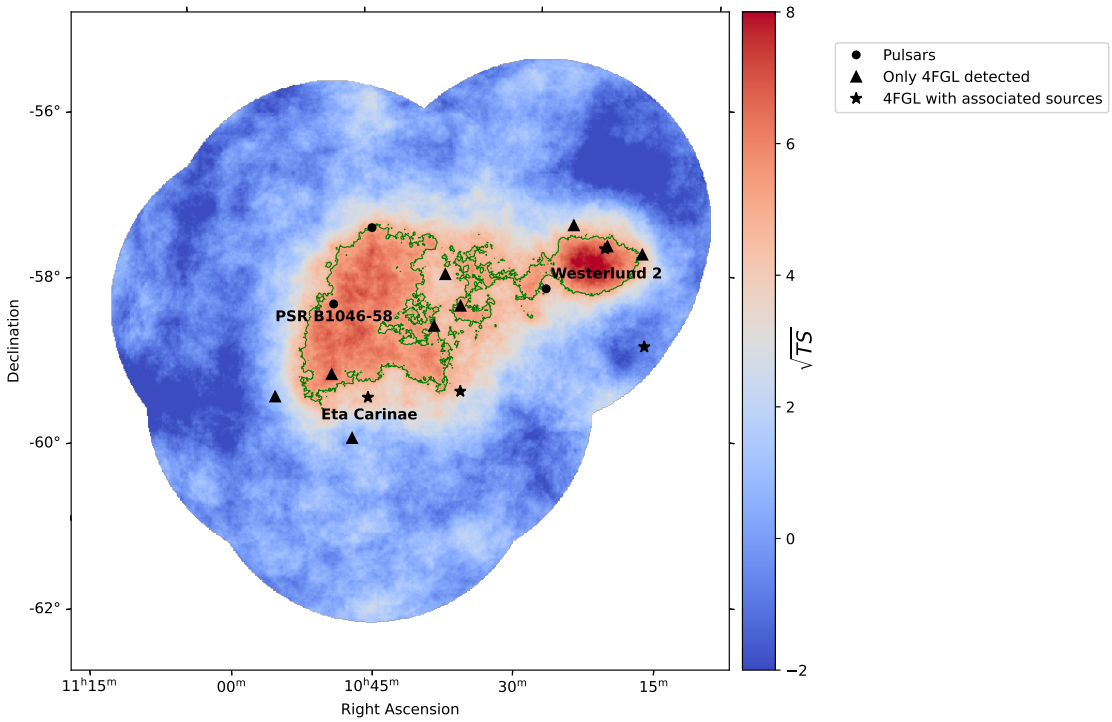

Figure 19: $\sqrt{TS}$ map of the region with 5σ indicated by the green lines as well as all known 4FGL sources within 2.5° radius; the correlation radius is 0.6°. Furthermore, the most important sources in the region are labelled by their common name, i.e., Eta Carinae and Westerlund 2.

The reason to have a first look upon these sources is on the one hand that is easily accessible through the build in catalogues of `gammapy`. On the other hand, a comparison using the other catalogues revealed less sources to be reported in the region, thus making the 4FGL catalogue a good starting point, from which associated sources can then be retraced. In order to identify possible counterparts of the 4FGL sources, this work has made use of the SIMBAD database, CDS, Strasbourg Astronomical Observatory, France (Wenger et al., 2000). If a 4FGL source has a pulsar associated to it, then it is flagged as "Pulsar" in Fig. 19 and the position is taken from the ATNF pulsar catalogue (Manchester et al., 2005, ATNF Catalogue, 2025a). However, in case the 4FGL source is also observed by other telescopes in between the radio to γ-ray domain but has no pulsar associated to it, the term "4FGL with associated source" is used, e.g., for Eta Carniae. Finally, if only 4FGL reported an emission, then the source is tagged with "Only 4FGL detected". Table 2 shows the sources depicted in Fig. 19, with all known HESS counterparts listed in case they have been reported. The table description is:

- 4FGL name: name of the source as listed in the 4FGL catalogue (Abdollahi et al., 2020).
- Associated name: name of associated sources listed by the SIMBAD database (Wenger et al., 2000). In case the associated source is also detected by HESS, then its corresponding name is used.

- R.A. [deg]: right ascension in degree.
- Dec [deg]: declination in degree.
- Flag: information from which source the position is taken. The flag "1" refers to the coordinates listed in the 4FGL catalogue (Abdollahi et al., 2020), whereas "2" is referring to the ones listed by ATNF (Manchester et al., 2005; ATNF Catalogue, 2025a).

Thereby, three pulsars are identified to be counterparts of the 4FGL sources J1028.5-5819, J1044.4-5737, and J1048.2-5832. The former is associated to HESS J1026-582 (PWN), whereas the other two have so far no reported HESS counterpart (Abdalla, Abramowski, et al., 2018). Furthermore, four other sources share already observed counterparts, thereby 4FGL J1045.1-5940 is associated to the most prominent Eta Carinae[8] within the active star forming region of the Carinae Nebula (Smith, 2006; Abdollahi et al., 2022). Furthermore, 4FGL J1036.2-5936 is associated to V* V906 Car, which is a classical Nova (Wenger et al., 2000). The source below the Westerlund 2 region (4FGL J1018.9-5856) is associated to the HESS source HESS J1018-589 A, which is classified as a γ-ray binary and has also been associated to the SNR G284.3-1.8 (Abdalla, Abramowski, et al., 2018). The last remaining associated source is 4FGL J1023.3-5747e, which is associated to the Westerlund 2 region[9], and has the HESS counterpart HESS J1023-575, which is also associated to PSR J1023-5746 (Abdalla, Abramowski, et al., 2018, Abdollahi et al., 2020). This leaves 8 sources out of the 15 within the 2.5° radius around centre that are only detected so far by the 4FGL catalogue.

[8]First observed by Halley (1679), with first reported γ-ray emission from Abdo et al. (2010), and first reported using HESS data by Collaboration et al. (2012).

[9]The cluster was first observed by Westerlund (1961).

Table 2: 4FGL sources within the region and flags describing the origin of the positions. Associated sources were obtained using the SIMBAD database (Wenger et al., 2000).

4FGL name	Associated name	R.A. [deg]	Dec. [deg]	Flag
4FGL J1018.9-5856	HESS J1018-589 A	10:18:57.6	-58:56:24	1
4FGL J1023.3-5747e	HESS J1023-575 Westerlund 2	10:23:19.2	-57:47:24	1
4FGL J1026.2-5731	-	10:26:16.8	-57:31:48	1
4FGL J1028.5-5819	HESS J1026-582	10:28:28.8	-58:19:12	2
4FGL J1036.2-5936	V* V906 Car	10:36:14.4	-59:36:00	1
4FGL J1036.3-5833e	-	10:36:21.6	-58:33:36	1
4FGL J1037.8-5810c	-	10:37:50.4	-58:10:48	1
4FGL J1038.8-5848c	-	10:38:50.4	-58:48:36	1
4FGL J1044.4-5737	PSR J1044-5737	10:44:33.6	-57:37:12	2
4FGL J1045.1-5940	Eta Carinae	10:45:07.2	-59:40:48	1
4FGL J1046.7-6010	-	10:46:43.2	-60:10:12	1
4FGL J1048.2-5832	PSR B1046-58	10:48:12.0	-58:32:24	2
4FGL J1048.5-5923	-	10:48:14.4	-58:32:24	1
4FGL J1054.0-5938	-	10:54:02.4	-59:38:24	1
4FGL J1054.7-6008c	-	10:54:43.2	-60:08:24	1

In order to validate the background reduction, it is useful to plot a histogram of the $\sqrt{TS}$ values with and without exclusion masks applied. Fig. 20 thereby shows that the reduction led to most values outside the exclusion mask to have $|\sqrt{TS}| < 5$, therefore leaving no emission above 5σ to be outside the excluded regions.

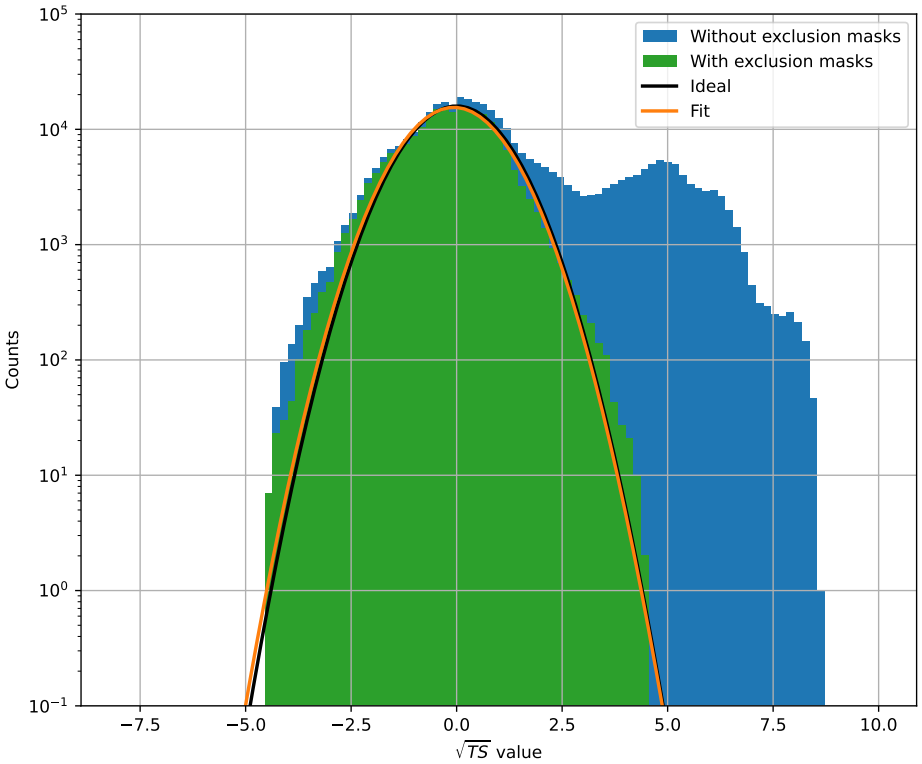

Figure 20: $\sqrt{TS}$ distributions with and without exclusion masks taken into account. A fit using Eqn. (15) is made upon the $\sqrt{TS}$ distribution with masks applied. Additionally, the ideal distribution for post background reduced $\sqrt{TS}$ distributions is shown too.

Table 3: Fit values using Eqn. (15) on the $\sqrt{TS}$ distribution with masks in Fig. 20.

Parameter	Value	Error
A [10^3 Counts]	15.5	0.20
μ	-0.06	0.02
σ	1.01	0.02

Furthermore a fit using Eqn. (15) is made in order to characterise the background reduction more thoroughly (see Table 3 for values). In addition to the fit, its ideal expected distribution is shown using $A_{\text{theo}} = N_{\text{max}}$, where N_{max} is the highest count value of the excluded mask histogram, and $\mu_{\text{theo}} = 0$, $\sigma_{\text{theo}} = 1$, as the counts should be Poisson distributed. Comparing the fitted values for μ, σ to their ideal expectations shows that the background reduction was successful, albeit with having μ being a little bit smaller than expected. This can be traced down to regions in which the background is systematically overestimated, as it is the case for the region above Westerlund 2. In these regions, an overestimated background model leads to areas containing only negative excess (= counts above background level), thus leading to a shift of μ to values below zero while also influencing σ. Taking these aspects into account leads to the conclusion that even though the found values for the posterior $\sqrt{TS}$

distribution come close to the ideal values, they still need to be treated with care. Yet, it can be concluded that the used FoV background model resulted in an adequate estimation, thus granting a sufficient reduction of γ-ray like events during the process. At last it is worth mentioning that the chosen masks or correlation radius must not be the universally best suiting ones, as they relied majorly on the initial assumption of the centre source emission from Jardin-Blicq (2019).

3.2.2 Background model cross-check

Using the same energy threshold algorithm, a cross check using the ring and run-matching background reduction methods is done. This cross-check represents on the one hand a validation for a significant ($> 5\sigma$) source emission by comparing the "traditional" methods of ring and FoV background reduction. On the other hand this best serves another validation of the run-matching approach, ensuring that the application of this method is done correctly. This is important, especially for the data taken from Monogem, for which (as will later be discussed) the traditional methods will not work.

Ring background reduction

Using the exclusion masks of Fig. 15 and the 5% bias energy method during the ring background reduction method (inner ring radius = 1.5°, width=0.5°), the map depicted in Fig. 21 arises. The map is computed by using a correlation radius of 0.6° and applying the energy bounds between 1.16-90 TeV. Furthermore, all sources from Fig. 19 as well as the 5σ contours of the FoV map are depicted too, revealing that the region above 5σ is now smaller. In comparison to the FoV map, a different shape arises, leading the main detectable emission to be around the left bulk of the centre region as well as Westerlund 2. Yet, the general character of the extended emission still persists, albeit being now below 5σ for the region in between.

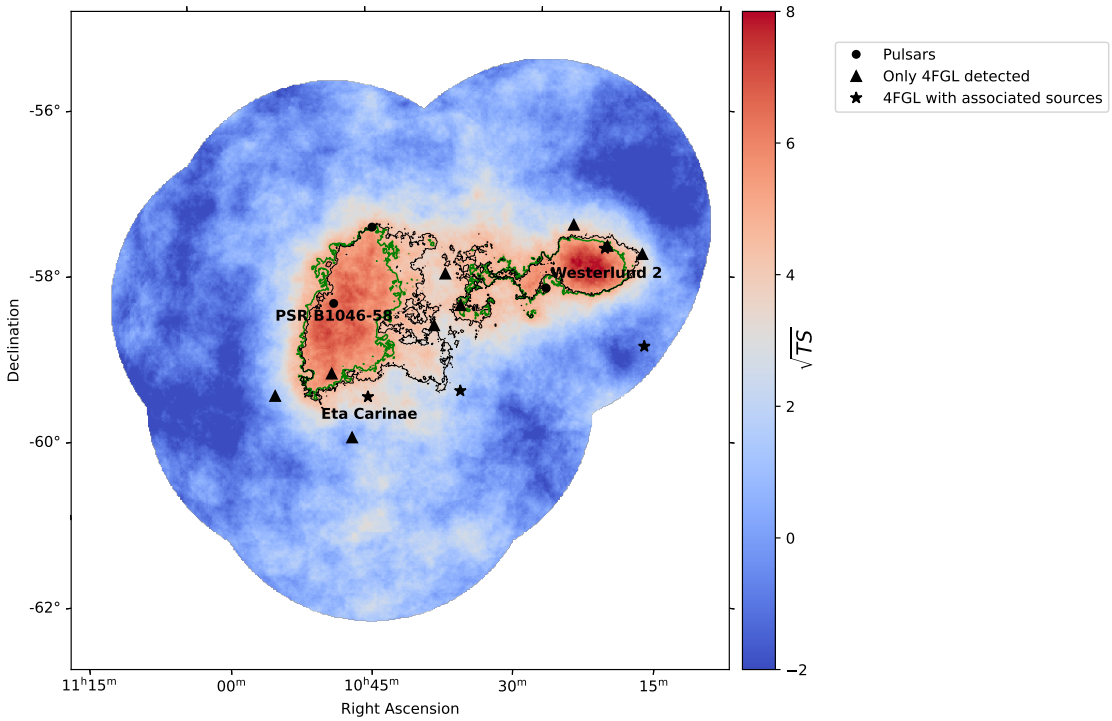

Figure 21: $\sqrt{TS}$ map after ring background reduction is applied with 5σ contours using the ring method (green) and the contours previously found with the FoV method (black); the correlation radius is 0.6°. The same sources as shown in Fig. 19 are depicted as well.

However, when regarding the $\sqrt{TS}$ distributions in Fig. 22, a slightly wider extend for the distribution with masks applied occurs. The values in Table 4 show that even though μ is at zero, the fitted σ is now above its ideal value. As the exclusion masks are the same as for the FoV background method, they should not provoke such a large value for σ all of a sudden. This is supported by fact that μ is located at zero which is the case if no γ-ray source is present outside the masks.

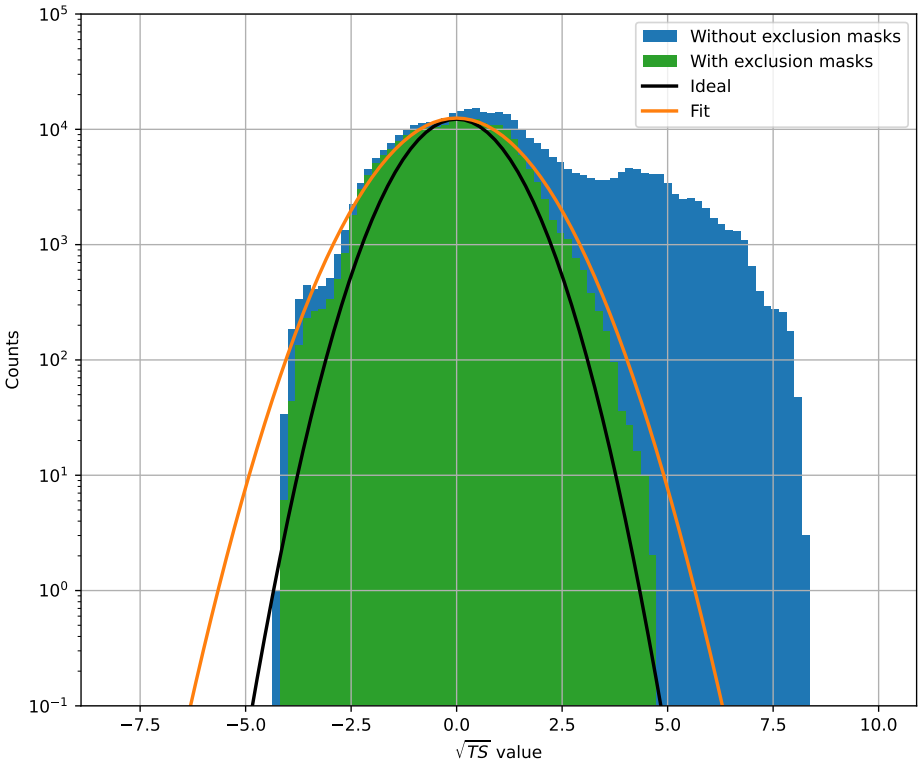

Figure 22: $\sqrt{TS}$ distribution with and without masks applied for the ring background reduction method. Additionally the fit and ideal distributions functional behaviour according to Eqn. (15) are shown.

Table 4: Fit values using Eqn. (15) on the $\sqrt{TS}$ distribution with masks in Fig. 22.

Parameter	Value	Error
A [10^3 Counts]	12.5	0.17
μ	0.00	0.02
σ	1.30	0.02

Therefore, the origin of this behaviour lies most probably in the changed background reduction method, i.e., the size of the ring used during the computation. Indeed choosing the ring to have inner radius of 1.5° with width equal to 0.5° may leads to a wrongly estimated acceptance for the region. However, using these values for the ring size have shown to be the best fitting, as choosing an inner radius smaller than 1.5° provoked more than half of the observations to fail the reduction (similar for the width). In turn, choosing a larger radius resulted in an underestimation of the background counts, resulting in single observation to have $\mathcal{O}(10^6)$ background counts, which is, given a typical observation contains ~ 900 counts in total, a ridiculous value. This phenomenon also supports the suggestions by Berge et al. (2007), which state that the FoV background reduction method is best suited for extended emission regions. However, this does not mean that the ring background reduction method is in general not suitable for extended regions, but rather an inconvenient choice, as its success

depends on the OFF region size.
Thereby, the acceptance computed by the ring method requires the ratio between the ring's solid angle and the fraction of the ON/OFF regions to be $\sim 1/7$. This implies for an ON region of radius 1.8°, an OFF region to be larger than the observed FoV, thus only achievable if more observations around the region would be made. Yet, larger OFF regions would then be affected by the non uniform nature of the acceptance across a region with a width $> 5°$, thus making them not desirable as well (Berge et al., 2007).

Run-matching background reduction

In order to have another cross-check, the run-matching approach is now applied too, using the same 5% energy threshold treatment as before. Before the actual background reduction can be done, a list of OFF runs needs to be obtained from the database using the methods described by Wach et al. (2024). However, the matching parameter range has been changed to higher limits than the ones stated in the original work. The reason to do so lies within the later following analysis for HESSIu Monogem data which requires a broader parameter range due to a lack of OFF runs fulfilling the criteria mentioned before. Therefore, this validation is not only done to confirm the extended emission detected around PSR B1046-58, but also to ensure that the changed parameters do produce a valid result. Thereby, the parameters as depicted in Table 5 are used during the search algorithm for possible matching OFF runs.

Table 5: Parameter values used to find matching OFF runs in the database for HESSI PSR B1046-58 data. Furthermore a column containing the validated parameter values by Wach et al. (2024) are depicted.

Parameter	value	validated value
Duration	0.25	0.07
NSB	0.90	0.80
Muon efficiency	0.19	0.11
transparency	0.19	0.06
trigger rate	0.45	0.25
Radiometer temperature	0.55	0.50

The algorithm usually takes one ON run at a time and compares it to all available OFF runs that are within the parameter bounds. If one such run is found, it is marked as being used and taken out of the algorithm, thus making it heavily depend on the order in which the runs are given to it. This can lead to the problem that some runs do either not find any match at all or that they find a matching OFF run that could however fit to some other ON run better. Therefore, it is decided to change the algorithm to simply find every possible match at first, leading to some ON runs have more than others[10]. However, when searching for ON-OFF pairs in the database, a careful inspection needs to be done, as some OFF runs show an unexpected behaviour. Even though some OFF runs can show a minimal fractional

[10]Some runs have shown to be more matchable than others, even though the time difference of their measurements were within a couple of hours.

run deviation, they still can have properties like for example a total counts number of ~ 0, i.e., truly empty observations. Therefore such OFF runs are taken out of the background reduction, even if they show a smaller run deviation than others. After filtering out these runs, all remaining are sorted by their smallest fractional run deviation. This leads to some OFF runs occurring several times, as shown in Table 16 in the Appendix A.1. Fig. 23 depicts the OFF run zenith angle distribution together with the ON runs for comparison reasons.

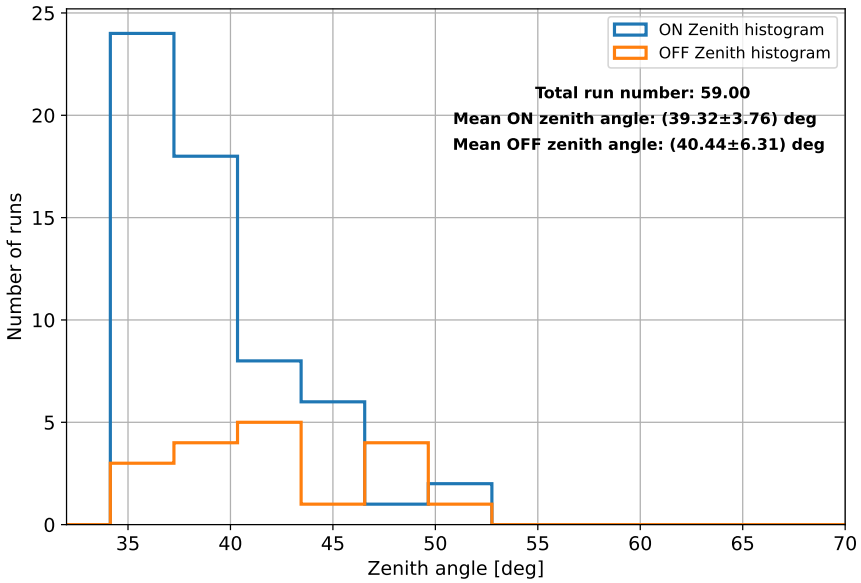

Figure 23: Zenith angles of the ON and OFF runs used during the run-matching background reduction for the region around PSR B1046-58.

It shows that no OFF runs were performed at similar zenith angles as the ON runs, as it is shown in Fig. 14. The average livetime is also in the same range as the mean ON run livetime, as all OFF runs have a livetime of ∼28 min.
Next, as shown in Fig. 24, the fractional run deviation histogram is of most interest, as it gives an estimate on how the atmospheric and instrument behaviour can be replicated by archival observations. Thereby the values show a more or less normal distributed spread between 0.2-1.8, with a mean fractional run deviation of 1.00 ± 0.32. This is acceptable, however not perfect, as a larger run deviation also means that the observational conditions differ more. Therefore potential systematics could be introduced, such as a general over-/underestimation of the background.

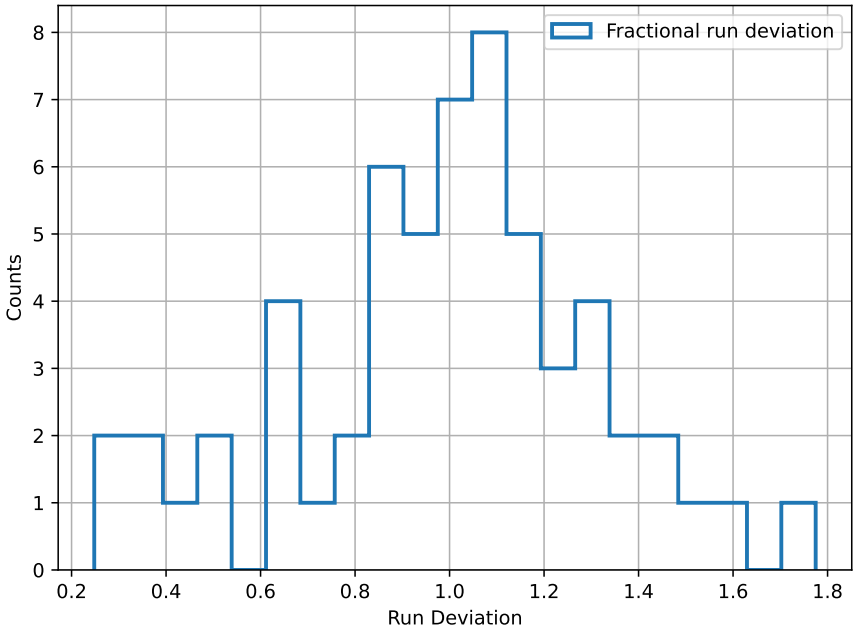

Figure 24: Fractional run deviation histogram for the ON-OFF run-matching for the data around the region of PSR B1046-58.

As the run-matching approach also uses the FoV background reduction method, albeit only on the OFF runs in this case, it is worthwhile inspecting the norm and tilt distributions. Fig. 25 & 26 shows them, revealing that most values are around zero and one. Like done previously, their fit values using Eqn. (15) are also shown with the plots. The norm is below the desired value of one, which however does reflect here the atmospheric conditions in which the OFF runs were taken. Therefore, the reason for a norm smaller than one is that the matched atmospheric conditions of the ON-OFF pair differ by a slight amount.

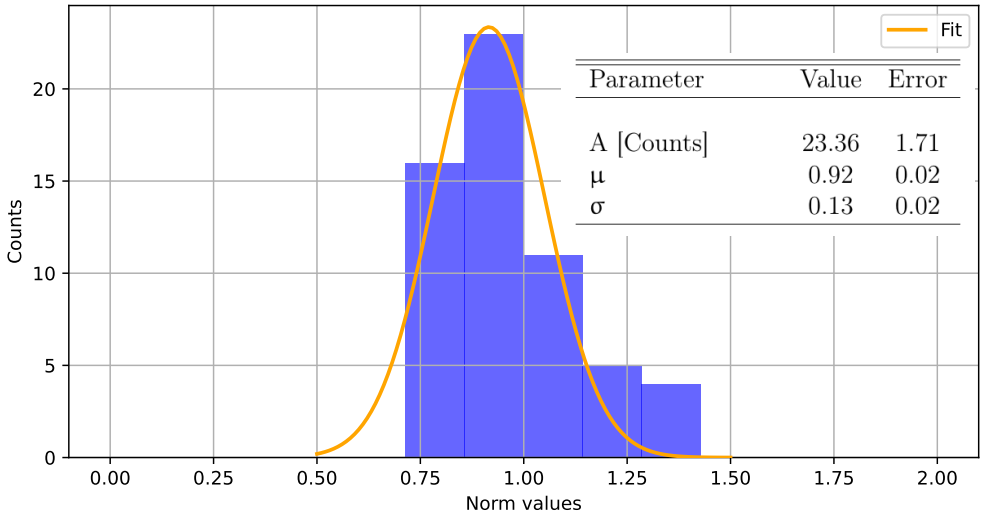

Figure 25: Norm histogram for the OFF runs alongside fit parameters using Eqn. (15).

The tilt histogram on the other hand shows a distribution around zero, which is expected.

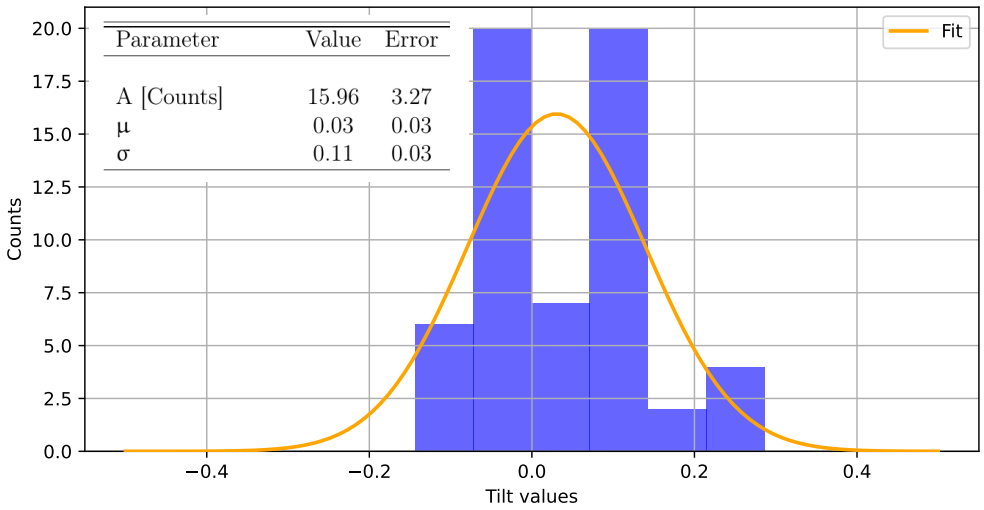

Figure 26: Tilt histogram for the OFF runs alongside fit parameters using Eqn. (15).

The resulting $\sqrt{TS}$ map with the 4FGL sources as well as contours of the FoV map is shown in Fig. 27 for a correlation radius of 0.6°.

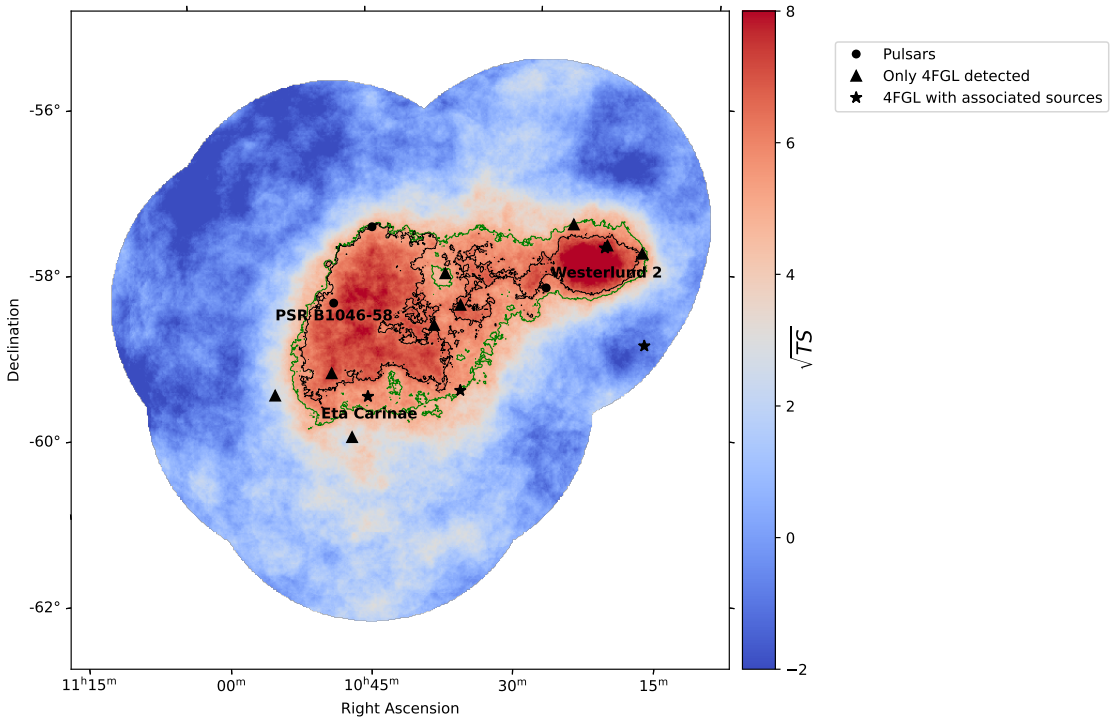

Figure 27: $\sqrt{TS}$ map with 5σ contours using the run-matching method (green) and the contours previously found with the FoV method (black); the correlation radius is 0.6°. The sources from the 4FGL catalogue indicated as before.

It can be seen that run-matched data with the used parameters to calculate the fractional run deviation seem to give a general overestimated emission from the region. However, this overestimation still occurs at reasonable values, such that the results using this method are still applicable.

3.3 Spectral analysis

From now on, only the FoV background reduction dataset (i.e., the one obtained in Fig. 19) is used for further analysis, as it represents the most realistic background reduced dataset. As could be seen throughout this section, choosing different reduction methods led to slightly different outcomes, thus making the FoV the most accurate one.
Analysing extended γ-ray emission regions is not straightforward, as they do not allow a precise morphological differentiation within them. Therefore it is decided to use a grid of squares laid upon the central emission region, as it can be seen in Fig. 28. The grid is placed upon the region, such that a single grid is always centred on the position of PSR B1046-58, i.e., square with number 3 in this case. The width of the square is chosen to be 1.075°, which represents the smallest size possible for the squares while also having the majority of emission covered. Furthermore, it turned out that using smaller squares leads to diverging model fits, being on the one hand due to sparsely populated regions (e.g., region 9), and on the other hand due to differences in the emission type (e.g., regions 1 & 2).

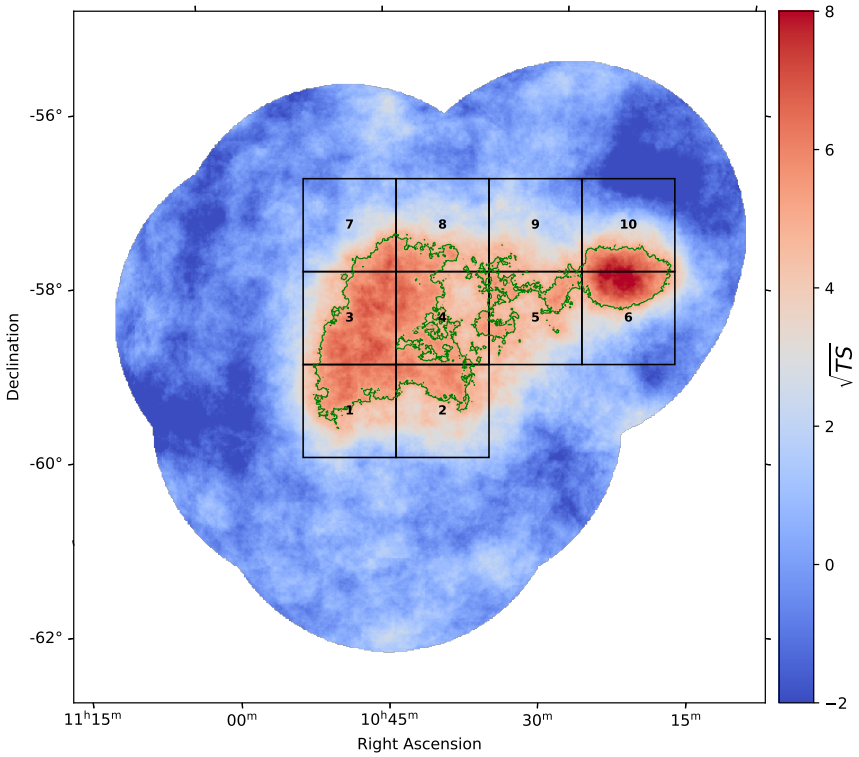

Figure 28: Grid overlay for the dataset obtained by using the FoV background reduction method. For each grid a spectral model fit using Eqns. 16 & 17 is performed where the highest significant one is kept.

The spectral models that are fitted onto each region are a simple power law

$$\phi_{\mathrm{PL}}(E) = \phi_0 \left(\frac{E}{E_0} \right)^{-\Gamma} , \tag{16}$$

and a more complex exponential cutoff power law

$$\phi_{\mathrm{EPL}}(E) = \phi_0 \left(\frac{E}{E_0} \right)^{-\Gamma} \exp(-(\lambda E)^{\alpha}). \tag{17}$$

For each region, both models are fitted and their significance is calculated. Then, only the model with the highest significance is used. In both cases the reference energy $E_0 = 1.16$ TeV is used and kept frozen during the fit process. Furthermore the parameter $\alpha = 1.0$ is also kept constant during the fit process in order to achieve converging fits. Tables 6 & 7 show the best fit results for each region together with its significance, with a heat map of the fitted indexes to be found in Fig. 29.

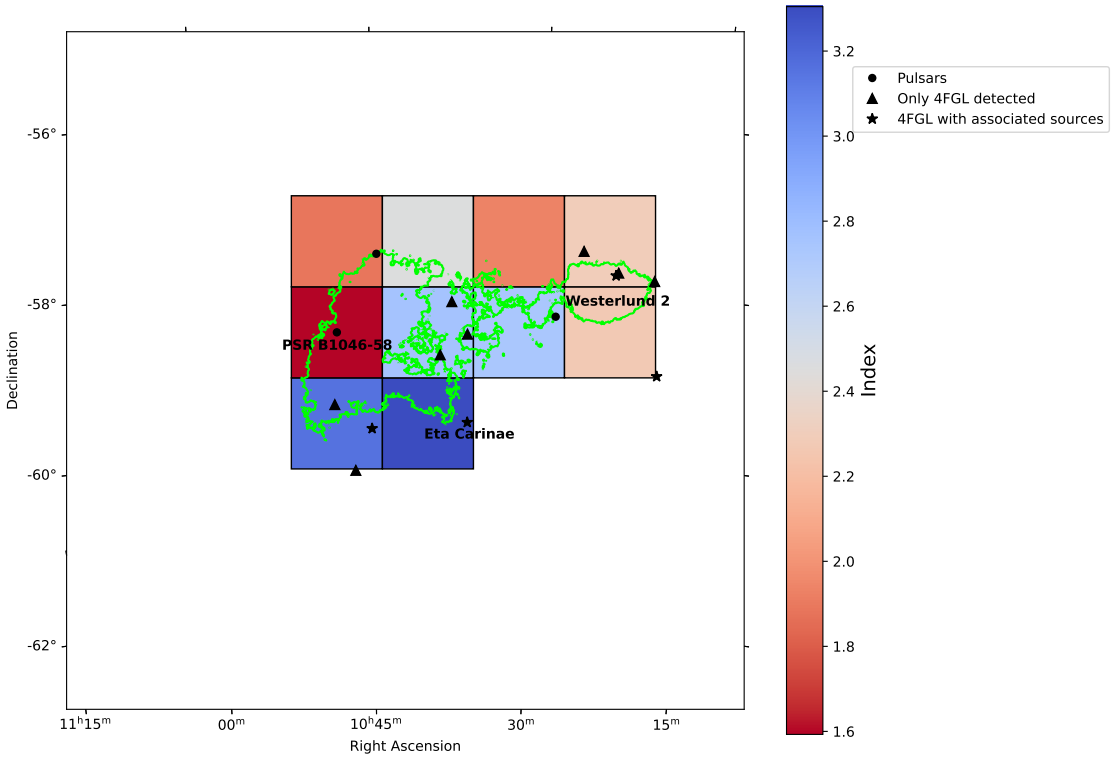

Figure 29: Heat map of the fitted index from the spectral models listed in Tables 6 & 7. Same contours and source positions as in Fig. 19 are applied. The index colourbar is normed by the value of the region centred around PSR B1046-58.

When comparing the fitted index parameters, it shows that two bottom regions (regions 1 & 2 in Table 6) share a similar index, as both have $\Gamma > 3$. Furthermore, regions 4 & 5 as well as 6 & 10 have almost even amplitudes and indexes, thus indicating that the emission is produced by the same source or sources with similar properties. The latter regions are at the

position of Westerlund 2, for which Abdalla, Abramowski, et al. (2018) found a spectral index of 2.36 ± 0.05, which is slightly larger but within errors consistent to the calculated models. However, when regarding regions 4 & 5, only 4FGL has so far detected three sources at these positions (see Fig. 19 and Table 2), these being 4FGL J1036.3-5833e, 4FGL J1037.8-5810c, and 4FGL J1038.8-5848c. The former source is thereby the only one modelled spatially by a disk with semi-major axes length of 2.465°, and therefore accounts for the entire region of interest and not just regions 4 & 5 (Abdollahi et al., 2020). This leaves only the two other sources left, both of which are modelled as point sources together with a logarithmic parabola spectral model by Abdollahi et al. (2020). However, as these sources are on the one hand both unassociated and on the other hand modelled by different models, a further comparison is omitted.
Yet, similar to these regions, region 8 shows a comparable index, however with a smaller amplitude, being less than half as large as the other two. Although being not as strong as them, this indicates that the region shows a similar emission type as regions 4 & 5. Moving on to regions 7 & 9, both of which having an index below two while also sharing the smallest amplitudes. In total, region 7-9 show the smallest model significances, which is most probably due to the emission below 5σ the take into account.

Table 6: Best fit model parameters upon the grid depicted in Fig. 28 in case Eqn.(16) provided the highest significance. As previously mentioned, the reference energy is kept at constant value $E_0 = 1.16$ TeV and is therefore not written down here.

Region	ϕ_0 [10^{-12} TeV^{-1}s^{-1}cm^{-2}]	Γ	Significance [σ]
1	2.54 ± 0.70	3.16 ± 0.47	4.42
2	2.61 ± 0.90	3.30 ± 0.83	3.92
4	2.43 ± 0.62	2.76 ± 0.27	4.72
5	2.86 ± 0.92	2.74 ± 0.38	4.26
6	1.72 ± 0.76	2.27 ± 0.26	2.77
7	0.58 ± 0.52	1.89 ± 0.35	2.29
8	1.26 ± 0.62	2.46 ± 0.33	2.11
9	0.68 ± 0.52	1.93 ± 0.32	2.32
10	1.43 ± 0.83	2.29 ± 0.36	2.37

This leaves only region 3 left, which is the only one where an exponential cutoff power law has been the highest significance model. Additionally, it is the only model exhibiting a significance of 5σ, making it the highest significance model among all fits done.

Table 7: Fit parameters in case Eqn.(17) provided the highest significance upon the grid depicted in Fig. 28. Again, the reference energy and index α are kept at constant values $E_0 = 1.16$ TeV and $\alpha = 1$, and thus not written down.

Region	ϕ_0 [10^{-12} TeV^{-1}s^{-1}cm^{-2}]	Γ	λ	Significance [σ]
3	1.43 ± 0.46	1.59 ± 0.31	0.08 ± 0.04	6.14

Furthermore, as can be seen in the heat map in Fig. 30, where the energy flux integral

$$F_e = \int_{E_1=1.16\ \text{TeV}}^{E_2=90\ \text{TeV}} dE\ E\ \phi(E) \tag{18}$$

is computed for all regions, it is also the region with largest emissivity. Yet, it can be seen that the chosen centralisation upon the position of PSR B1046-58 provokes that the emission from the Westerlund 2 region is split up between regions 9 and 10.

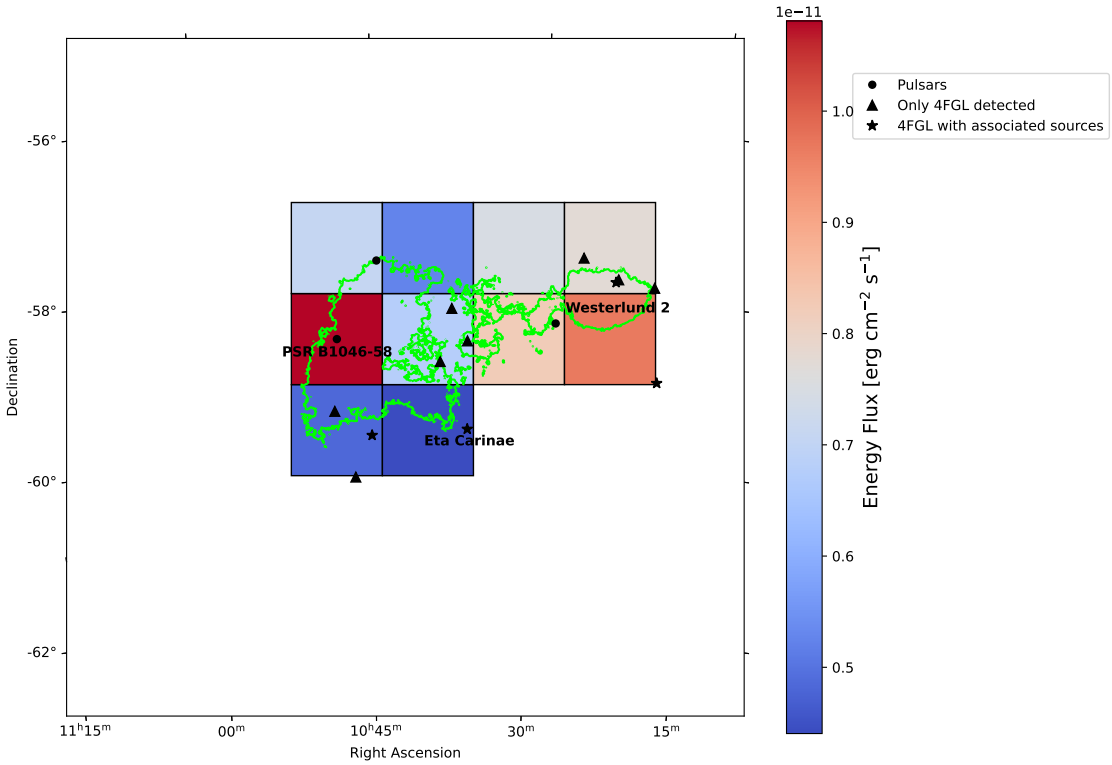

Figure 30: Heat map of the calculated model energy flux integrals according to Eqn. (18) with the 5σ contours of the FoV map (Fig. 19) as well the sources from Table 2. The energy flux integral colourbar is normed by the value of the region centred around PSR B1046-58.

However, regardless of this choice, the energy flux integral from region 3 indicates that the strongest emission comes from within that region. This is in contrast to what is found by Yang et al. (2018) using Fermi LAT data, which contribute Westerlund 2 as the main source of emission present within the FoV. Furthermore, they attribute the extended emission to be following an $1/r$ emission for increasing distances r from Westerlund 2. This is inconsistent to the shown distribution in Fig. 30, indicating that there is a second major source within the FoV. This inconsistency can also be seen in Fig. 31, where the 3, 4, 5 $\sqrt{TS}$ levels from the paper by Yang et al. (2018) are plotted into the map, which were kindly made accessible for this thesis. Thereby, it seems that their reported emission is of a different shape from what is observed using HESSI data, therefore suggesting a shift between the data.

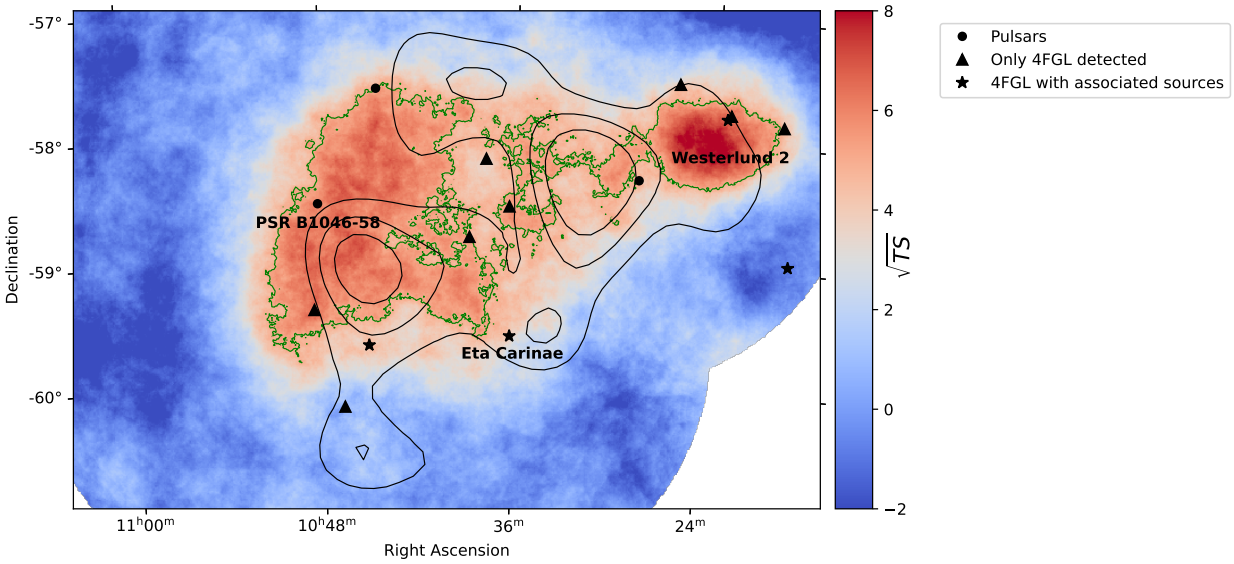

Figure 31: $\sqrt{TS}$ map with overlaid 3, 4, and 5 $\sqrt{TS}$ levels from the paper by Yang et al. (2018), which utilized Fermi LAT data. The contours by Yang et al. (2018) were thereby obtained for energies energies above 10 GeV. Furthermore all sources from the 4FGL catalogue listed in Table 2 taken from Abdollahi et al. (2020) are also plotted.

Thereby it seems that the major centres for emission (5 $\sqrt{TS}$ levels) account for the region between PSR B1046-58 and Eta Carinae, as well as the "between" region and Westerlund 2 alike. This could mean that the emission measured by Yang et al. (2018) is attributed to multiple sources and thus could explain their explanation of the $1/r$ decrease.

3.3.1 Flux point extraction

Having now modelled the regions, flux points are estimated using the `FluxPointsEstimator` class provided by `Gammapy`. Furthermore following discussions by Bevington et al. (2003),

the reduced χ^2_{red} is imposed as

$$\chi^2_{\text{red}} = \frac{\chi^2}{\text{d.o.f.}} = \sum_{i=1}^{n} \frac{(y_i - m_i)^2}{\sigma_i^2}. \tag{19}$$

Hereby, y_i denotes the calculated flux point, and σ_i^2 its error, whereas m_i is the reference flux computed from the model. In this case, $\chi^2/\text{d.o.f.} = 0.99$ for the $E^2\text{d}N/\text{d}E$ fluxes, thus indicating that the estimated flux points are within a valid range. The values of the estimation are listed in Table 8, together with their corresponding energy. The $E^2\text{d}N/\text{d}E$ flux points vs. energy can be seen in Fig. 32 together with the residuals.

Table 8: Estimated $E^{2dN}/_{dE}$ together with its corresponding energy. Note that the energy bands are given here, thereby making E_{min} and E_{max} the bandwidth of the energy in which the flux can be found and not the error of the energy.

E_{ref} [TeV]	E_{min} [TeV]	E_{max} [TeV]	$E^2\frac{dN}{dE}$ [10^{-12} erg cm^{-2} s^{-1}]	$\Delta E^2\frac{dN}{dE}$ [10^{-12} erg cm^{-2} s^{-1}]
1.66	1.16	2.36	2.85	1.06
3.77	2.36	6.02	3.75	0.95
8.55	6.02	12.2	4.53	1.24
16.3	12.2	21.8	1.82	1.29

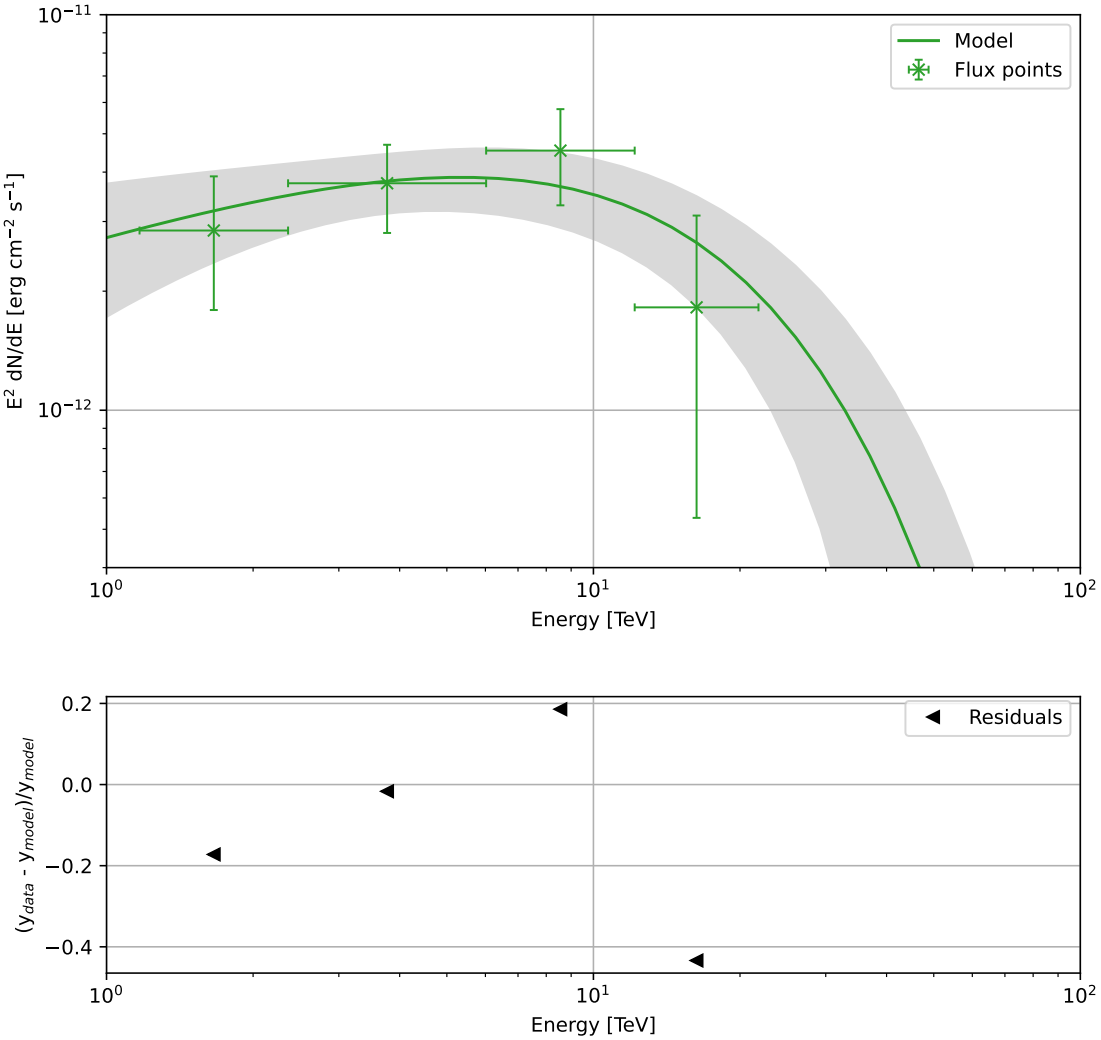

Figure 32: $E^{2}{}^{dN}/_{dE}$ over energy together with the reference model (top panel) and the corresponding residuals (bottom panel). Note that the energy bands are given here, thereby making E_{min} and E_{max} the bandwidth of the energy in which the flux can be found and not the error of the energy.

Since the $\chi^2/_{\text{d.o.f.}}$ is almost equal to 1, the estimated flux points can be assumed to be well computed from the reference model. Furthermore, the residuals in Fig. 32 indicate that the distance between model and estimated flux is not larger than 0.2 in between 1.16-12.15 TeV. However, for energies above 12.15 TeV, the estimator seems to produce a larger error for the found flux point. This is also visible in the residual plot, as the estimated flux point shows a residual below -0.4, showing clearly that the model is slightly worse in this energy range. However, as the estimation of this flux point is also within errors acceptable with the model, it can be further used, making up in total four energy flux points available for further analysis.

3.4 Broad-band source modelling

In order to analyse the source further, flux points are extracted from several other telescopes that have observed PSR B1046-58 in different energy regimes. Thereby, one must take into account that the following analysis takes a wide range of energies into account, ranging from sub-eV up to TeV regimes. It is important to notice that observing astrophysical sources at different energies also means that their emission character is not the same either. For example, a TeV halo can hardly be observed by a measurement in the lowest radio regime, whereas the TeV emission could be shifted from the true pulsar position. Here, a similar situation occurs for the observed data in other energy regimes, as most collaborations only report an emission from the PWN's hosting pulsar B1046-56. However, as previously discussed in section 1.4, the emission character of a post supernova system shows a different type across the measurable wavelengths. Therefore, by including these observations, different aspects of the region can be taken into account, with radio to X-ray emissions revealing the photon emission around the pulsar itself. The observed TeV emission can then be used to explain the emission type due to older emitted cosmic rays (electrons and positrons) from the region. Thereby, the inclusion and analysis of multi-wavelength data can give vital access to the mechanisms responsible for the observed emission.

3.4.1 Flux points between radio and sub-TeV range

However, before models can be fitted on the flux points extracted from different telescopes, some minor unit conversions and a derivation of the flux points from model parameters given by the collaborations need to be done. The computation of flux points further used in such cases is demonstrated through theoretical calculations in Appendix A.2. Basically this is necessary for data taken by the space observatories Chandra/XMM-Newton, used by Gonzalez et al. (2006) and the **A**dvanced **S**atellite for **C**osmology and **A**strophysics (ASCA) data, used by Pivovaroff et al. (2000), which both observed PSR B1046-58 in the keV regime. Table 9 shows all values necessary during the computation (energy band, energy flux, index) that are taken from said papers and its results (amplitude, flux point) computed by own means. Note however that the errors derived from the sources are just the upper and lower error bounds inserted into the calculation. Therefore the errors on the flux points calculated are just the upper and lower bound and not some propagated error. In order to then calculate $E^{2dN}/_{dE}$, the mean value of E_1 and E_2 is used.

Table 9: Calculated $E^{2dN}/_{dE}$ flux points using data obtained by Chandra/XMM-Newton observatories (Gonzalez et al., 2006), as well as from ASCA (Pivovaroff et al., 2000). In order to calculate $E^{2dN}/_{dE}$, the mean of E_1 and E_2 is used as reference energy.

E_1 [keV]	E_2 [keV]	F_e [10^{-13} erg cm^{-2} s^{-1}]	α	A [10^{-5} keV^{-1} cm^{-2} s^{-1}]	$E^2 \frac{dN}{dE}$ [10^{-14} erg cm^{-2} s^{-1}]
0.50	10.0	$1.00^{+0.70}_{-0.20}$	$1.70^{+0.40}_{-0.20}$	$1.59^{+1.11}_{-0.30}$	$4.19^{+3.66}_{-4.66}$
2.00	10.0	$2.50^{+0.30}_{-0.30}$	2.00	$9.67^{+0.19}_{-0.19}$	$1.55^{+0.19}_{-0.19}$

Furthermore the data taken in the MeV-GeV band is from the 4FGL source catalogue (Abdollahi et al., 2020) as well as the third **E**nergetic **G**amma **R**ay **E**xperiment **T**elescope (EGRET) catalogue (Hartman et al., 1999), and the second **A**strorivelatore **G**amma ad **I**mmagini **LE**ggero (AGILE) catalogue (Pittori, C. et al., 2009). The corresponding table in which the flux points and energies are listed is Table 10. The data obtained from the third EGRET catalogue thereby had several fluxes listed for a single energy, hence the reason the error is in this case stated as the standard deviation. Furthermore, only flux points that have shown $\sqrt{TS} > 5$ are thereby used from the third EGRET catalogue.

Table 10: $E^{2dN}/_{dE}$ flux points taken from the 4FGL catalogue (Abdollahi et al., 2020), third EGRET catalogue (Hartman et al., 1999), and the second AGILE catalogue (Pittori, C. et al., 2009). The flag "1" means that the error were stated as such, whereas "2" means that the error is computed from the standard deviation of given values.

E_{ref} [GeV]	E_{min} [GeV]	E_{max} [GeV]	$E^{2dN}/_{dE}$ [10^{-11} erg cm^{-2} s^{-1}]	Flag
0.17	0.10	0.30	$2.71^{+0.66}_{-0.64}$	1
0.55	0.30	1.00	$5.04^{+0.13}_{-0.13}$	1
1.73	1.00	3.00	$4.99^{+0.08}_{-0.08}$	1
5.48	3.00	10.0	$2.48^{+0.06}_{-0.06}$	1
17.3	10.0	30.0	$0.47^{+0.05}_{-0.05}$	1
54.8	30.0	100	$0.03^{+0.03}_{-0.02}$	1
400	-	-	$10.31^{+0.85}_{-0.85}$	2
0.65	0.30	1.00	$3.18^{+0.61}_{-0.61}$	1
2.00	1.00	3.00	$13.46^{+4.17}_{-4.17}$	1

Data taken in the radio energy band is from the ATNF pulsar catalogue (Manchester et al., 2005; ATNF Catalogue, 2025c), and the upgraded **M**olonglo **O**bservatory **S**ynthesis Radio **T**elescope (UTMOST) pulsar timing programme I (Jankowski et al., 2018) and visible in Table 11.

Table 11: $E^{2dN}/_{dE}$ flux points taken from ATNF pulsar catalogue (Manchester et al., 2005; ATNF Catalogue, 2025c) and UTMOST pulsar timing programme I (Jankowski et al., 2018). The errors are stated as such in the individual papers.

Energy [μeV]	$E^{2dN}/_{dE}$ [10^{-16} erg cm^{-2} s^{-1}]
2.90	$0.84^{+0.07}_{-0.07}$
3.31	$1.08^{+0.08}_{-0.08}$
5.79	$1.27^{+0.07}_{-0.07}$
12.4	$1.86^{+0.15}_{-0.15}$
3.49	$1.14^{+0.08}_{-0.08}$

3.4.2 Physical Modelling

The derived flux points are now used to fit a spectral energy distribution calculated by taking particle processes into account. As already mentioned, the C++/python library `GAMERA` (Hahn, Romoli, et al., 2022) is used to model the particle interactions surrounding PSR B1046-58. In principle, the software package aims to solve the particle transport equation that describes the energy distribution function $N = N(E,t)$ (Atoyan et al., 1999)

$$\frac{\partial N}{\partial t} = Q(E,t)\frac{\partial}{\partial E}(PN) - \frac{N}{\tau_{\text{esc}}}, \tag{20}$$

where $Q(E,t)$ is the injection spectrum, $P = P(E,t) = \frac{\partial E}{\partial t}$ is the energy loss rate, and $\tau_{\text{esc}} = \tau_{\text{esc}}(E,t)$ is the characteristic escape time. However, as the analytical solution[11] of this equation is only possible in case P and τ_{esc} are time constant, numerical approaches are required. Therefore the usage of Markov chain Monte Carlo (MCMC) simulations is necessary and hereby executed using `emcee`[12] developed by Foreman-Mackey et al. (2013). A more thorough discussion of this approach can be found in MacKay (2003).
Thereby, the spectrum that describes the particle injection into the system is chosen to be a simple power law of the form

$$Q(E) = \frac{A}{\tilde{N}} \cdot \psi(E) = \frac{A}{\tilde{N}} \left(\frac{E}{E_{\text{ref}}}\right)^{-\alpha}, \quad \text{where} \quad \tilde{N} = \int_{E_{\text{min}}}^{E_{\text{max}}} dE\, E\psi(E). \tag{21}$$

[11] First found by Syrovatskii (1959) using Green's function.
[12] `https://emcee.readthedocs.io/en/stable/`

For the fit of the particle injection spectrum, the parameters A, α, and β are kept free, while $E_{\mathrm{ref}} = 1$ TeV ≈ 1.6022 erg. Using this spectrum as injection source for the electrons in the system allows to fit models describing the particle processes as described in section 1.2 to the data. In this case synchrotron and IC scattering contributions to the emission are taken into account, therefore requiring photon target fields for the latter one. Thereby, a thermal target photon field is used in order to calculate contributions due to IC scattering of CMB photons. Since this field follows a blackbody spectrum, one can express the energy density in terms of the temperature through Stefan-Boltzmann's law (Bartelmann et al., 2018)

$$w_{\mathrm{CMB}} = aT^4 \,, \quad \text{with} \quad a = \frac{4\sigma}{c} = \frac{8\pi^5 k_b}{15h^3c^4}. \tag{22}$$

Therefore, when using $T_{\mathrm{CMB}} = (2.72548 \pm 0.00057)\,\mathrm{K}$, one obtains an energy density of $(0.26039 \pm 0.00006)\,\mathrm{eV\,cm^{-3}}$ when plugging the temperature into Eqn. (22) for the CMB photon target field (Fixsen, 2009). The second field is derived using methods described by (Popescu et al., 2017a; Popescu et al., 2017b) and accounts for ultraviolet submillimeter radiation fields of the Milky Way. In order to account for the synchrotron component, a magnetic field B is required and is thereby fitted upon the data too.
As the flux points shown in Tables 9-11 were specifically computed for the pulsar and not its PWN, two fits are applied in this case. The first one is done for the synchrotron emission using the data in 9-11, where and a second one using the derived data in this work for the IC scattered emission. In both cases a MCMC sampled fit chain is started using 30 walkers with 2500 burn-in-steps and 10000 subsequent steps. Additionally, the fits are only used further, if all walkers have a so-called acceptance fraction within 0.2 to 0.5, as this factor indicates the number of accepted steps that are within priors. Thereby having an acceptance close to zero indicates a too wide step size for the walkers during the sampling, whereas a value closer to one indicates a too tiny step size (Foreman-Mackey et al., 2013).
Furthermore, in order to validate that the obtained MCMC sample has converged well, the so-called Gelman-Rubin coefficients are computed, which are now briefly introduced, following discussions by Vats et al. (2021).

Gelman-Rubin coefficient $\hat{R}$ (Vats et al., 2021):

Given there are m chains (walkers) in a MCMC simulation that runs n steps after an initial burn-in period, where X_{iq} $(1 \leq i \leq m,\, 1 \leq q \leq n)$ independent Markov chains are sampled. Then one can calculate the average of m sampled variances s^2 via

$$s^2 = \frac{1}{m}\sum_{i=1}^{m} s_i^2 \quad \text{with} \quad s_i^2 = \frac{1}{n-1}\sum_{q=1}^{n}(X_{iq} - \bar{X}_i)^2 \tag{23}$$

where $\bar{X}_i$ represents the sample mean from chain i and s_i^2 being the variance of each chain. Given then that across all chains one obtains a global mean $\hat{\mu} = \frac{1}{m}\sum_{i=1}^{m}\bar{X}_i$, one can define the sample variance of sample means as

$$B = \frac{n}{m-1}\sum_{i=1}^{m}(\bar{X}_i - \hat{\mu})^2. \tag{24}$$

Then, the Gelman-Rubin coefficient is given as

$$\hat{R} = \sqrt{\frac{\sigma^2}{s^2}}\,, \quad \text{with} \quad \sigma^2 = \frac{n-1}{n}s^2 + \frac{B}{n}, \tag{25}$$

thus comparing the variance between the chains σ^2 to the one within the chains s^2. A MCMC fit has thereby converged, if these parameters are close to each other (i.e., if $\hat{R} \approx 1$), as this indicates a well mix between global variance and variance within the chains. Thereby, all MCMC fits that are made here are only further used, if $\hat{R} < 1.01$.

Concluding these considerations, the first fit applied here is for the synchrotron component of the obtained data, i.e., data in Tables 9-11. Thereby, the injection spectrum described in Eqn. (21) is fitted alongside the B-field responsible for the observed synchrotron emission. The corner plots of the MCMC fit can be seen in Fig. 33, where a logarithmic parametrisation is used for the amplitude and B-field of the model. It shows that the sampling has effectively found a best fitting sample, as all distributions show a Gaussian shape. The only correlation that seems to be occurring is thereby happening for the amplitude and B-field, as their corner plot shows a slightly elongated shape. This however is expected, since changes of the amplitude during the sampling directly impact the strength of the magnetic field used for the radiation component. Thereby, both parameters basically provoke similar changes for the calculated spectral energy distribution (SED) and are therefore correlated to each other.
In order to obtain the best sampled values, the median (blue lines in Fig. 33) of the distribution is used as the final fitted parameter. The errors are calculated from the 16^{th} and 84^{th} percentile of the distribution (black dotted lines in Fig. 33), i.e., the 1σ range.

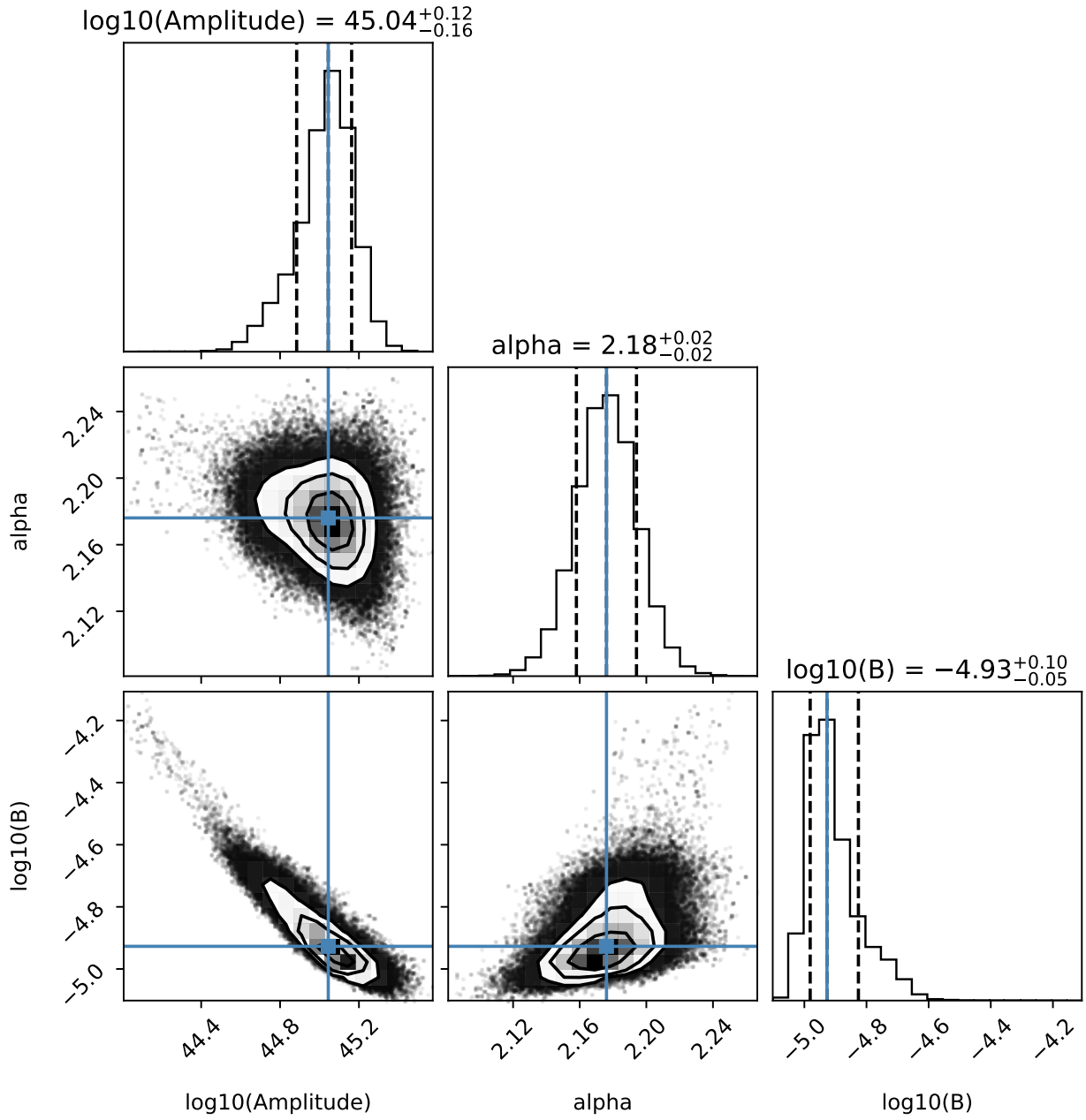

Figure 33: Corner plots of the MCMC using 2500 burn-in steps followed by 10000 sampling steps afterwards for the synchrotron model. The best fitting values used for the computation are obtained from the median value (blue line) of the Gaussian distribution. Furthermore, the errors are computed from the 1σ range of parameters around the median.

Since the MCMC parameters shown here are in logarithmic depiction, a more cleared visualisation of the obtained fit values are shown in Table 12 alongside the priors used during the sampling.

Table 12: MCMC fit parameters obtained for the synchrotron SED fit.

Parameter	$\log_{10}$(value)	value	prior
Amplitude	$45.04^{+0.12}_{-0.16}$	$1.10^{+0.35}_{-0.34} \cdot 10^{45}$ erg^{-1}	$44 < \log_{10}(A) < 50$
α	-	$2.18^{+0.02}_{-0.02}$	$1.5 < \alpha < 3$
B-field	$-4.93^{+0.10}_{-0.05}$	$11.75^{+3.05}_{-1.28}$ µG	$-6 \leq \log_{10}(B) \leq -4$

Thereby, the injection spectrum shows an amplitude of $A = 1.10^{+0.35}_{-0.34} \cdot 10^{45}$ erg^{-1} and index $\alpha = 2.18^{+0.02}_{-0.02}$, which means that the flux of electrons/positrons decreases with increasing energy, as is expected. Furthermore, the strength of the magnetic field is estimated to be $11.75^{+3.05}_{-1.28}$ µG, which is a typical value encountered within the ISM, as it is estimated to have field strengths ~ 10 µG (Beck, 1983). In conclusion to theses values, the estimated injection spectrum fits the surrounding region of the pulsar well, since the injection of electrons/positrons follows a direct way through the power law. Furthermore the obtained magnetic field strength fits to the expected values for the interstellar magnetic field strengths thus indicating a realistic description of the magnetic field.
The other MCMC sampling is done for the flux points in Table 8, where the main contributing emission is due to IC scattered photons of the radiation fields discussed earlier. Due to the lack of data points, only the injection spectrum could now be modelled on the data, leading to the corner plots depicted in Fig. 34, with the recalculated values presented in Table 13.

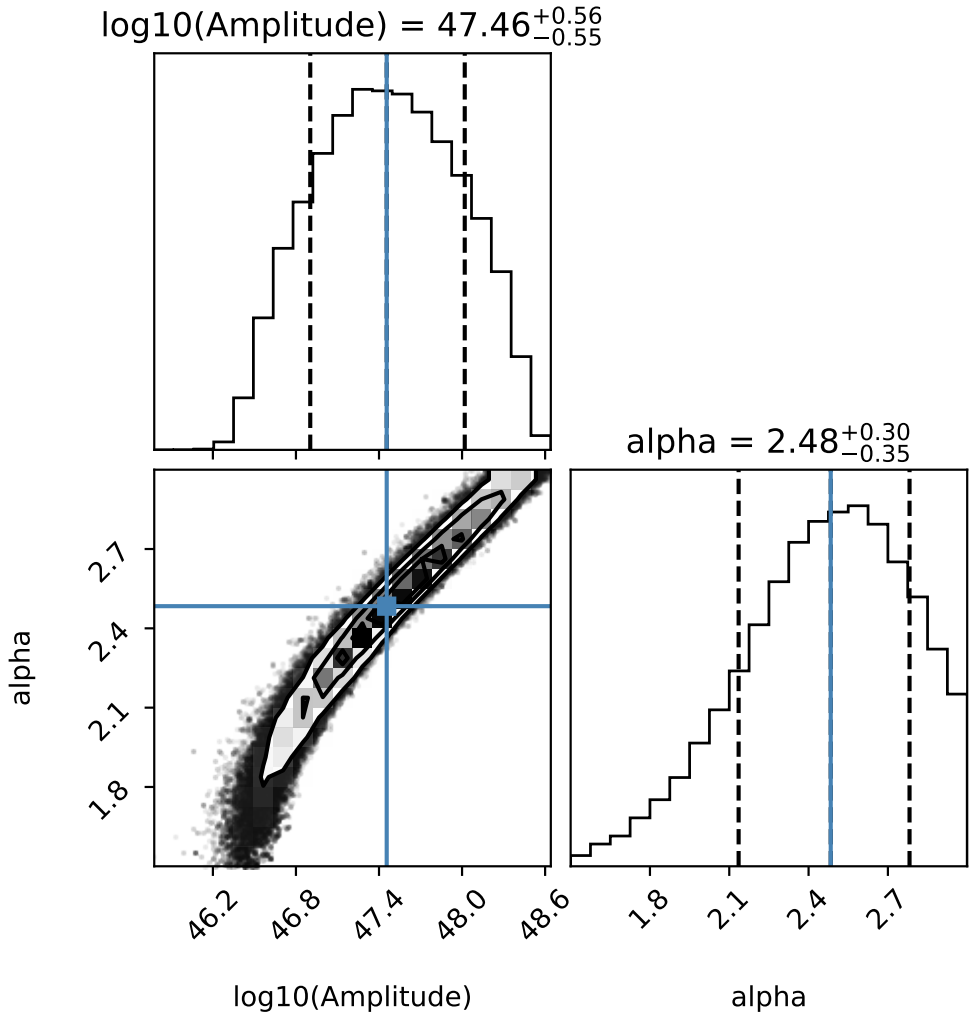

Figure 34: Corner plots of the MCMC using 2500 burn-in steps followed by 10000 sampling steps afterwards for the IC model. The lines are applied like described in Fig. 33.

The corner plots of the two parameters show Gaussian distributions, albeit having in this case a larger correlation between the parameters. This however can be expected in this case, since both these parameters are essentially only plugged into the injection spectrum without any other parameter to be constraining them. Thereby, the calculated best fitting model only depends on variations given by the amplitude and index of the power law, which of course influence each other. Furthermore, the sampling depends on the data points that are available for fitting, i.e., the four flux points in the TeV domain. Thereby any model that is used to parametrise the emission must have four or less parameters, since an application of a model with more parameters than fit points does not make sense. Thereby, the limited fit must be carried out in this case with only the injection model and no other physical quantity, which itself limits the conclusions that can be drawn from the model to those that are assumed in the model. This means that hereby only IC scattering from CMB and submillimeter radiation photon fields is attributed, leaving possible contributions from pion decay or Bremsstrahlung up to debate. Nevertheless, using only the IC fit without other contributing effects to the

TeV emission is still valid, since it is anyway estimated that the main emission of γ-rays is due to this effect (Giacinti et al., 2020).

Table 13: MCMC fit parameters obtained for the IC SED fit.

Parameter	$\log_{10}$(value)	value	prior
Amplitude	$47.46^{+0.56}_{-0.55}$	$2.88^{+7.59}_{-2.08} \cdot 10^{47}$ erg^{-1}	$44 < \log_{10}(A) < 50$
α	-	$2.48^{+0.30}_{-0.35}$	$1.5 < \alpha < 3$

The resulting MCMC sampled fits for the synchrotron and IC components can then be seen in Fig. 35 which shows the broad-band SED of all obtained flux points.

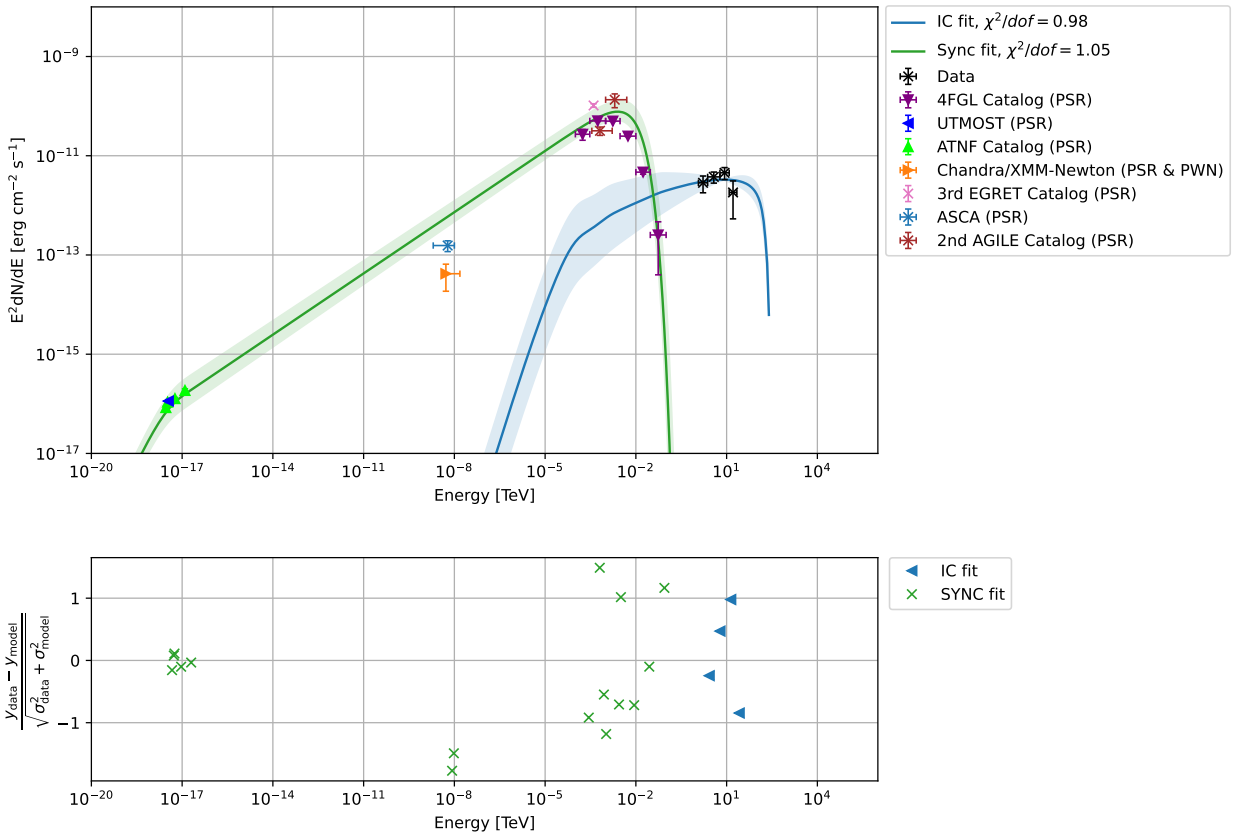

Figure 35: Obtained broad-band flux points alongside best fitting synchrotron and IC models as well as their residuals. Note that the residuals take also the error of the MCMC sampling into account.

In this case, the calculation of the χ^2 value must now be modified, since the obtained MCMC fit itself represents a best fitting sample that can be prone to errors. Therefore, the model itself has an error, since the best fitting parameter is obtained from the median of the distributions in Fig. 33 & 34. Following considerations by Cowan (2019), this leads to the implementation of

$$\chi^2 = \sum_{i=1}^{n} \frac{(y_i - m_i)^2}{\sigma^2_{\text{total},i}}, \quad \text{with} \quad \sigma_{\text{total},i} = \sqrt{\sigma^2_{y_i,i} + \sigma^2_{m_i,i}} \tag{26}$$

where the error of the model $\sigma_{m_i,i}$ is calculated from the upper and lower bounds m_i^{upper} m_i^{lower} of the model via

$$\sigma_{m_i,i} = \frac{m_i^{\text{upper}} - m_i^{\text{lower}}}{2}. \tag{27}$$

Therefore, the obtained model must rather be seen as a relatively well fitting model instead of an absolute (true) one. This is mainly due to the limited information that is available over the total spectrum depicted here. Thereby, ~ 20 decades need to be taken into account when fitting the synchrotron component. This makes the model a good compromise between the different obtained fluxes rather than an actual best fitting model for the data. Therefore, taking the model errors into account is the best way to account for this systematic shift towards a global description of the spectrum rather than an individual best fitting model.
A similar case occurs for the IC model, this time however, the fit is limited by the scarce data that could be obtained so far in the TeV domain. One could argue that using the last or even second to last 4FGL flux points could be worthwhile during the fit, since the model error margin is also within the vicinity of these two fluxes. However, since the 4FGL data is obtained only for the PSR this would not be advisable. Furthermore, observations in the TeV domain above 30 TeV limit the estimation of a reasonable energy cutoff (E_{max} for the IC component), which is thereby estimated to be ten times the last energy bin of the obtained data in this work. Therefore, the model is also prone to sampling errors and the extrapolated regions must be accordingly adjusted by error marges.
Taking these model errors into account leads to reasonable reduced χ^2 values around one, indicating that including the model errors is necessary in this case. Furthermore, when regarding the residuals in the plot below the SED in Fig. 35, it shows that the best fits occurred for the radio data. The rest of the synchrotron spectrum is then aligned more or less within reasonable margins around zero, albeit showing for the X-ray data an overall overestimation and some underestimation for data in the sub-TeV domain. However, given the overall accordance of the model and its limited precision due to the numerical MCMC approach as well as the scarce data in the between radio to sub-TeV data, it is concluded that the model fits reasonably.

3.5 Discussion

Starting off by the reported emission within the region by Jardin-Blicq (2019), an analysis of the region surrounding PSR B1046-58 was carried out. Thereby, it was necessary to apply several cuts to the data due to periastron runs as well as contaminated runs due to high NSB values. Furthermore, only runs above a livetime of 25 min were considered for the analysis, leading to further reduction in observations. However, it could be argued that the periastron runs did not need to be discarded in the first place, since suggestions by Steinmassl et al. (2023) concluded no major impacts of the periastron passage. Yet, since only four observations were taken during that time, the decision to discard them for the analysis seemed to be a reasonable choice in this case. The remaining 59 observations that could be further used were then taken to the next analysis step, the background reduction.
Three background reduction methods were applied, these being the FoV, ring, and ON-OFF run-matching. In order to account for the high NSB contamination among the remaining runs, two different energy thresholds derived from the energy bias and effective area IRFs were applied. Thereby, only the larger one was utilised further during the background reduction for every observation. Starting off with the FoV method, an exclusion mask of 1.8° radius is used, together with other masks for known and proposed sources. This then led to norm and tilt values that are in accordance to expectable values of zero and one. However, before a sky map could be obtained, the resulting energy bias of the dataset was further analysed, leading to the application of a 5% bias window for the dataset due to reasons of consistency. Thereby, only data in between 1.16-90 TeV was further taken into account, resulting in a sky map as seen in Fig. 19, which showed an emission in roughly the same size as reported by Jardin-Blicq (2019). Furthermore, it could also be seen in the $\sqrt{TS}$ distribution that no emission due to a remaining source persists, as the distribution with applied masks followed a uniform Gaussian. Concerning the other background reductions, the same masked regions and bias methods as for the FoV background reduction were applied to the ring background method, resulting this time in a reduced region of γ-ray emission. Furthermore, the $\sqrt{TS}$ distribution revealed a value of 1.30 ± 0.02 for the σ of the Gaussian fit upon the distribution. This large value most probably emerged due to the poor choice of the ring radius and width, which, given the limited size for OFF regions available, represent a reasonable compromise. Thereby, the ring method did not fit perfectly for the region, but could still be used as a reasonable comparison to the obtained sky map using the FoV method. At last, the ON-OFF matching following Wach et al. (2024) was applied, using thereby larger parameters than suggested, as the later application for PSR B0656+14 required them too. Thereby, OFF runs with similar zenith angles and livetime as the ON runs could be obtained, albeit implementing multiple usage of OFF runs in this instance. The fractional run deviation between the runs was also within reasonable boundaries with only a small number of pairs exhibiting deviations larger than 1.5. Applying then the FoV background method upon the OFF runs led to reasonable norm and tilt distributions, although the former showed a mean value below the desired value of one. This behaviour however is expectable, since a changed norm implies that the atmospheric conditions of the ON-OFF pair differed in that case, leading to a changed norm. The 5% bias window was then applied upon the dataset, leading to a sky map which showed a broader emission than the FoV map. The reason for this extended emission type to occur lied most probably within the relaxed parameters used for the matching, which however led to a reasonable result.

In conclusion to the three applied background reductions, it was decided to only use the FoV background map, since it can be seen as the moderate mean between the ring and ON-OFF map. It could be argued that using the ring map is also viable, since it showed a more conservative emission throughout the region, which is in addition also more centred around PSR B1046-58. This however is not advisable, since the ring used for the background reduction was actually too small, since the required ratio between ring solid angle and fraction of the ON-OFF region is not $\sim 1/7$ (Berge et al., 2007). Thereby, a larger ring (i.e. OFF region) would have been required, which would then need more measurements to be carried out further away from the source. However, given that such observations do not exist, the ring method remains to be only viable as a sort of verification of emission to present within region rather than an actual option for further analysis steps. Additionally, the use of the ON-OFF map is also not advisable, since the derived sky map showed brighter emission than the FoV map. This in itself is not a problem, but rather represents a choice towards the more conservative emission type obtained by using the FoV method.
Concluding the background estimation, a grid of 10 squares was lain upon the the derived FoV sky map and spectral models were fitted upon the dataset. Thereby, each grid had a size of ($1.075^\circ \times 1.075^\circ$), which corresponds to a physical size of $\sim$54 pc for each grid, given the estimated distance of 2.9 kpc to the source. This resulted in the region centred around PSR B1046-58 to have the highest significant model. The best fitting spectral model was found to be being an exponential cutoff one for the region around PSR B1046-58. The other regions had a simple power law as the best fitting one. Taking then the index and energy flux maps (Fig. 29 & 30) into account revealed that the main emission is centred around PSR B1046-58. The reason to get to this conclusion is that the spectral index of the model is 1.43 ± 0.46 and thereby suggesting a more compact region of γ-ray emission, which is in contrast to e.g., regions 1 & 2 that had indexes > 3. However, it must be kept in mind that the application of the grid results in the Westerlund 2 region to be split up into basically two parts. Thereby, both the squares that are upon Westerlund 2 showed similar indexes but a smaller energy flux for the top region. Furthermore, it shows that the regions in between PSR B1046-58 and Westerlund 2 (regions 4 & 5) have spectral indexes ~ 2.7. Therefore, it can be concluded that the emission is of extended type with no clear source being responsible for the emission there. Concerning region 7, an index of 1.89 ± 0.35 leads to the suggestion that the source of γ-ray emission is within the square present. Since only PSR J1044-5737 lies within its vicinity and no other source being present, this emission is most probably due to this pulsar. However, since the square also takes large portions of emission below 2σ into account, this result must be treated with care, thus requiring more thorough studies of the region.
In total, it can be concluded that the region centred around the position of PSR B1046-58 is the one with the most concentrated and strongest emission within the region, albeit taking also minor emission below 3σ into account. This is in contrast to the results by Yang et al. (2018) using Fermi LAT data, which suggests that the emission follows a $1/r$ shape, where Westerlund 2 is the main source of emissivity. Comparing also the 3,4, and 5 $\sqrt{TS}$ contours above 10 GeV as done in Fig. 31 then revealed a shift between the reported GeV and here derived TeV emission. Thereby, it could be that the reported emission by Yang et al. (2018) is attributed to multiple sources, which could diminish the observed emission.
In order to further investigate the emission around PSR B1046-58, flux points were extracted, leading to a total number of four that can be obtained with $\chi^2_{\text{red}} = 0.99$. The derived flux points as well as flux points derived from other reported catalogues/telescopes of PSR

B1046-58 in the radio to sub-TeV were then used to obtain radiation SEDs. Thereby, a MCMC sampled fit was carried out using these flux points, leading to a reasonable fit of a synchrotron component in between the radio to sub-TeV domain as well as an IC component for the flux points derived in this work. Thereby, the incorporation of the model error based on its upper and lower bounds was necessary, as the model provided a poor estimation otherwise. Therefore one could argue that the obtained models are biased towards the model errors chosen for the calculation. However, since not incorporating them would essentially mean that the obtained model is not inducing any systematic deviations, which it yet does. This could be best seen for the X-ray data points where the model clearly overestimates the data. Thereby, including the systematic error provides a better overall estimation, which however then comes at the cost of a systematic bias from the model estimation. Therefore, the estimation of the models can be seen as reasonable but also influenced by systematics of the models chosen hereby. Furthermore, only IC scattering was taken into account, therefore leaving contribution from pion decay as well as Bremsstrahlung up to debate. Therefore, possible contributions due to these processes must not be ruled out and therefore further studies taking them into account could lead to contributions not taken into account in this work. Nevertheless, the conclusion that the main emission observed around PSR B1046-58 is due to synchrotron and IC scattering can still be drawn, which is in accordance to discussions by Giacinti et al. (2020), which state these as the most probable sources of emission. Additionally, since the computation of the IC SED is majorly based on the flux derived in this work, it could also be that the estimated flux points take more than the contribution due to the region influenced by PSR B1046-58 into account. Since the squares of the grid that is used to describe the region provoked sizes of $\sim$54 pc for each square, it could be that parts of the emission taken into account were stemming from other sources. This in turn could provoke an artificially enlarged flux point overestimation that could then also be responsible for an overestimated IC contribution. Furthermore, since no analysis using HESSI data below 1.16 TeV was possible due to the large NSB values during the measurements, a vital link between the 4FGL and hereby derived flux points is missing. Taking all these aspects into account leads to the conclusion that the reported emission tends towards a PWN being responsible for the emission, as the SED could be described reasonably well by synchrotron and IC scattered emission. The PWN emission origin is also supported by the fact that Gonzalez et al. (2006) reported a PWN in the size of 6"$\times$11" (0.08 pc$\times$0.14 pc at distance of 2.7 kpc) in the X-ray domain to be present. Following then discussions by Giacinti et al. (2020), which state several sources with their corresponding radio and TeV PWN sizes to show a larger size for the former, a similar case occurs in this case. Yet, the size difference in this case is larger than their ratio of $R_{\mathrm{TeV}}/R_{\mathrm{X\text{-}ray}} \approx 5$ between the TeV and X-ray radius size of the PWN. Therefore the region size used here seems to be larger than for already reported radii within the X-ray and TeV domain. However, choosing smaller regions leads to poorer model estimations and was therefore not applied, thus leading to a still open question whether or not the entire region is responsible for the emission or not. Further studies need to be made to confirm or reject these results, which however then will be facing the same problems of extended emission as it was for this work. Furthermore, it could then be proven by taking more measurements in the TeV domain, whether or not the resulting IC model fits. Taking all these aspects into account leads to the final conclusion that an origin of the TeV emission is possibly due to a PWN, albeit still needing further observations within the TeV domain to safely confirm this result.

4 Analysis of the extended PSR B0656+14 region

Abeysekara et al. (2017) first reported a $\sim 2^\circ$ extended TeV γ-ray emission region to be present around PSR B0656+14, with its corresponding supernova to be the cause of the Monogem ring. Furthermore Linden et al. (2017) concluded then that the extended emission that is present around PSR B0656+14 is due to its TeV halo. Table 14 thereby shows the basic parameters of PSR B0656+14. However, the pulsar is in this case of less interest, since the main emission in the γ-ray regime is estimated to be from its TeV halo. Therefore, a data analysis is made in order to investigate the properties of the TeV halo surrounding PSR B0656+14.

Table 14: Basic parameters of PSR B0656+14 taken from the ATNF pulsar catalogue (Manchester et al., 2005; ATNF Catalogue, 2025b).

Parameter	Value	Unit
Spin period (P)	385	ms
Period derivative ($\dot{P}$)	$5.49 \cdot 10^{-14}$	ss^{-1}
Characteristic age (τ_c)	111	kyr
Surface magnetic field (B)	$4.65 \cdot 10^{12}$	G
Spin-down luminosity ($\dot{E}$)	$3.8 \cdot 10^{34}$	erg s^{-1}
R.A. (J2000)	06:59:48.20	hh:mm:ss.s
Dec (J2000)	+14:14:19.40	dd:mm:ss.s
Distance (d)	286	pc

HESSI era data are available, but only to such an sparse extend that an analysis is not practicable here. Due to these circumstances and the knowledge that there are sufficient observations done using HESSIu, an attempt to produce data by own means was done. However, this did not go to full satisfaction, as it turned out that an incorrectly estimated energy dispersion during the production of the DL3 data made further spectral analysis inadvisable. Yet, it is still possible to discuss the general spatial morphology of the region and thus provide possible insights or extensions of already known aspects of the region.

4.1 Dataset cuts

In case of HESSIu data, no observations containing NSB values above 200 could be found, thus starting off with initially 66 observations. However, out of these initial ones, two observations need to be taken out, since their livetime was below 20 min. The corresponding histogram of the remaining 64 runs can be seen in Fig. 36, showing that in total 30.10 h of data is available, with a mean duration of (28.22±1.65) min.

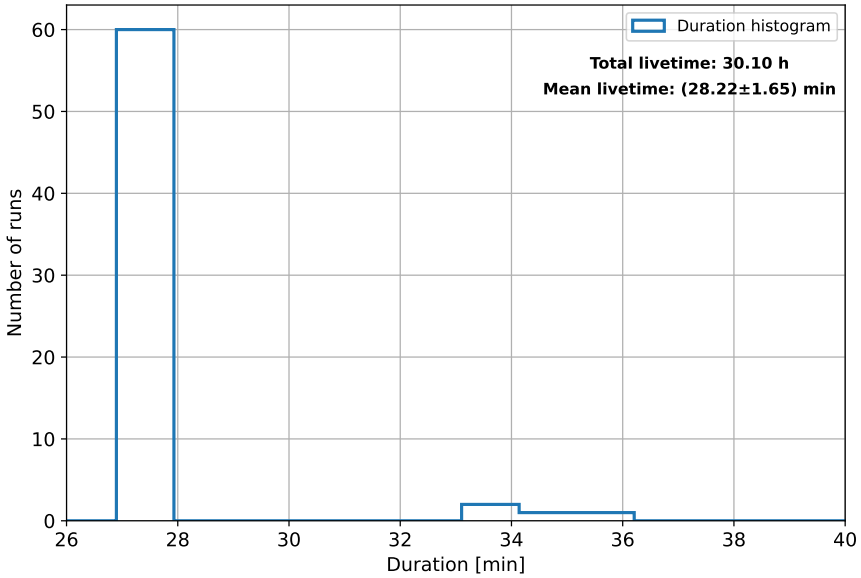

Figure 36: Livetime histogram of the available Monogem observations.

The next cut criteria is the zenith angle, which however must not be applied in this case, as all remaining runs show a zenith angle $< 60°$. This can be seen in Fig. 37, showing that the zenith angles lie around the mean $(43.30 \pm 4.18)°$.

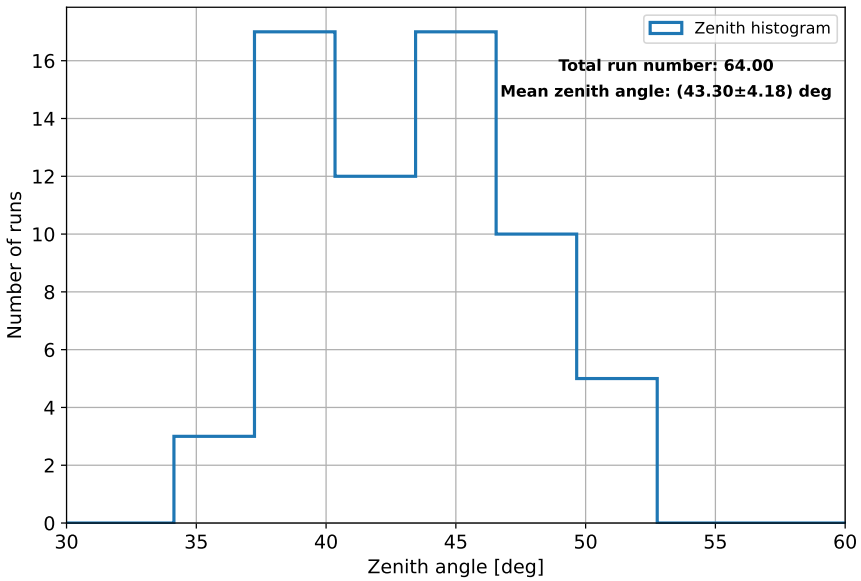

Figure 37: Zenith angle histogram of the available Monogem observations.

Having thus no further cuts that would potentially be needed, the next step lies within the background reduction of the DL3 data.

4.2 Background reduction

Since the Monogem region shows very extended emission, it is decided to only compare the FoV and run-matching approach in this analysis step. However, as will be seen at the end of this section, a systematic bias error has occurred during the background reduction, which is due to the wrongly produced DL3 data product. Therefore, this section is the main part of the analysis of Monogem HESSIu data, which however can still be used for two reasons. One being a demonstration that the run-matching is indeed the better choice than the "regular" FoV approach when it comes to really extended γ-ray emission, and second that the resulting maps can still be discussed quantitatively.

4.2.1 FoV background reduction

Contrary to the PSR B1046-58 data, the Monogem one does not need to be further restricted to certain energy ranges, since the DL3 is not affected by high NSB values. Therefore, the background reduction can be applied directly, using the exclusion masks shown in Fig. 38, where all sources within a 5° radius are excluded, and the centre mask is set upon the reported halo emission at (R.A., Dec = 07h 00m 28.8s, +14d 19' 12") and has a 2° radius (Abeysekara et al., 2017). The FoV size is in this case (8°×8°) with a bin size of 0.01°.

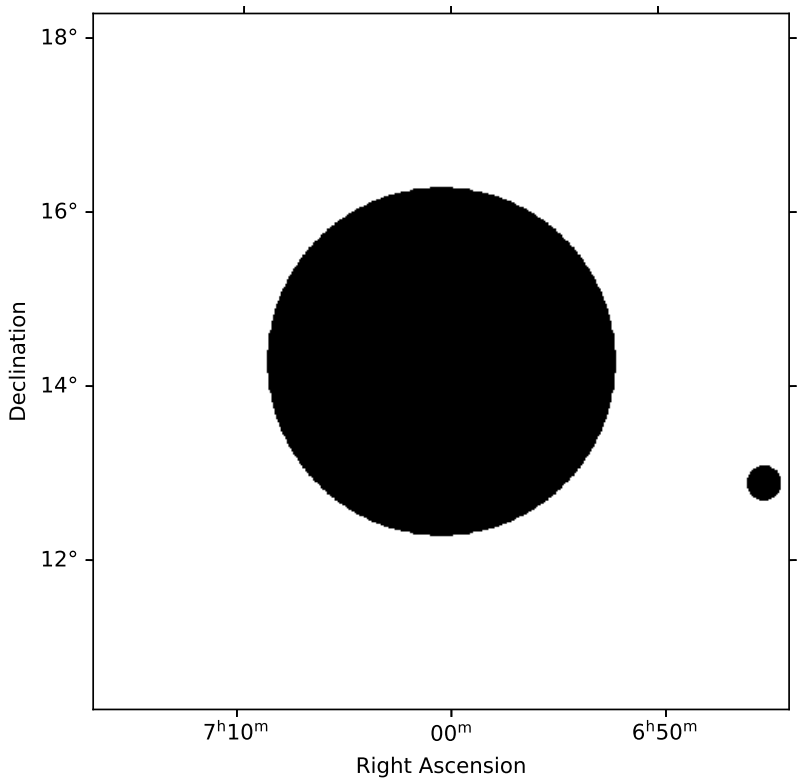

Figure 38: Exclusion masks set during the FoV background reduction applied on Monogem data.

Using these masks, a norm and tilt for the background model could be estimated to be around the expected values of one and zero, as it can be seen in Fig. 39 & 40.

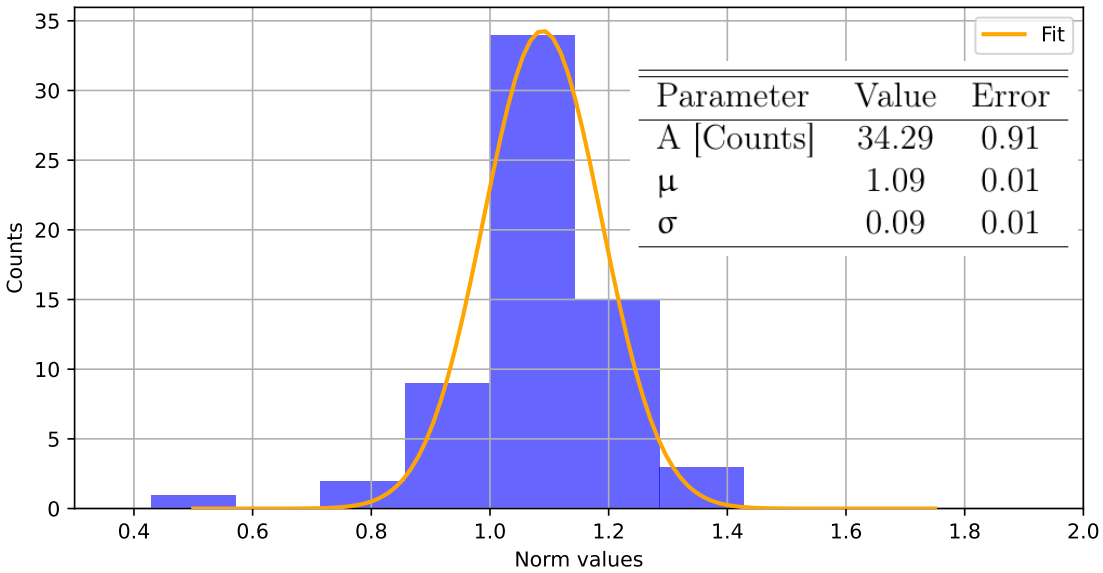

Figure 39: Norm histogram with fit parameters when using Eqn. (15).

In the norm histogram are two observations that have a very low value at 0.6 and one with a very high value at 1.3. This indicates that there is a discrepancy when the archival template is folded upon the observation. However, since such deviations can occur and will not majorly shape the outcome of the reduction, no further steps are made to exclude these datasets.

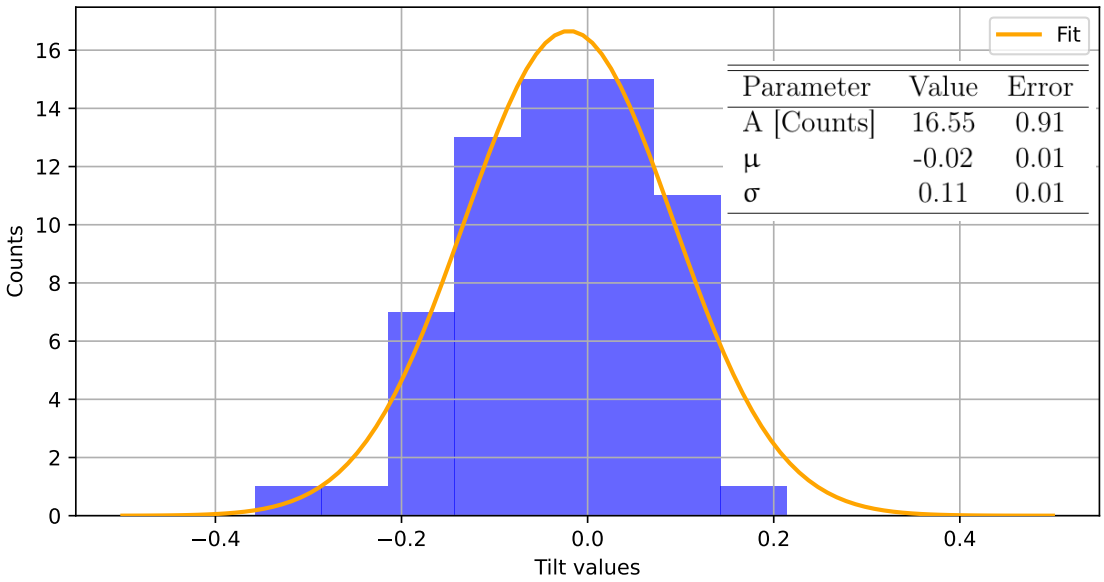

Figure 40: Tilt histogram with fit parameters when using Eqn. (15).

Additionally, the tilt values show a well distributed behaviour around zero, albeit indicating a small trend towards values below zero. This behaviour however is within errors acceptable, and therefore making the background reduction successful, at least when regarding the norm and tilt.
The resulting $\sqrt{TS}$ map in Fig. 41 shows the 2σ contours (green lines), as well as the position of PSR B0656+14 plotted in (black dot), using the coordinates from Table 14. It can be seen that when using the FoV background method, a contamination of γ-rays outside the masks is most likely, thus provoking the total range of $\sqrt{TS}$ values to lie in between ± 3.5.

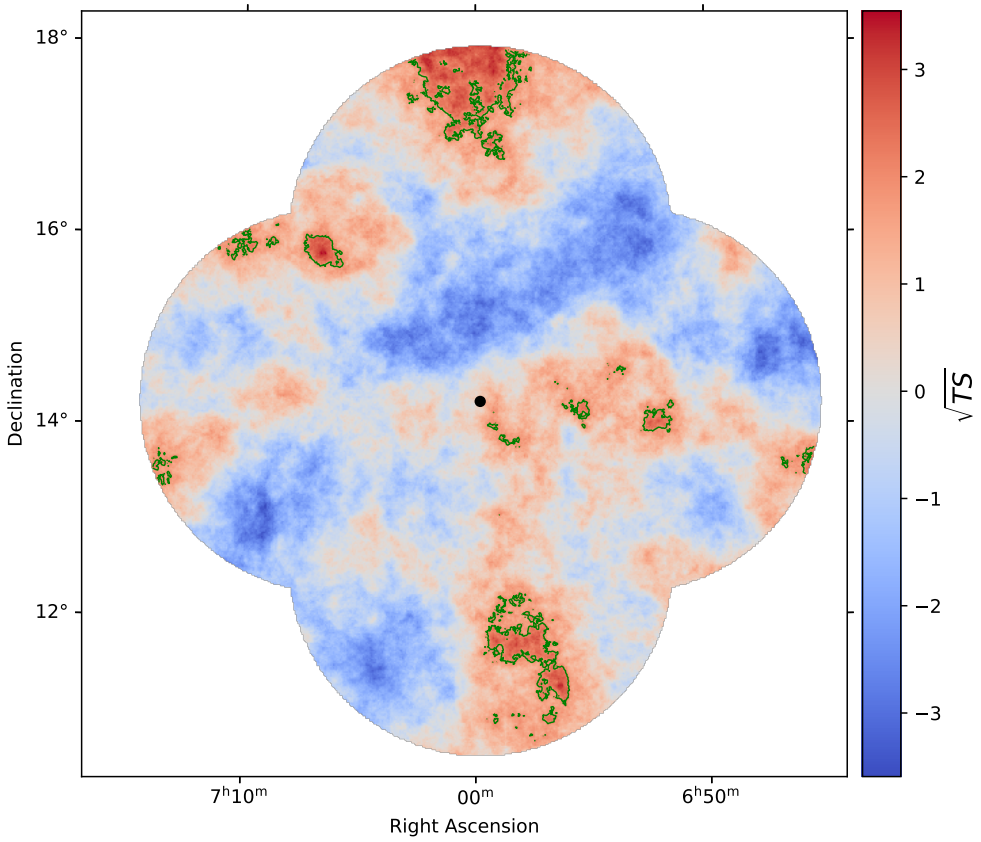

Figure 41: $\sqrt{TS}$ after the FoV background reduction of Monogem observations; the used correlation radius is 0.6°.

This effect can be seen more clearly when regarding Fig. 42, which shows the $\sqrt{TS}$ distribution with and without exclusion masks taken into account. It is evident that both distributions are almost identical, which indicates that the background was overestimated.

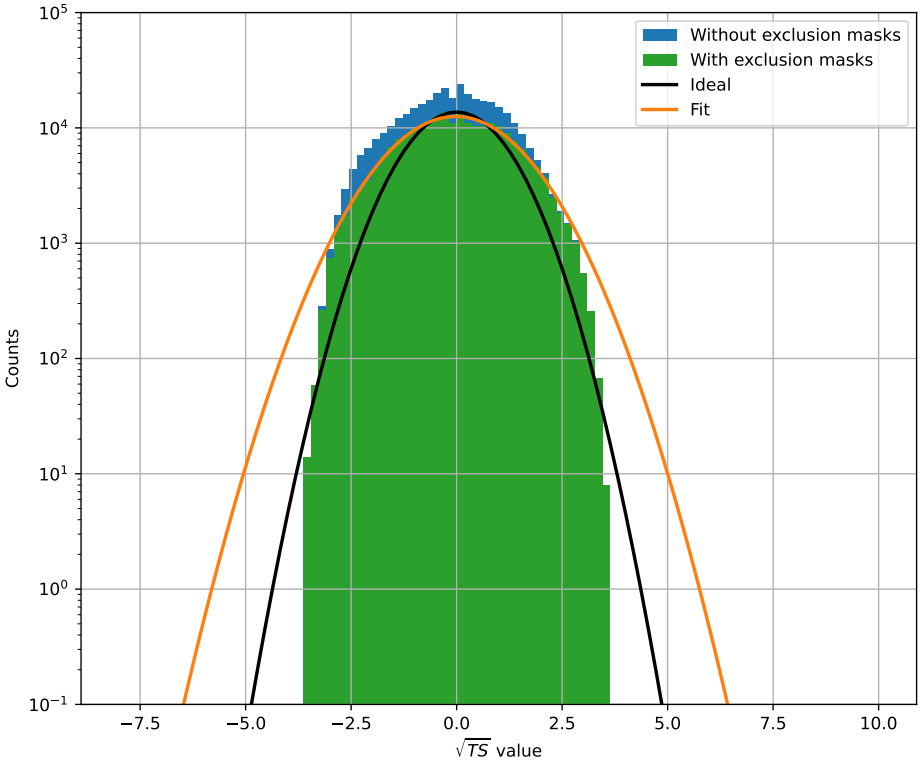

Figure 42: $\sqrt{TS}$ distribution for FoV background reduction (0.6° correlation radius) of Monogem data with and without exclusion masks, as well as its ideal and fitted (Table) behaviour using Eqn. (15).

Table 15: Fit parameters for the $\sqrt{TS}$ distribution with masks applied in Fig. 42 when using Eqn. (15).

Parameter	Value	Error
A [10^3 Counts]	12.57	0.13
μ	-0.02	0.02
σ	1.33	0.02

It seems that the emission at the edges of the FoV is responsible for this behaviour, which is expectable, since Abeysekara et al. (2017) reported extended emission to be occurring from this region. Therefore, choosing a background reduction method that normalises a template on this FoV must take this emission into account, thus leading to an overestimation of the background. This can also be observed in the fitted σ value upon the posterior distribution, which is larger than one, while having μ close to zero. The latter value thereby indicates that the FoV normalisation took all emission into account, since having μ further away from zero indicates non accounted emission. The larger value for σ and the visible equality of both distributions on the other hand leads to the conclusion that the applied masks seemingly

did not change the background reduction process. However, choosing a larger mask will not impact the result of this behaviour due to the extended emission that is present within the region, thus making the FoV background reduction a not practicable approach in this case.

4.2.2 ON-OFF run-matching background reduction

Having seen that the FoV approach results in an overestimation of the background due to the extended nature of the source makes the ON-OFF run-matching the only promising approach in this case[13]. Therefore, a run-matching using the same parameters as in Table 5 is made, resulting in only 55 ON runs to have a fitting OFF run. The matching ON-OFF observation IDs are depicted in Table 17 in Appendix B, where multiples are allowed for the pairs. However, not all ON runs could be matched to an OFF run in the database even with the relaxed parameters chosen here. The resulting fractional run deviation histogram can be seen in Fig. 43, where most values are distributed around the mean value of 1.25±0.35.

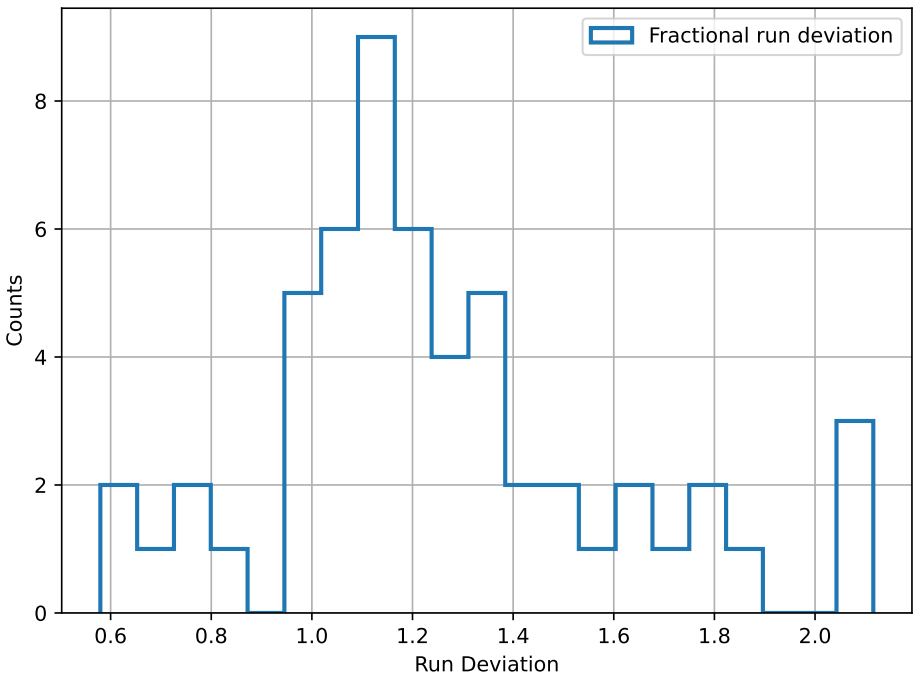

Figure 43: Fractional run deviation for the ON-OFF run-matching of Monogem observations.

Yet, some runs are showing a deviation above two, which is due to the relaxed parameters for the run-matching. Fig. 44 shows that the zenith angles of both ON and OFF runs, as well as their mean zenith angles, where less OFF runs are occurring since multiple matches are allowed. The zenith angles of both histograms lie within the same range, showing values between 34-53°, which is within well defined ranges below 60° (Abdalla, Abramowski, et al., 2018).

[13]Besides of course a classical ON-OFF region analysis as explained by Berge et al. (2007).

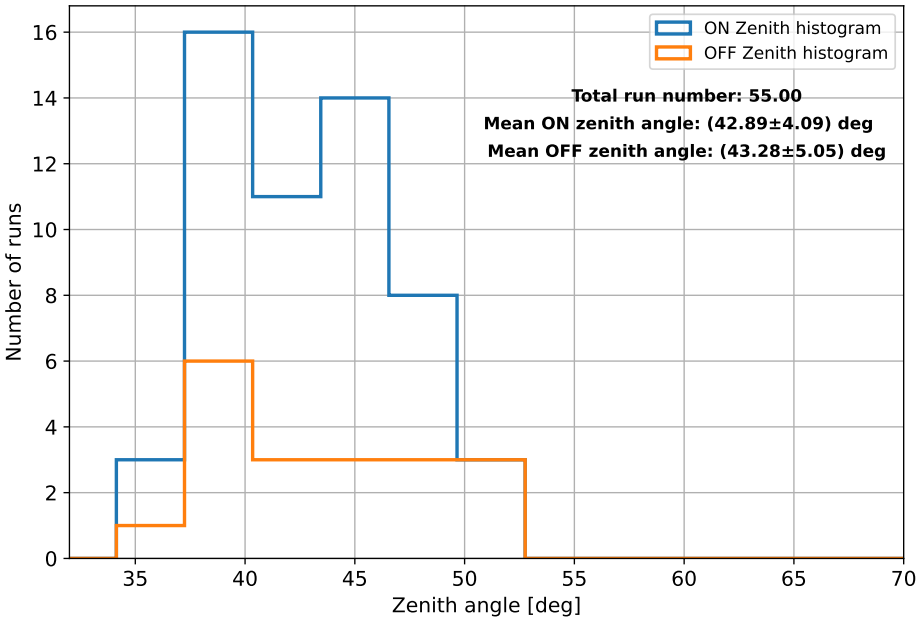

Figure 44: ON & OFF run zenith angle histograms.

The mean zenith angle of the reduced ON run list is a little bit smaller than the one depicted in Fig. 37, but within the same range. Concerning the matched OFF runs, an almost equal mean zenith angle compared to its paired ON runs can be found. However, for the livetimes, a slightly different picture arises, since the OFF runs show values between 21-30 min, which is due to the less constrained parameters during the matching.

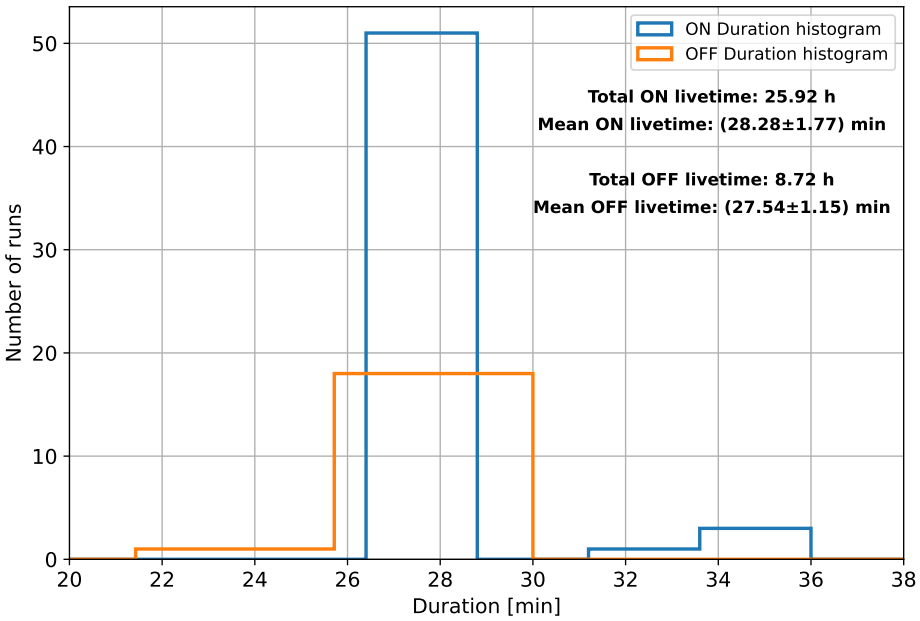

Figure 45: ON & OFF run livetime histograms.

Thereby, it seems that the parameter constrains for the run-matching lead to the inclusion of runs below 25 min, which however does not lead to an exclusion of the runs, since they are still comparable to the ON livetimes. Since the run-matching can then be estimated to be producing reasonable ON-OFF pairs, a further analysis is performed. Performing the background reduction results in the norm and tilt histograms depicted in Fig. 46 & 47, where also the fit parameters when using Eqn. (15) are shown. The tilt values are located narrowly around zero, with no outliers to be seen, thus indicating a well behaviour.

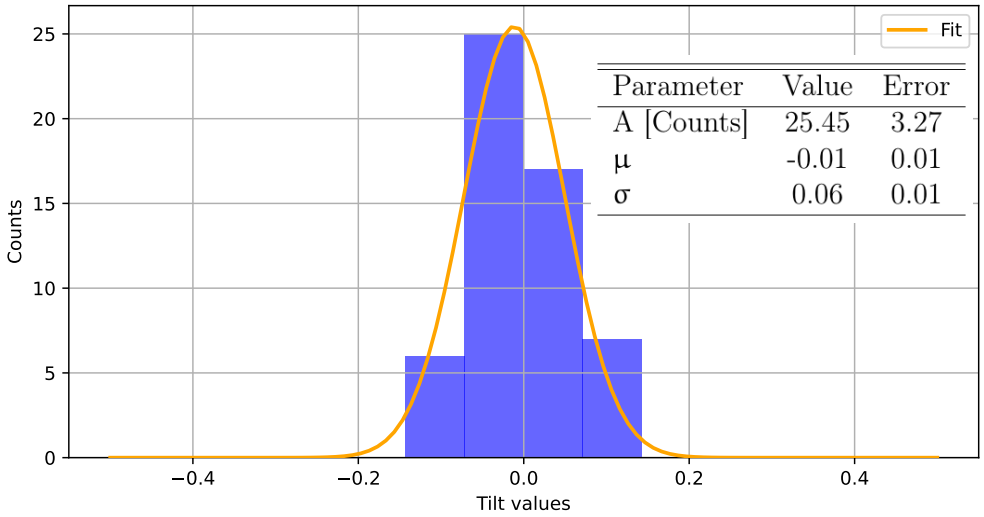

Figure 46: Tilt values with fit parameters for run-matching of Monogem data.

The norm values are also located around their ideal value, albeit showing an outlying value at 1.5, indicating that either the telescope system or atmosphere showed a different behaviour than the mean of its corresponding ON run.

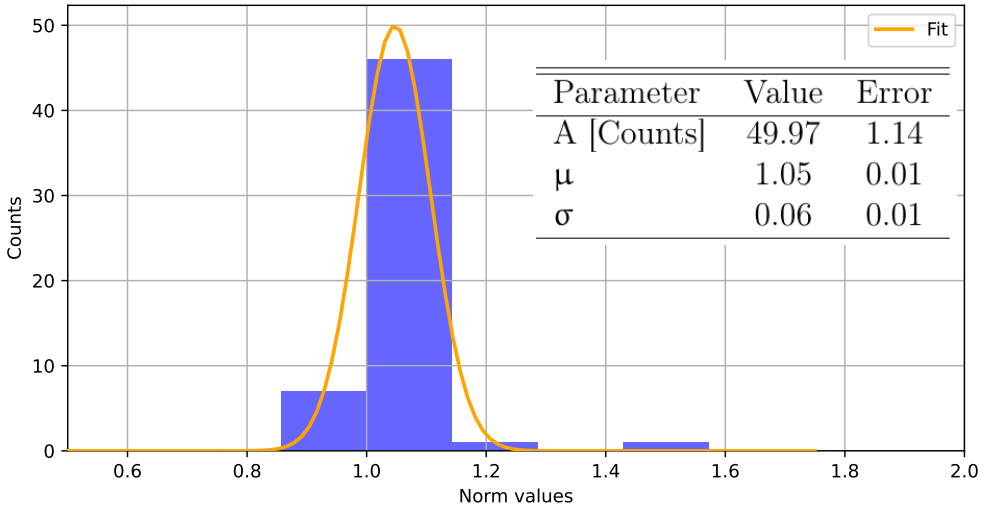

Figure 47: Norm values with fit parameters for run-matching of Monogem data.

The resulting $\sqrt{TS}$ map can be seen in Fig. 48, showing a different shape than the FoV background produced map. The position of the pulsar from Table 14 is indicated by the black dot, whereas the 5σ contours are depicted by green lines. It can be seen that extended emission can now be seen around the pulsar, as well as in other regions of the observed FoV.

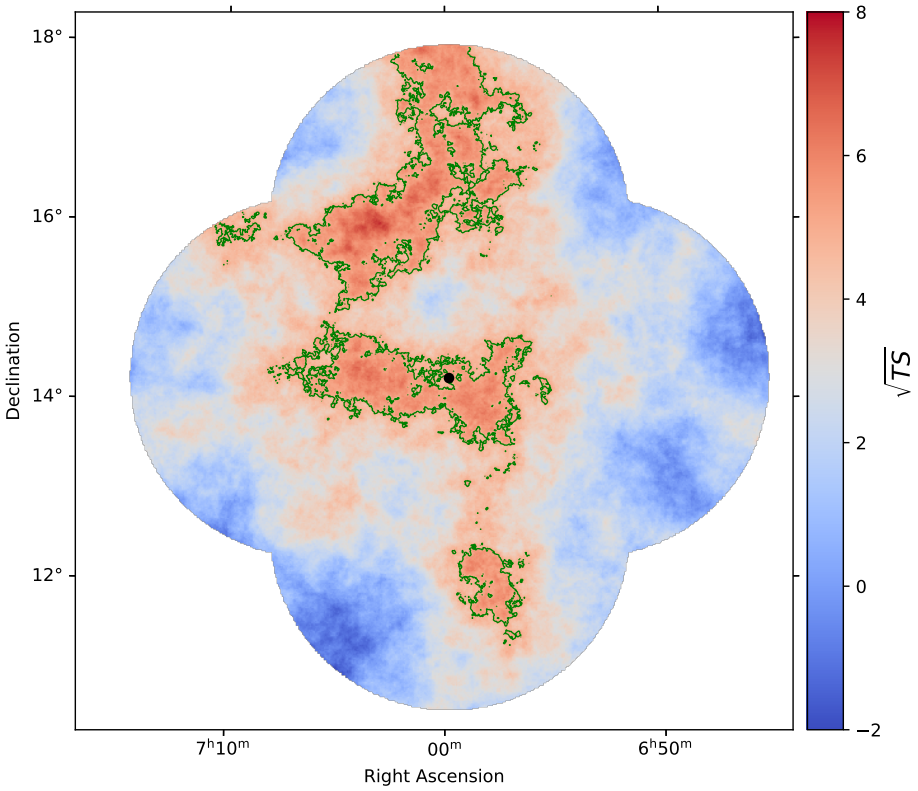

Figure 48: $\sqrt{TS}$ map of the Monogem region using run-matching. The correlation radius is 0.6° in this case and the Monogem pulsar according to Table 14 is indicated by a black dot, whereas the 5σ contours are depicted by green lines.

When comparing this map to Fig. 41 then reveals that the dominant emission regions in the top and bottom parts are now occurring again. The centre emission differs almost completely from the FoV background estimated one, given the now arising emission above 5σ. This emission is of extended nature and morphologically not describable by a simple geometrical structure. Furthermore it seems that the emission in the top region is more dominant than the one around the Monogem pulsar. This emission could be due to the TeV halos extend, since no pulsar could be found to be within the vicinity of Monogem using (Manchester et al., 2005; ATNF Catalogue, 2025c), nor is there a TeV emitting source listed in the TeVCat catalogue (Wakely et al., 2008). The same occurs for the bottom region, which also shows some emission above 5σ, although at smaller extend than its counterparts in the top region. In conclusion, the observed emission is held to be accountable from the Monogem pulsar halo, since it is so far the only source to have shown TeV emission in this region.

4.3 Analysis

Typically the next step in the analysis would require the spatial and spectral modelling of the sources within the region. This however can not be done in this case, as the energy bias of the DL3 datasets was wrongly produced. Thereby, the bias curve in Fig. 49 shows a systematic shift in the curve, thus provoking a wrongly estimated reconstructed energy for the dataset.

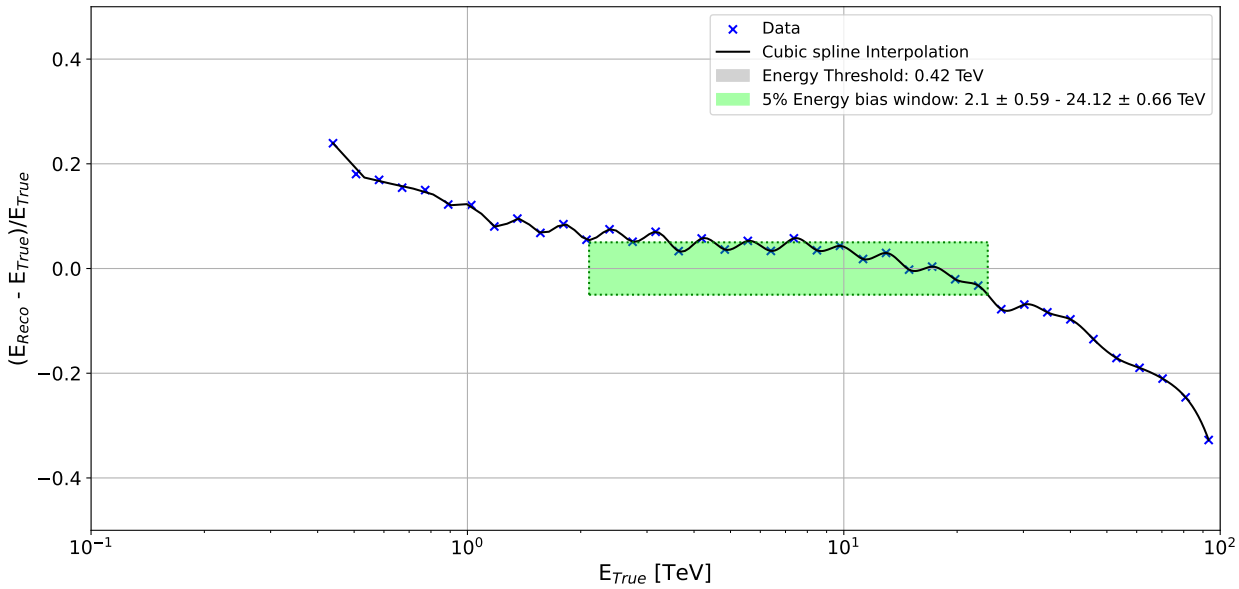

Figure 49: Energy dispersion curve of the run-matched Monogem dataset together with energy threshold as well as 5% bias window.

This makes it unfortunately not advisable to consider an analysis of the region using models based on the reconstructed energy. One could argue that an analysis using a narrow range between $2.1 - 24.12$ TeV could be done, since it is roughly within a 5% bias range. This however is not advisable, since the problem can be traced down to the DL3 data files, which itself create a systematic error. Thereby, the production of the sky map in Fig. 48 shows equal systematics for both ON and OFF runs, which makes itself affected by them. Yet, the produced map can still be used for general discussions like the shape and emission within the region, which will now be done.

4.4 Discussion

Even though the resulting DL4 product of the analysis showed a corrupted energy bias curve, it can at least be stated that the run-matching presents a fitting alternative compared to the FoV background method. Thereby it could be observed that when using an exclusion mask of circular shape with 2° radius resulted in the produced sky map to be dominated by a background overestimation. Even though the excluded region was estimated by the results of Abeysekara et al. (2017), it clearly did not provoke an adequate background reduction.

Yet, the norm and tilt distributions of the background model applied did not indicate any unusual behaviour that could have occurred during the reduction, the resulting $\sqrt{TS}$ map did so. It turned out the applied masks did not account for all the emission within the region, hence the reason the significance distributions with and without masks looked almost the same. Thereby it was not possible to do an analysis using this background reduction method, since the resulting $\sqrt{TS}$ map showed no significant (i.e, above 5σ) emission.
Since the "traditional" method of FoV background reduction did not yield any detectable emission from the source, an attempt was made to apply ON-OFF run-matching. Thereby the database of possible OFF runs was searched using run-matching parameters depicted in Table 5, which were already used for the analysis of PSR B1046-58. Having seen that using more relaxed parameters than recommended by Wach et al. (2024) results in similar outcomes as traditional methods did for PSR B1046-58, made it thus possible to apply this method again for Monogem. Although the fractional run deviation indicated a larger deviation for some runs, the fixed zenith angle and livetime histograms showed that at least these parameters are to most extend within expectable values. It is hereby necessary to notice that at least for the livetime histogram a larger deviation between ON and OFF runs has occurred. Thereby, a couple of OFF runs showed run times barely over 20 min, whereas some ON runs showed run duration around 35 min. Since these runs were however not matched with each other but rather with one in the corresponding range, deviations due to this factor could be ruled out. Yet, since these parameters were still within bounds of reasonable values, the background reduction was still performed leading to the $\sqrt{TS}$ map as seen in Fig. 48. Having reasonable norm and tilt values, with only one small outlier for the former parameter, made it clear that the background reduction resulted in reasonable background model fits. This could be confirmed by the general emission seen in the produced $\sqrt{TS}$ map, which showed an extended emission of $\sim 2^\circ$ extend around the Monogem pulsar. Since the extension of the Monogem pulsar halo is estimated to be of the same size by Abeysekara et al. (2017), the conclusion that the run-matching provides better values was made. Furthermore it could be seen that extended emission around the position of PSR B0656+14 was then present, which was in contrast to the FoV map. Additionally, emission that was present in the FoV map towards the top and bottom edge of the map could now be seen in a more amplified manner. The origin of this emission could not be traced down to be due to a pulsar or any other known TeV source using the ATNF catalogue (Manchester et al., 2005; ATNF Catalogue, 2025c) and TeVCat (Wakely et al., 2008). Thereby it is here estimated that the measured emission is associated to the pulsar itself, since the extend of the measured γ-rays by Abeysekara et al. (2017) goes beyond the 2°, showing $\sqrt{TS} > 5$ values in a region of $\sim 4^\circ$ in total. Therefore, the entire emission is hereby accounted to be coming from the Monogem pulsar halo that has formed around the PWN hosted by PSR B0656+14.
However, an analysis going further into detail about the modelling of the source could not be made, as it turned out that the DL3 (and therefore also the DL4) data has a wrongly estimated energy dispersion. As could be seen in Fig. 49, the bias curve only goes below an acceptable 5% bias percentage within a tiny window between $2.1 - 24.12$ TeV, which is a very narrow range for an analysis. Furthermore, this makes the background estimation also affected by this bias shift, thus making all spectral analysis systematically biased. Yet, the morphological discussions earlier made are still valid, since the bias itself affects both ON and OFF runs alike, and is therefore accounted in the same manner during the reduction. Thereby, the map that could be seen is only usable under general morphological discussions

but not in any way for spectral modelling. In conclusion to these discussions, it can thereby only stated that the ON-OFF run-matching method can indeed improve the estimation of backgrounds in large regions of γ-ray emission. Additionally it could be seen that the HESSIu data taken from the Monogem region could in future provide valuable insights about the TeV halo within the region.

5 Summary & Conclusions

This work has dealt with the analysis of the two extended γ-ray sources around PSR B1046-58 and PSR B0656+14. Thereby, the former source has been analysed using the "traditional" methods of FoV and ring background reduction as well as the recently developed ON-OFF run-matching. A comparison between the three methods was done, resulting in the FoV method to be the best fitting one. The dataset obtained using this method was then further used and a grid model was lain upon the region in order to extract the spectral parameters. Thereby, it turned out that the grid centred around PSR B1046-58 showed not only the highest energy flux integral value but also an index that allowed the emitted γ-ray emission to be stemming from within the region. Additionally, emission from Westerlund 2 was briefly discussed, and it was found that the emission around Eta Carinae is of diffuse extended type. In conclusion to these characteristics, it was found that the reported $1/r$ emission detected by Yang et al. (2018) for Fermi LAT data above 10 GeV could not be observed in this case. Therefore, it was concluded that the detected γ-ray emission above 1.16 TeV within the vicinity of PSR B1046-58 is not stemming from an extended emission from Westerlund 2. Therefore, it was decided to fit a radiation model to the flux points extracted here as well as the reported flux points ranging from radio to sub-TeV band. Thereby photons arising from synchrotron and IC scattering processes were taken into account. The resulting MCMC fit gave an overall well fitting result for both emission types, although it was necessary to assume a systematic bias of the MCMC sampled fit values. Thereby, it is most likely that the most dominant processes leading to the observed SED are the synchrotron and IC scattering, albeit leaving out possible contributions of pion decay as well as Bremsstrahlung. Nevertheless, the hereby presented discussion of the surrounding region of PSR B1046-58 was the first one taking all the different reported fluxes across the radio to γ-ray band into account. Therefore, getting better results than found here would require more measurements in the lower TeV domain as well as in the higher γ-ray range. Additionally, using data that is not affected by NSB values could prove the earlier mentioned overestimation of the flux in the region. In conclusion, it can be stated the hereby made observations and data analysis of the region surrounding PSR B1046-58 led to the conclusion that a PWN is the most probable source of the detected γ-ray emission, albeit requiring further measurements in this domain to confirm this result.

In the second part of this work, an analysis of the region surrounding PSR B0656+14 was done, which however led to less conclusions that could be drawn from it. Even though it could be shown that the newly developed method of ON-OFF run-matching led to a significant improvement of the background reduction, no further analysis could be made due to a corrupted energy bias. Therefore, the studies using HESSIu data could only be used to describe the morphological shape of the region. Thereby, studies that use no such corrupted HESS Iu data could reveal the true characteristics of the TeV emission in the region.

Bibliography

Abdalla, H., A. Abramowski, et al. (Apr. 2018). "The H.E.S.S. Galactic plane survey". In: *Astronomy & Astrophysics* 612, A1. ISSN: 1432-0746. DOI: 10.1051/0004-6361/201732098. URL: http://dx.doi.org/10.1051/0004-6361/201732098.

Abdalla, H., R. Adam, et al. (Mar. 2020). "Detection of very-high-energy γ-ray emission from the colliding wind binary η Car with H.E.S.S." In: *Astronomy & amp; Astrophysics* 635, A167. ISSN: 1432-0746. DOI: 10.1051/0004-6361/201936761. URL: http://dx.doi.org/10.1051/0004-6361/201936761.

Abdo, Aous A et al. (2010). "Fermi large area telescope observation of a gamma-ray source at the position of Eta Carinae". In: *The Astrophysical Journal* 723.1, p. 649.

Abdollahi, S. et al. (Mar. 2020). "Fermi Large Area Telescope Fourth Source Catalog". In: *The Astrophysical Journal Supplement Series* 247.1, p. 33. DOI: 10.3847/1538-4365/ab6bcb. URL: https://dx.doi.org/10.3847/1538-4365/ab6bcb.

Abdollahi, S. et al. (July 2022). "Search for New Cosmic-Ray Acceleration Sites within the 4FGL Catalog Galactic Plane Sources". In: *The Astrophysical Journal* 933.2, p. 204. DOI: 10.3847/1538-4357/ac704f. URL: https://dx.doi.org/10.3847/1538-4357/ac704f.

Abeysekara, A. U. et al. (July 2017). "The 2HWC HAWC Observatory Gamma-Ray Catalog". In: *The Astrophysical Journal* 843.1, 40, p. 40. DOI: 10.3847/1538-4357/aa7556. arXiv: 1702.02992 [astro-ph.HE].

Acero, Fabio et al. (Feb. 2024). *Gammapy: Python toolbox for gamma-ray astronomy*. Version v1.2. DOI: 10.5281/zenodo.10726484. URL: https://doi.org/10.5281/zenodo.10726484.

Aharonian, F, J Buckley, et al. (Aug. 2008). "High energy astrophysics with ground-based gamma ray detectors". In: *Reports on Progress in Physics* 71.9, p. 096901. DOI: 10.1088/0034-4885/71/9/096901. URL: https://dx.doi.org/10.1088/0034-4885/71/9/096901.

Aharonian, F., A.G. Akhperjanian, K.-M. Aye, et al. (2004). "Calibration of cameras of the H.E.S.S. detector". In: *Astroparticle Physics* 22.2, pp. 109–125. ISSN: 0927-6505. DOI: https://doi.org/10.1016/j.astropartphys.2004.06.006. URL: https://www.sciencedirect.com/science/article/pii/S0927650504001227.

Aharonian, Felix, AG Akhperjanian, AR Bazer-Bachi, et al. (2006). "Observations of the Crab nebula with HESS". In: *Astronomy & Astrophysics* 457.3, pp. 899–915.

Anchordoqui, L. A. et al. (Oct. 1999). "Heavy nuclei at the end of the cosmic-ray spectrum?" In: *Physical Review D* 60.10. ISSN: 1089-4918. DOI: 10.1103/physrevd.60.103001. URL: http://dx.doi.org/10.1103/PhysRevD.60.103001.

Ashton, T. et al. (2020). "A NECTAr-based upgrade for the Cherenkov cameras of the H.E.S.S. 12-meter telescopes". In: *Astroparticle Physics* 118, p. 102425. ISSN: 0927-6505. DOI: https://doi.org/10.1016/j.astropartphys.2019.102425. URL: https://www.sciencedirect.com/science/article/pii/S0927650519302282.

ATNF Catalogue, Web address of (2025a). *ATNF Pulsar Catalogue (v.2.5.1)*. online. Accessed: 2025-01-17. URL: https://www.atnf.csiro.au/research/pulsar/psrcat/proc_form.php?version=2.5.1&Name=Name&JName=JName&RAJ=RAJ&DecJ=DecJ&startUserDefined=true&sort_attr=jname&sort_order=asc&condition=&coords_unit=raj%2Fdecj&radius=&coords_1=&coords_2=&pulsar_names=%0D%0A&ephemeris=short&ephemeris_submit=&style=long+with+last+digit+error&no_value=*&fsize=3&x_axis=&x_scale=linear&y_axis=&y_scale=linear&state=query.

– (2025b). *ATNF Pulsar Catalogue (v.2.5.1) web adress for Pulsar B0656+14*. online. Accessed: 2025-01-29. URL: https://www.atnf.csiro.au/research/pulsar/psrcat/proc_form.php?version=2.5.1&Name=Name&RAJ=RAJ&DecJ=DecJ&P0=P0&P1=P1&Dist=Dist&Age=Age&BSurf=BSurf&Edot=Edot&startUserDefined=true&sort_attr=jname&sort_order=asc&condition=&coords_unit=raj%2Fdecj&radius=&coords_1=&coords_2=&pulsar_names=B0656%2B14%0D%0A&ephemeris=long&ephemeris_submit=&style=long+with+last+digit+error&no_value=*&fsize=3&x_axis=&x_scale=linear&y_axis=&y_scale=linear&state=query.

– (2025c). *ATNF Pulsar Catalogue (v.2.5.1) web adress for Pulsar B1046-58*. online. Accessed: 2025-01-15. URL: https://www.atnf.csiro.au/research/pulsar/psrcat/proc_form.php?startUserDefined=true&c1_val=&c2_val=&c3_val=&c4_val=&sort_attr=jname&sort_order=asc&condition=&pulsar_names=B1046-58&ephemeris=long&submit_ephemeris=Get+Ephemeris&coords_unit=raj%2Fdecj&radius=&coords_1=&coords_2=&style=Long+with+last+digit+error&no_value=*&x_axis=&x_scale=linear&y_axis=&y_scale=linear&state=query.

Atoyan, A.M. et al. (Jan. 1999). "Modelling of the non-thermal flares in the Galactic microquasar GRS 1915+105". In: *Monthly Notices of the Royal Astronomical Society* 302.2, pp. 253–276. DOI: 10.1046/j.1365-8711.1999.02172.x.

Atwood, W. B. et al. (May 2009). "THE LARGE AREA TELESCOPE ON THE FERMI GAMMA-RAY SPACE TELESCOPE MISSION". In: *The Astrophysical Journal* 697.2, p. 1071. DOI: 10.1088/0004-637X/697/2/1071. URL: https://dx.doi.org/10.1088/0004-637X/697/2/1071.

Bartelmann, Matthias et al. (2018). *Theoretische Physik 3: Quantenmechanik*. Vol. 1. Springer Spektrum Berlin, Heidelberg. ISBN: ISBN 978-3-662-56071-6. DOI: https://doi.org/10.1007/978-3-662-56072-3.

Beck, R. (Jan. 1983). "Magnetfelder in Spiralgalaxien". In: *Mitteilungen der Astronomischen Gesellschaft Hamburg* 60, p. 208.

Benbow, Wystan et al. (2005). "The status and performance of HESS". In: *AIP Conference Proceedings*. Vol. 745. 1. American Institute of Physics, pp. 611–616.

Berge, David et al. (2007). "Background modelling in very-high-energy γ-ray astronomy". In: *Astronomy & Astrophysics* 466.3, pp. 1219–1229.

Bevington, PR et al. (2003). *Data reduction and error analysis for the physical sciences, 3rd McGraw-Hill*. Vol. 3. McGraw-Hill: New York City.

Bi, Baiyang et al. (2021). "Performance of the new FlashCam-based camera in the 28m telescope of H.E.S.S." In: *PoS* ICRC2021, p. 743. DOI: 10.22323/1.395.0743.

Blum, Kfir et al. (2017). *Cosmic-ray Antimatter*. arXiv: 1709.06507 [astro-ph.HE]. URL: https://arxiv.org/abs/1709.06507.

Bosch-Ramon, V. et al. (Mar. 2005). "Electromagnetic radiation initiated by hadronic jets from microquasars in the ISM". In: *Astronomy & Astrophysics* 432.2, pp. 609–618. ISSN: 1432-0746. DOI: 10.1051/0004-6361:20041794. URL: http://dx.doi.org/10.1051/0004-6361:20041794.

Candia, Julián et al. (May 2003). "Cosmic ray spectrum and anisotropies from the knee to the second knee". In: *Journal of Cosmology and Astroparticle Physics* 2003.05, p. 003. DOI: 10.1088/1475-7516/2003/05/003. URL: https://dx.doi.org/10.1088/1475-7516/2003/05/003.

Cerda-Duran, Pablo et al. (2018). "Neutron Stars Formation and Core Collapse Supernovae". In: *The Physics and Astrophysics of Neutron Stars*. Springer International Publishing, pp. 1–56. ISBN: 9783319976167. DOI: 10.1007/978-3-319-97616-7_1. URL: http://dx.doi.org/10.1007/978-3-319-97616-7_1.

Cesarsky, Catherine J et al. (1983). "Gamma rays from active regions in the galaxy: The possible contribution of stellar winds". In: *Space Science Reviews* 36.2, pp. 173–193. DOI: https://doi.org/10.1007/BF00167503.

Cirkel-Bartelt, Vanessa (2008). "History of Astroparticle Physics and its Components". In: *Living Reviews in Relativity* 11.2. Online Article, cited [28.01.2025]. URL: http://www.livingreviews.org/lrr-2008-2.

Collaboration, HESS et al. (July 2012). "HESS observations of the Carina nebula and its enigmatic colliding wind binary Eta Carinae". In: *Monthly Notices of the Royal Astronomical Society* 424.1, pp. 128–135. ISSN: 0035-8711. DOI: 10.1111/j.1365-2966.2012.21180.x. eprint: https://academic.oup.com/mnras/article-pdf/424/1/128/3259178/mnras0424-0128.pdf. URL: https://doi.org/10.1111/j.1365-2966.2012.21180.x.

Compton, Arthur H. (May 1933). "Nature of Cosmic Rays". In: *Nature* 131.3316, pp. 713–715. DOI: 10.1038/131713a0.

Corcoran, M. F. et al. (Mar. 2017). "The 2014 X-Ray Minimum of η Carinae as Seen by Swift". In: *The Astrophysical Journal* 838.1, p. 45. DOI: 10.3847/1538-4357/aa6347. URL: https://dx.doi.org/10.3847/1538-4357/aa6347.

Cornils, R. et al. (Jan. 2005). "The optical system of the H.E.S.S. II telescope". In: *29th International Cosmic Ray Conference (ICRC29), Volume 5*. Ed. by B. Sripathi Acharya et al. Vol. 5. International Cosmic Ray Conference, p. 171.

Cowan, Glen (2019). "Statistical models with uncertain error parameters". In: *The European Physical Journal C* 79.2, p. 133. ISSN: 1434-6052. DOI: 10.1140/epjc/s10052-019-6644-4. URL: https://doi.org/10.1140/epjc/s10052-019-6644-4.

Davies, John M. et al. (1957). "Design of the quartermaster solar furnace". In: *Solar Energy* 1.2, pp. 16–22. ISSN: 0038-092X. DOI: https://doi.org/10.1016/0038-092X(57)90116-0. URL: https://www.sciencedirect.com/science/article/pii/0038092X57901160.

De Angelis, Alessandro et al. (2018). *Introduction to particle and astroparticle physics: multimessenger astronomy and its particle physics foundations*. Vol. 2. Springer. DOI: https://doi.org/10.1007/978-3-319-78181-5.

Demtröder, Wolfgang (2017). *Experimentalphysik 4: Kern-, Teilchen-und Astrophysik*. Vol. 5. Springer Spektrum Berlin, Heidelberg. ISBN: 978-3-662-52883-9. DOI: https://doi.org/10.1007/978-3-662-52884-6.

Donath, Axel et al. (2023). "Gammapy: A Python package for gamma-ray astronomy". In: *Astronomy & Astrophysics* 678, A157.

Drury, Luke O'C. (2012). "Origin of cosmic rays". In: *Astroparticle Physics* 39-40. Cosmic Rays Topical Issue, pp. 52–60. ISSN: 0927-6505. DOI: https://doi.org/10.1016/j.astropartphys.2012.02.006. URL: https://www.sciencedirect.com/science/article/pii/S092765051200045X.

Elster, E (1901). "Weitere Versuche über die Elektrizitätszerstreuung in abgeschlossen Luftmengen." In: *Physik. Z.* 2, pp. 560–563.

Evoli, Carmelo (Dec. 2020). *The Cosmic-Ray Energy Spectrum*. DOI: 10.5281/zenodo.4396125. URL: https://doi.org/10.5281/zenodo.4396125.

Fixsen, D. J. (Nov. 2009). "The temperature of the cosmic microwave background". In: *The Astrophysical Journal* 707.2, p. 916. DOI: 10.1088/0004-637X/707/2/916. URL: https://dx.doi.org/10.1088/0004-637X/707/2/916.

Foreman-Mackey, D. et al. (2013). "emcee: The MCMC Hammer". In: *PASP* 125, pp. 306–312. DOI: 10.1086/670067. eprint: 1202.3665.

Forster, Otto (2004). *Analysis 1: Differential- und Integralrechnung einer Veränderlichen*. Vol. 12. Springer. ISBN: 978-3-658-11544-9. DOI: 10.1007/978-3-658-11545-6.

Gaensler, Bryan M. et al. (Sept. 2006). "The Evolution and Structure of Pulsar Wind Nebulae". In: *Annual Review of Astronomy and Astrophysics* 44.1, pp. 17–47. ISSN: 1545-4282. DOI: 10.1146/annurev.astro.44.051905.092528. URL: http://dx.doi.org/10.1146/annurev.astro.44.051905.092528.

Gammapy (2024). *Instrument Response Functions (DL3)*. Accessed: 2025-01-05. URL: https://docs.gammapy.org/dev/user-guide/irf/index.html.

Gaug, M. et al. (July 2019). "Using Muon Rings for the Calibration of the Cherenkov Telescope Array: A Systematic Review of the Method and Its Potential Accuracy". In: *The Astrophysical Journal Supplement Series* 243.1, 11, p. 11. DOI: 10.3847/1538-4365/ab2123. arXiv: 1907.04375 [astro-ph.IM].

Gehrels, Neil et al. (2012). "Gamma-Ray Bursts". In: *Science* 337.6097, pp. 932–936. DOI: 10.1126/science.1216793. eprint: https://www.science.org/doi/pdf/10.1126/

science.1216793. URL: https://www.science.org/doi/abs/10.1126/science.1216793.

Geitel, Hans (1900). "Über die Elektrizitätszerstreuung in abgeschlossenen Luftmengen". In: *Phys. Z* 2, pp. 116–119.

Giacinti, G et al. (2020). "Halo fraction in TeV-bright pulsar wind nebulae". In: *Astronomy & Astrophysics* 636, A113.

Gonzalez, M. E. et al. (Nov. 2006). "Chandra and XMM-Newton Observations of the Vela-like Pulsar B1046–58". In: *The Astrophysical Journal* 652.1, p. 569. DOI: 10.1086/507125. URL: https://dx.doi.org/10.1086/507125.

Gottschall, Daniel et al. (2015). *The Mirror Alignment and Control System for CT5 of the H.E.S.S. experiment.* arXiv: 1509.04100 [astro-ph.IM]. URL: https://arxiv.org/abs/1509.04100.

Hahn, J., R. de los Reyes, et al. (Feb. 2014). "Impact of aerosols and adverse atmospheric conditions on the data quality for spectral analysis of the H.E.S.S. telescopes". In: *Astroparticle Physics* 54, pp. 25–32. DOI: 10.1016/j.astropartphys.2013.10.003. arXiv: 1310.1639 [astro-ph.IM].

Hahn, Joachim, Carlo Romoli, et al. (2022). "GAMERA: Source modeling in gamma astronomy". In: *Astrophysics Source Code Library*, ascl–2203.

Halley, Edmund (1679). *Catalogus stellarum australium; sive, Supplementum catalogi Tychenici, exhibens longitudines et latitudines stellarum fixarum, quae, prope polum Antarcticum sitae, in horizonte Uraniburgico Tychoni inconspicuae fuere, accurato calculo ex distantiis supputatas, & ad annum 1677 completum correctas ... Accedit appendicula de rebus quibusdam astronomicis.* Archived from the original on 6 November 2015. London, UK: T. James, p. 13.

Harding, Alice K et al. (Aug. 2006). "Physics of strongly magnetized neutron stars". In: *Reports on Progress in Physics* 69.9, p. 2631. DOI: 10.1088/0034-4885/69/9/R03. URL: https://dx.doi.org/10.1088/0034-4885/69/9/R03.

Hartman, R. C. et al. (July 1999). "The Third EGRET Catalog of High-Energy Gamma-Ray Sources". In: *The Astrophysical Journal Supplement Series* 123.1, p. 79. DOI: 10.1086/313231. URL: https://dx.doi.org/10.1086/313231.

Hess, Victor Francis (1912). "Über Beobachtungen der durchdringenden Strahlung bei sieben Freiballonfahrten". In: *Z. Phys.* 13, p. 1084.

Hewish, Antony et al. (1979). "74. Observation of a Rapidly Pulsating Radio Source". In: *A Source Book in Astronomy and Astrophysics, 1900–1975.* Ed. by Kenneth R. Lang et al. Cambridge, MA and London, England: Harvard University Press, pp. 498–504. ISBN: 9780674366688. DOI: doi:10.4159/harvard.9780674366688.c80. URL: https://doi.org/10.4159/harvard.9780674366688.c80.

Hillas, A Michael (1985). "Cerenkov light images of EAS produced by primary gamma". In: *19th Intern. Cosmic Ray Conf-Vol. 3.* OG-9.5-3.

Hinton, J.A. et al. (2009). "Teraelectronvolt Astronomy". In: *Annual Review of Astronomy and Astrophysics* 47.Volume 47, 2009, pp. 523–565. ISSN: 1545-4282. DOI: https://doi.org/10.1146/annurev-astro-082708-101816. URL: https://www.annualreviews.org/content/journals/10.1146/annurev-astro-082708-101816.

Iping, Rosina C et al. (2005). "Detection of a hot binary companion of η Carinae". In: *The Astrophysical Journal* 633.1, p. L37.

Jankowski, F et al. (Dec. 2018). "The UTMOST pulsar timing programme I: Overview and first results". In: *Monthly Notices of the Royal Astronomical Society* 484.3, pp. 3691–3712. ISSN: 1365-2966. DOI: 10.1093/mnras/sty3390. URL: http://dx.doi.org/10.1093/mnras/sty3390.

Jardin-Blicq, Armelle (June 2019). "The TeV γ-ray emission of the Galactic Plane. HAWC and H.E.S.S. observations of the Galactic Plane and detailed study of the region surrounding 2HWC J1928+177." Theses. Ruperto-Carola University of Heidelberg. URL: https://hal.science/tel-03347146.

Johnston, Simon et al. (1992). "A high-frequency survey of the southern Galactic plane for pulsars". In: *Monthly Notices of the Royal Astronomical Society* 255.3, pp. 401–411.

Kirk, John G. et al. (2009). "The Theory of Pulsar Winds and Nebulae". In: *Neutron Stars and Pulsars*. Ed. by Werner Becker. Berlin, Heidelberg: Springer Berlin Heidelberg, pp. 421–450. ISBN: 978-3-540-76965-1. DOI: 10.1007/978-3-540-76965-1_16. URL: https://doi.org/10.1007/978-3-540-76965-1_16.

Lee, Jane J (May 2013). "Women scientists who were snubbed due to sexism". In: *National Geographic* 19.

Li, T. et al. (Sept. 1983). "Analysis methods for results in gamma-ray astronomy." In: *Astrophysical Journal* 272, pp. 317–324. DOI: 10.1086/161295.

Linden, Tim et al. (Nov. 2017). "Using HAWC to discover invisible pulsars". In: *Phys. Rev. D* 96 (10), p. 103016. DOI: 10.1103/PhysRevD.96.103016. URL: https://link.aps.org/doi/10.1103/PhysRevD.96.103016.

Lu, C. -C. (2013). *Improving the H.E.S.S. angular resolution using the Disp method*. arXiv: 1310.1200 [astro-ph.IM]. URL: https://arxiv.org/abs/1310.1200.

MacKay, David JC (Mar. 2003). *Information theory, inference and learning algorithms*. Vol. 7.2. Cambridge university press.

Manchester, R. N. et al. (Apr. 2005). "The Australia Telescope National Facility Pulsar Catalogue". In: *The Astronomical Journal* 129.4, p. 1993. DOI: 10.1086/428488. URL: https://dx.doi.org/10.1086/428488.

Milikan, RA (1926). "High frequency rays of cosmic origin". In: *Proceedings of the National Academy of Sciences* 12, p. 48.

Mirabel, I. Félix (2007). "Microquasars". In: *Comptes Rendus Physique* 8.1. Observation of black holes and extreme gravitational events, pp. 7–15. ISSN: 1631-0705. DOI: https:

//doi.org/10.1016/j.crhy.2006.12.001. URL: https://www.sciencedirect.com/science/article/pii/S1631070506002830.

Mohrmann, Lars et al. (2019). "Validation of open-source science tools and background model construction in γ-ray astronomy". In: *Astronomy & Astrophysics* 632, A72.

Navas, S. et al. (2024). "Review of particle physics". In: *Phys. Rev. D* 110.3, p. 030001. DOI: 10.1103/PhysRevD.110.030001.

Nigro, Cosimo et al. (2021). "Evolution of Data Formats in Very-High-Energy Gamma-Ray Astronomy". In: *Universe* 7.10. ISSN: 2218-1997. DOI: 10.3390/universe7100374. URL: https://www.mdpi.com/2218-1997/7/10/374.

Parsons, R.D. et al. (2014). "A Monte Carlo template based analysis for air-Cherenkov arrays". In: *Astroparticle Physics* 56, pp. 26–34. ISSN: 0927-6505. DOI: https://doi.org/10.1016/j.astropartphys.2014.03.002. URL: https://www.sciencedirect.com/science/article/pii/S0927650514000231.

Pittori, C. et al. (2009). "First AGILE catalog of high-confidence gamma-ray sources". In: *A&A* 506.3, pp. 1563–1574. DOI: 10.1051/0004-6361/200911783. URL: https://doi.org/10.1051/0004-6361/200911783.

Pivovaroff, M. J. et al. (Jan. 2000). "ASCA Observations of the Young Rotation-powered Pulsars PSR B1046–58 and PSR B1610–50". In: *The Astrophysical Journal* 528.1, p. 436. DOI: 10.1086/308139. URL: https://dx.doi.org/10.1086/308139.

Popescu, C. C. et al. (Sept. 2017a). "A radiation transfer model for the Milky Way: I. Radiation fields and application to high-energy astrophysics". In: *Monthly Notices of the Royal Astronomical Society* 470.3, pp. 2539–2558. DOI: 10.1093/mnras/stx1282. arXiv: 1705.06652 [astro-ph.GA].

– (June 2017b). *VizieR Online Data Catalog: Radiation fields of the Milky Way (Popescu+, 2017).*

Ptuskin, V.S. et al. (Oct. 1981). "The Galactic Center and the Origin of Cosmic Rays". In: *Soviet Astronomy* 25, p. 547.

Pühlhofer, G., M. Barcelo, et al. (2019). "FlashCam: a fully digital camera for the Cherenkov telescope array medium-sized telescopes". In: *Optics for EUV, X-Ray, and Gamma-Ray Astronomy IX*. Ed. by Stephen L. O'Dell et al. Vol. 11119. International Society for Optics and Photonics. SPIE, p. 111191V. DOI: 10.1117/12.2531025. URL: https://doi.org/10.1117/12.2531025.

Pühlhofer, Gerd, Fabian Leuschner, et al. (2024). "HESS: The High Energy Stereoscopic System". In: *Handbook of X-ray and Gamma-ray Astrophysics*. Springer, pp. 2745–2785.

Rieger, Frank M. (Nov. 2022). "Active Galactic Nuclei as Potential Sources of Ultra-High Energy Cosmic Rays". In: *Universe* 8.11, p. 607. ISSN: 2218-1997. DOI: 10.3390/universe8110607. URL: http://dx.doi.org/10.3390/universe8110607.

Romero, G. E. et al. (Aug. 2018). "Particle acceleration in the superwinds of starburst galaxies". In: *Astronomy & Astrophysics* 616, A57. ISSN: 1432-0746. DOI: 10.1051/0004-6361/201832666. URL: http://dx.doi.org/10.1051/0004-6361/201832666.

Röntgen, W. C. (1898). "Ueber eine neue Art von Strahlen". In: *Annalen der Physik* 300.1, pp. 12–17. DOI: https://doi.org/10.1002/andp.18983000103. eprint: https://onlinelibrary.wiley.com/doi/pdf/10.1002/andp.18983000103. URL: https://onlinelibrary.wiley.com/doi/abs/10.1002/andp.18983000103.

Slane, Patrick (2017). "Pulsar Wind Nebulae". In: *Handbook of Supernovae*. Springer International Publishing, pp. 2159–2179. ISBN: 9783319218465. DOI: 10.1007/978-3-319-21846-5_95. URL: http://dx.doi.org/10.1007/978-3-319-21846-5_95.

Smith, Nathan (Apr. 2006). "A census of the Carina Nebula — I. Cumulative energy input from massive stars". In: *Monthly Notices of the Royal Astronomical Society* 367.2, pp. 763–772. ISSN: 0035-8711. DOI: 10.1111/j.1365-2966.2006.10007.x. eprint: https://academic.oup.com/mnras/article-pdf/367/2/763/3310271/367-2-763.pdf. URL: https://doi.org/10.1111/j.1365-2966.2006.10007.x.

Steinmassl, Simon et al. (2023). "The Eta Carinae 2020 periastron passage as seen by H.E.S.S." In: *PoS* ICRC2023, p. 640. DOI: 10.22323/1.444.0640.

Sudoh, Takahiro et al. (Aug. 2019). "TeV halos are everywhere: Prospects for new discoveries". In: *Physical Review D* 100.4, 043016, p. 043016. DOI: 10.1103/PhysRevD.100.043016. arXiv: 1902.08203 [astro-ph.HE].

Syrovatskii, S.I. (Feb. 1959). "The Distribution of Relativistic Electrons in the Galaxy and the Spectrum of Synchrotron Radio Emission." In: *Soviet Astronomy* 3, p. 22.

Truelove, J. Kelly et al. (Feb. 1999). "Evolution of Nonradiative Supernova Remnants". In: *The Astrophysical Journal Supplement Series* 120.2, p. 299. DOI: 10.1086/313176. URL: https://dx.doi.org/10.1086/313176.

Vacanti, G. et al. (1994). "Muon ring images with an atmospheric Čerenkov telescope". In: *Astroparticle Physics* 2.1, pp. 1–11. ISSN: 0927-6505. DOI: https://doi.org/10.1016/0927-6505(94)90012-4. URL: https://www.sciencedirect.com/science/article/pii/0927650594900124.

Vats, Dootika et al. (2021). "Revisiting the Gelman–Rubin Diagnostic". In: *Statistical Science* 36.4, pp. 518–529. DOI: 10.1214/20-STS812. URL: https://doi.org/10.1214/20-STS812.

Virtanen, Pauli et al. (2020). "SciPy 1.0: Fundamental Algorithms for Scientific Computing in Python". In: *Nature Methods* 17, pp. 261–272. DOI: 10.1038/s41592-019-0686-2.

Wach, Tina et al. (2024). "A background-estimation technique for the detection of extended gamma-ray structures with IACTs". In: *Astronomy & Astrophysics* 690, A250.

Wakely, S. P. et al. (2008). "TeVCat: An online catalog for Very High Energy Gamma-Ray Astronomy". In: *International Cosmic Ray Conference* 3, pp. 1341–1344.

Wang, Chih-Yueh (2014). "Neutron Stars and Pulsars (IAU S291): Challenges and Opportunities after 80 Years, Proceedings of the International Astronomical Union (IAU S279), edited by Joeri van Leeuwen". In: *Contemporary Physics* 55.4, pp. 346–347. DOI: 10.1080/00107514.2014.933257. eprint: https://doi.org/10.1080/00107514.2014.933257. URL: https://doi.org/10.1080/00107514.2014.933257.

Watson, A A (Feb. 2014). "High-energy cosmic rays and the Greisen–Zatsepin–Kuz'min effect". In: *Reports on Progress in Physics* 77.3, p. 036901. DOI: 10.1088/0034-4885/77/3/036901. URL: https://dx.doi.org/10.1088/0034-4885/77/3/036901.

Wells, Donald Carson et al. (1979). "FITS-a flexible image transport system". In: *Image processing in astronomy*, p. 445.

Wenger, M. et al. (Apr. 2000). "The SIMBAD astronomical database. The CDS reference database for astronomical objects". In: *Astronomy and Astrophysics Supplement Series* 143, pp. 9–22. DOI: 10.1051/aas:2000332. arXiv: astro-ph/0002110 [astro-ph].

Westerlund, Bengt (1961). "A heavily reddened cluster in ara". In: *Publications of the Astronomical Society of the Pacific* 73.430, pp. 51–55.

Wilson, Charles TR (1900). "On the leakage of electricity through dust-free air". In: *Proc. Cambridge Philos. Soc.* Vol. 11, p. 32.

Yang, Rui-zhi et al. (2018). "Diffuse γ-ray emission in the vicinity of young star cluster Westerlund 2". In: *Astronomy & Astrophysics* 611, A77.

A Additions to the PSR B1046-58 Analysis

A.1 ON-OFF run-matches

Table 16: Matched ON-OFF runs for Monogem dataset.

OFF-ID	ON-ID
20711	20108
20734	20107
31756	32348
32467	32340, 32450, 31660, 32366, 32344
32468	32483, 32319
33901	32320
34981	32890
38283	30531, 30555
40906	55958, 55886, 55885, 56098
41958	55918
42286	51982
48259	45283, 45282
48274	45121
48336	45122, 51933, 56635, 56078, 51383, 56636, 51883, 56555, 56637, 56638, 56556
48838	56524
48890	56056, 56055, 55988, 55987
55341	56122, 55599, 56364, 55960, 56365
61456	62060, 62061
61500	61682

61530	61752, 61705, 61692, 61753, 62135, 62115, 61763, 62116
61537	61704
61538	61751, 61584, 61691
64864	64738, 64806
84448	80371, 80328, 80329, 80372, 83726, 83709

A.2 Flux point computation

In some cases only the integral energy flux and the spectral models are given in some reference papers. Therefore it is decided to show here how the $E^{2dN}/_{dE}$ flux points are calculated then. Luckily such a conversion is only necessary for the keV data given in (Gonzalez et al., 2006) and (Pivovaroff et al., 2000), which both use a power law to compute their flux points. In order to keep the formulations as general as possible, the calculation of the flux points begins with the definition of the power law, i.e.:

$$\phi(E) \propto E^{-\alpha} \implies \phi(E) = A \cdot E^{-\alpha}, \tag{28}$$

where A is some normalisation constant. Then the integral energy flux can be calculated from

$$F_e = \int_{E_1}^{E_2} dE\, E\phi(E) = \int_{E_1}^{E_2} dE\, A \cdot E^{-\alpha+1} = A\,\frac{E_2^{-\alpha+2} - E_1^{-\alpha+2}}{-\alpha+2}. \tag{29}$$

However, the problem is now the case if $\alpha = 2$, in which L'Hospital's rule (Forster, 2004) can be used. Thereby, the derivatives

$$f(\alpha) = E_2^{-\alpha+2} - E_1^{-\alpha+2} \implies f'(\alpha) = \frac{df}{d\alpha} = -\ln(E_2)E_2^{-\alpha+2} - \left(-\ln(E_1)E_1^{-\alpha+2}\right) \tag{30a}$$

$$g(\alpha) = -\alpha + 2 \implies g'(\alpha) = \frac{dg}{d\alpha} = -1 \tag{30b}$$

are computed first. One can now compute their limit, i.e.,

$$\lim_{\alpha \longrightarrow 2} \frac{f'(\alpha)}{g'(\alpha)} = \lim_{\alpha \longrightarrow 2} \left[\frac{-\ln(E_2)E_2^{-\alpha+2} - \left(-\ln(E_1)E_1^{-\alpha+2}\right)}{-1} \right] \tag{31a}$$

$$= \lim_{\alpha \longrightarrow 2} \left[\ln(E_2) \underbrace{E_2^{-\alpha+2}}_{\longrightarrow 1} - \ln(E_1) \underbrace{E_1^{-\alpha+2}}_{\longrightarrow 1} \right] \tag{31b}$$

$$= \ln(E_2) - \ln(E_1) \tag{31c}$$

$$= \ln\left(\frac{E_2}{E_1}\right) \tag{31d}$$

which is now equal to the limit of ${}^{f(\alpha)}/_{g(\alpha)}$ and thereby also the solution for $\alpha = 2$ in Eqn.(29). Finally, one gets

$$F_e = \begin{cases} A \ \ln\left(\frac{E_2}{E_1}\right) & , \text{ for } \alpha = 2 \\ \\ A \ \frac{E_2^{-\alpha+2} - E_1^{-\alpha+2}}{-\alpha+2} & , \text{ else} \end{cases} \tag{32}$$

which can now be used to compute the amplitude and then ${E^2 dN}/{dE}$ by own means.

B Additions to the Monogem Analysis

Table 17: Matched ON-OFF runs for Monogem dataset.

OFF-ID	ON-ID
165758	172090, 171589, 172067, 172155, 172200, 172154, 172156
166897	165193, 165232
167302	165244
167747	165305, 165395, 165425, 165394, 165272, 165166, 165164
167749	165807
169641	165398, 165274, 165168
170123	165308, 165429, 165400, 165276, 165963
170316	165306
170389	165197, 165236
170775	165839, 165933
170879	165205
171084	171611, 171631, 171652, 172093
171552	165427, 165170, 165203, 165201, 165749, 165240, 165746
171553	165242
173732	165750
173825	165423, 165271
173961	165199
174650	165268
176277	165811, 165936, 165842, 165310, 165810, 165278, 165966
183894	165302

Declaration of Originality

I, Darius Grüber, student registration number: 22532461, hereby confirm that I completed the submitted work independently and without the unauthorized assistance of third parties and without the use of undisclosed and, in particular, unauthorized aids. This work has not been previously submitted in its current form or in a similar form to any other examination authorities and has not been accepted as part of an examination by any other examination authority.

Where the wording has been taken from other people's work or ideas, this has been properly acknowledged and referenced. This also applies to drawings, sketches, diagrams and sources from the Internet.

In particular, I am aware that the use of artificial intelligence is forbidden unless its use an aid has been expressly permitted by the examiner. This applies in particular to chatbots (especially ChatGPT) and such programs in general that can complete the tasks of the examination or parts thereof on my behalf.

Any infringements of the above rules constitute fraud or attempted fraud and shall lead to the examination being graded "fail" ("nicht bestanden").

Erlangen, 24.02.2025
Place, Date

Grüber
Signature